Physics | Lancaster University

Arsenide Nanowire Based Quantum Materials for Advanced Photonics

by

ZhiMing Jin

Supervisor

Dr. QianDong Zhuang

Dissertation submitted in partial fulfilment for the degree of *Doctor of Philosophy*

May 2020

Abstract

This work concentrates on hybrid structures based on arsenic-containing nanowires, with a focus on material growth, structural regulation, performance characterization, and device construction, in order to obtain quantum heterostructures with excellent performance near the telecommunication characteristic wavelength. Specifically, it includes the following work:

We first study the growth of InAs NWs and GaAs NWs. Based on the full understanding of the selective area growth method, the importance of the appropriate oxide layer on the surface of the silicon wafer for nanowire growth is explained. The two-step growth method is demonstrated to realize the growth of GaAs NWs, and the droplet assisted growth method is also proposed to achieve the growth of InAs NWs.

For the InAs nanowires, after the successful growth of vertically InAs NWs standing on silicon substrate, the TEM results show a mixed phase of WZ and ZB, the PL results show emissions both from transition of BtB and type-II alignment. The built-in electric field formed in InAs NWs on p-type substrate leads to carrier assembling around the WZ-on-ZB interface, thus affected the emission feature.

By carefully tuning $FR_{\mathrm{V/III}}$ and F_{Sb}, InAsSb NWs with different Sb content have been obtained. The crystalline phases regulation and luminescence properties are clearly revealed as a function of Sb incorporation via detailed measurements and analysis (including TEM, temperature-sweeping PL, power-sweeping PL) on a series of InAsSb samples. InAsSb NWs with Sb incorporation of up to 19% have been obtained by suppressing the Sb surfactant effect, and the emission wavelength is successfully extended to 5.1 µm covering the entire MWIR band. This study opens the way to fabricate next-generation

devices using InAsSb NWs , such as highly sensitive silicon-based room-temperature infrared photodetectors operating in MWIR and LWIR, by combining the advantages of III-V semiconductors.

InAs/AlSb core–shell nanowire heterostructure is realized by molecular beam epitaxy and they also exhibit remarkable radiative emission efficiency, which is attributed to efficient surface passivation and quantum confinement induced by the shell. A high-performance core–shell nanowire phototransistor is also demonstrated with negative photoresponse. It has a dark current two orders of magnitude smaller and a sixfold improvement in photocurrent signal-to-noise ratio, in comparison with simple InAs nanowire phototransistor.

InAs/InGaAs core-shell NWs are also obtained by growing the shell layer after the InAs stem. Due to the introduction of Ga, nanowires exhibit a mixed growth path of core-shell and axial heterostructure. The EDS analysis implies that Ga exhibits stronger incorporation in the shell growth. The PL results show a bimodal emission with a main peak energy of approximately 0.425 eV, with a very stable temperature profile.

GaAs NWs were grown via VLS mode, and their optical properties were studied. The temperature and excitation scanning PL results show that the emission mainly comes from the transition of type-II alignment. The formation of the heterojunction after the introduction of Sb element was confirmed under the premise of maintaining the axial growth. The embedding of multiple GaAsSb nano disks is realized, with the emission wavelength increased to 1 µm, and the offset of conduction band of GaAs/GaAsSb is estimated to be about 53 meV. In addition, the embedding of ultra-thin GaAsSb nano disk is also successfully obtained associated with novel phenomenon of phase tuning.

Contents

List of Tables

List of Figures

Chapter 1

Introduction

1.1 Light and spectroscopy

"Nature and nature's laws lay hid in night; God said 'Let Newton be' and all was light." Light is the most widely used way of accepting information in human life. Research shows that more than 80% of the information that a person receives is through vision [1], and any vision is inextricably linked to light. In addition, modern society light has broad application in information acquisition (all kinds of detectors like cameras and face ID in mobile phones) [2, 3], transmission (including telephones, radio broadcasts, fiber-optic networks, bluetooth *et al.*) [4–7] and processing [8, 9], and even in energy harvest (such as photosynthesis and solar cells) [10] and illumination [11]. The vast majority of the process is inseparable from light, so that the importance of light is reflected in almost every corner of modern life.

Numerous applications use light of different wavelengths or energy. It is regarded as one kind of electromagnetic wave, whose wavelength λ is inversely proportional to its frequency ν. The product of the two is equal to the speed of light c, which satisfies:

$$c = \lambda\nu \tag{1.1}$$

It is also regarded as an energy quantum whose energy E is proportional to its frequency ν and satisfies the relationship:

$$E = h\nu = \hbar\omega \tag{1.2}$$

where h is the Planck constant, $\hbar = h/2\pi$ is the reduced Planck constant, and $\omega = 2\pi\nu$ is the angular frequency.

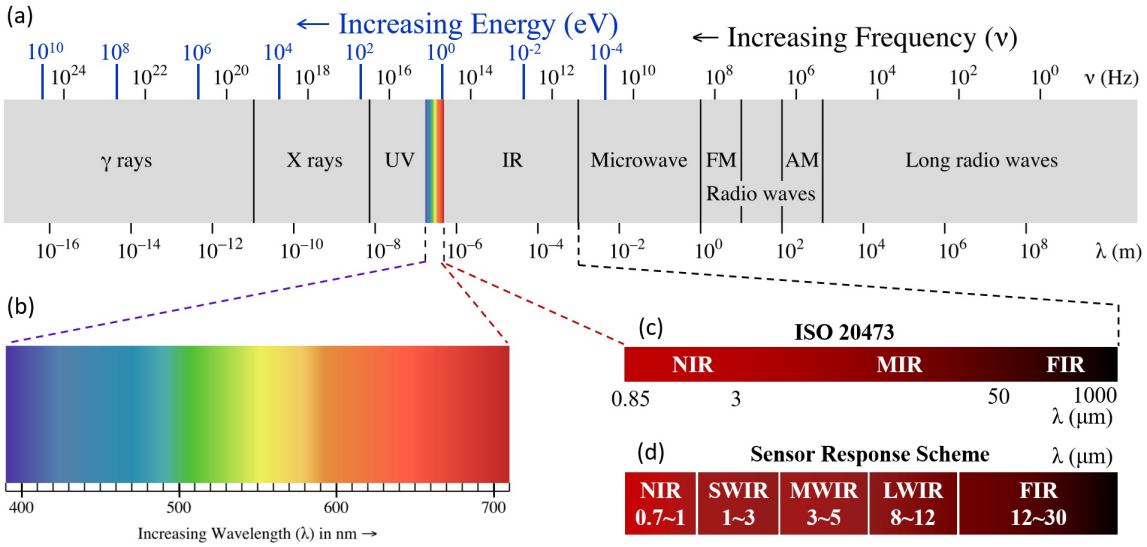

Figure 1.1: Spectrum of light. (a) Whole spectrum of light, including γ-rays, X-rays, Ultra-violet, Visable-light, Infrared (IR), Microwave, Radio waves, and Long radio waves; (b) sperctrum of visable light; (c) 3 regions of IR spectrum according ISO 20473; (d) 5 typical regions for sensor application.

The spectrum [12] shown in Fig. 1.1 (a) contains different frequency bands, which may have different names in different fields. The frequency range overrides $1\sim10^{24}$ Hz, corresponding to the energy range of $10^{-15}\sim10^{10}$ eV, wavelength range of $10^{-16}\sim10^{8}$ m. The band can be seen by the human is called visible light, which occupies the range of $400-700$ nm, as shown in Fig. 1.1 (b). Light with wavelength longer than that of visible light is called infrared light and occupies the range of $0.8-1000$ μm. They are classified into near-infrared (NIR), mid-infrared (MIR), and far-infrared according to ISO 20473 as shown in Fig. 1.1 (c). In different disciplines and/or application scenarios, their scope is slightly different. For example, in the field related to sensor, they are divided into 5

regions as Fig. 1.1 (d) shows:

♢ Near-infrared (NIR $0.7-1$ µm), from the range that the human eye cannot detect to the range in which silicon can respond.

♢ Short-wave infrared (SWIR $1-3$ µm), from the cutoff frequency of silicon to the cut-off frequency of the atmospheric infrared window, the InGaAs range can be up to 1.8 µm, and some less sensitive lead salts can also detect this range. Light of certain wavelengths in this range has a low attenuation rate in silica glass, and is usually used in fiber-optic communication, such as $1.53-1.56$ µm; and some wavelengths of light are very sensitive to image enhancement, usually can be used for night vision devices.

♢ Medium wave infrared (MWIR $3-8$ µm), defined by the atmospheric infrared window, is also the range covered by InSb and HgCdTe, and sometimes the range covered by PbSe. The passive infrared heat-seeking guided missile technology is designed to work with the atmospheric window of the $3-5$ µm band; the homing of the infrared sign of the aircraft is usually for the plume of the aircraft engine.

♢ Long-wave infrared (LWIR $8-12$ µm or $7-14$ µm) is determined by the range covered by HgCdTe and microbolometer. Among them, $8-15$ µm is the area of "thermal imaging", and the sensor working in this band can obtain a complete passive image of heat emission without the need of other light or external heat source.

♢ Far infrared (FIR $12-30$ µm) is the range covered by doped silicon.

The generation of light, the transmission of light, and the interaction of light and matter are generally all inseparable from atoms and molecules. Light with different wavelengths tend to have different generation mechanisms. From short wavelength range to long wavelength range, the mechanisms can be roughly divided into transition of intra-atomic electrons, transition of intramolecular electrons (for example, the case of semiconductor going to be discussed in Sec. 1.3), transition related to vibration, transition related to rotation, rotation of atomic nucleus, and rotation of free electrons. The rotation and/or

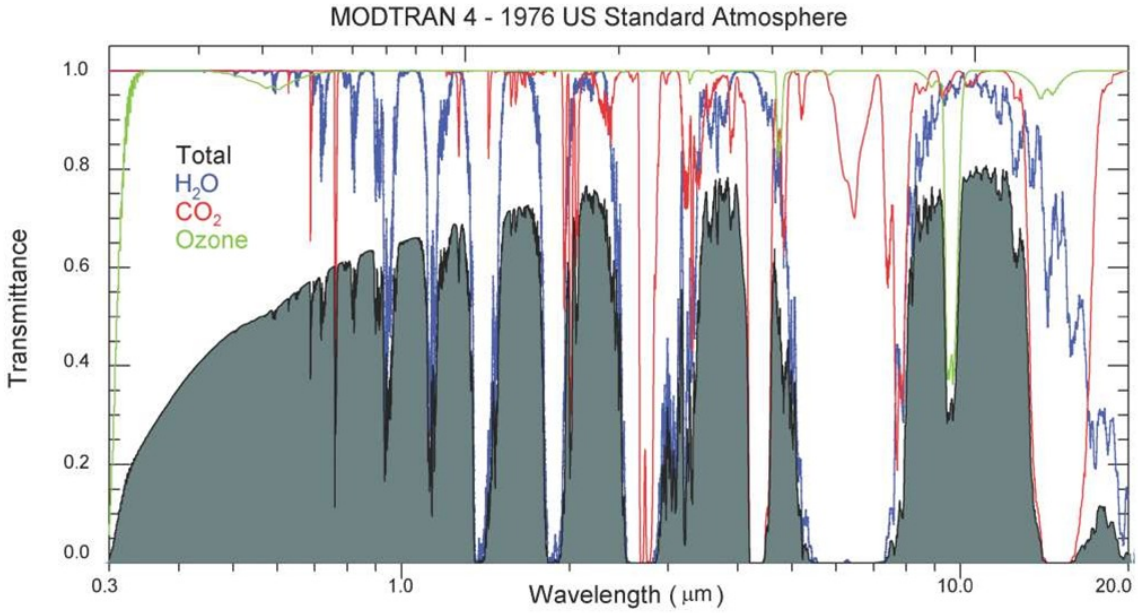

Figure 1.2: Atmospheric absorption and scattering.

vibration level of the molecule usually falls within the energy range of the infrared ray, so that a specific molecule or a functional group may result in a significant absorption effect on the infrared ray of a specific wavelength, and this characteristic can be used as a finger print for the molecules. Since the atmosphere also contains a lot of gas molecules, the infrared rays propagating in the air will also be attenuated by this absorption, so it is necessary to evade or correct when doing related tests. Fig. 1.2 shows the transmittance curve of the atmosphere in the range of $0.3 - 20$ μm. The transmission curves calculated using MODTRAN 4.0, version 2 [13]. The conditions are typical mid-latitudes, assuming a 1976 US standard atmosphere. The overall broad shape is caused by the scattering of molecular species and aerosols. It is worth noting that in the vicinity of 1.45 μm and 2.8 μm, the atmosphere has a strong absorption due to water vapor. In some region, the atmosphere is almost opaque. The absorption of light by ozone below 0.35 μm is very significant. Due to the ozone layer at the altitude of $20 - 40$ km, the atmosphere is opaque to sunlight below 0.3 μm. In general, the atmosphere is more transparent in the long-wave

infrared spectrum than in the visible spectrum.

Considering the wide application of infrared rays, this mainly discusses the preparation of materials and devices with infrared response characteristics, specifically III/V group semiconductors including Al/In/Ga & As/Sb. The fundamental of semiconductor materials will be introduced in the next section.

1.2 Structure of crystals

1.2.1 Formation of crystals

Solid materials can be classified into crystalline and amorphous materials according to the degree of order in which the atoms are arranged. The crystals of interest in this thesis are divided into monocrystals and polycrystals. The nature of the crystal is a reflection of the internal structure of the crystal. Inside the crystal, atoms or molecules are repeatedly arranged in a regular cycle in space, and the smallest repeating unit is called a unit cell as shown in Fig. 1.3. The open circles represent the atoms arranged in a spatial relationship in the crystal, and the bold black lines represent a unit cell. The actual crystal is the result of the unit cell being repeatedly arranged in three dimensions. In the crystal, since the distance and orientation between the particles arranged in various directions are different, the crystal has an important characteristic of anisotropy, that is, the properties of the same crystal in different directions are different. In contrast, amorphous is generally isotropic. The periodic arrangement of the particles inside the crystal and its ideal shape have specific symmetry. Such as: symmetry centre, symmetry plane, symmetry axis, *etc.*. Crystals are classified according to their symmetry.

Fig. 1.4 shows the schematic formation progress of hexagonal close packed lattice (HCP) and cubic close packed lattice (CCP). For the specificity of the content, we consider

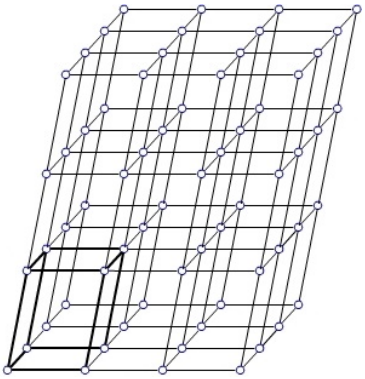

Figure 1.3: Schematic diagram of the structure inside crystal as an example.

a close packed lattice, and for simplicity, perfect spheres are used to represent the space that atoms occupied.

As shown in Fig. 1.4 (a), the blue atoms are taken as the first plane, which is called as "A-plane" for what we are going to built on it. Then the second layer will have the centre of the atoms right over the depressions of the A-plane, but it could be either the B- or C-configuration. For the sake of generality, B-configuration in Fig. 1.4 (a) is chosen as the second layer, thus the two layers have be determined as shown in Fig. 1.4 (b). The blue and pink spheres represent "A-plane" and "B-plane", respectively. Now the third layer has two choices: to site directly over the A-plane (called as A-configuration) or to site in the C-configuration, both of which are as the depressions of the "B-plane":

♢ If A-configuration is chosen for the third layer as the A-atom in Fig. 1.4 (c) shows, the HCP is obtained as the blue-pink-cyan stacking shown in the left part of Fig. 1.4 (d);

♢ If C-configuration is chosen for the third layer as the C-atom in Fig. 1.4 (c) shows, CCP is is obtained as the blue-pink-green stacking shown in the right part of Fig. 1.4 (d).

The above two ways couldn't be chosen at one time. If the third layer start chosing the A-configuration somewhere (the cyan atoms in the left part of Fig. 1.4 (d)) and the C-configuration somewhere else (the green atoms in the right part of Fig. 1.4 (d)), a problem will occur as soon as the two parts meet to form the entire third layer: fault occurs at the

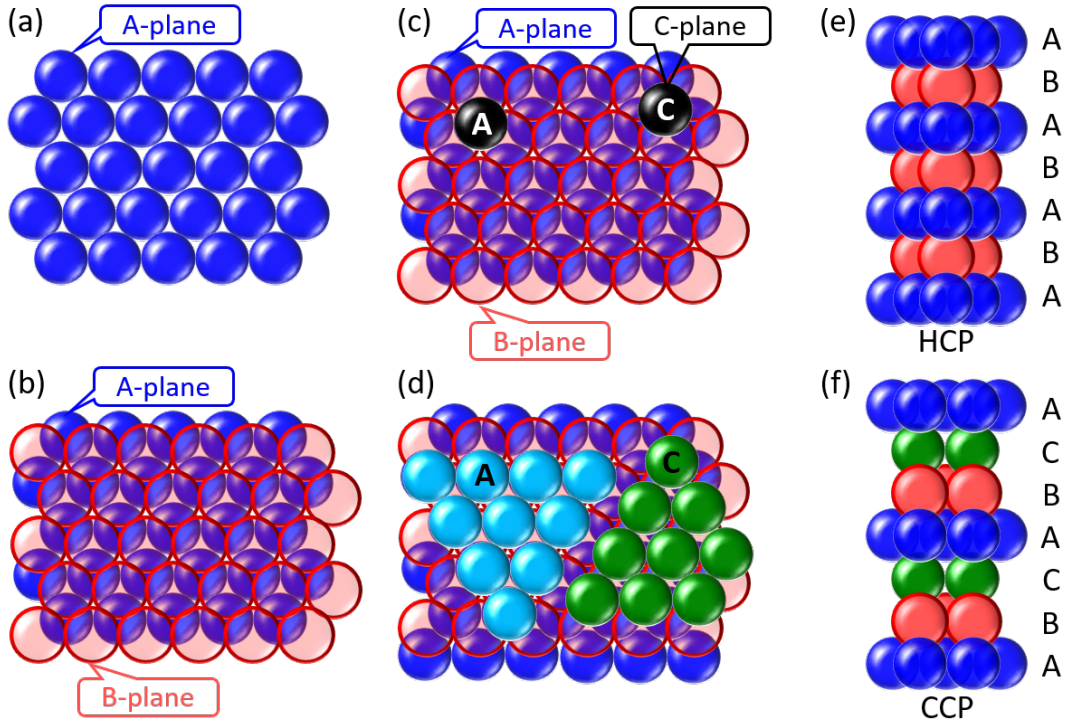

Figure 1.4: Schematic top-view diagram of the formation of HCP lattice and CCP lattice.

interface of the atoms stacking in different ways, which will be introduced soon below. For varieties sake and to distinguish the layers better, the bottom cyan "A-plane" is drawn in blue instead in Fig. 1.4 (d). In summary, the stacking sequences of the two close-packed lattices therefore are

CCP: ABCABCABCA $\cdots$

HCP: ABABABA $\cdots$

1.2.2 Wurtzite and Zinc-Blende phases in crystals

The cryatals discussed in this thesis would be binary semiconductors usually crystallizing in Wurtzite (WZ) or Zinc-Blende (ZB) phases, which could be classified into HCP and CCP, respectively. In order to illustrate the characteristics of WZ and ZB more graphically, the structure diagram of WZ and ZB is drawn in Fig. 1.5. Fig. 1.5 (a) & (b)

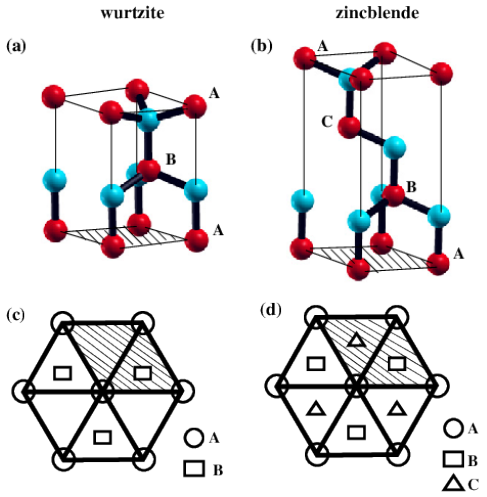

Figure 1.5: Schematic diagram of WZ and ZB phases.

show the crystal structures in WZ and ZB symmetries in cross-section [14], while cations and anions are denoted with two different colours. An ideal WZ structure consists of two interpenetrating HCP sublattices, one of atoms A, the other of atoms B, displaced from each other by $\frac{3}{16}c$ alongthe c-axis. On the other hand, the ZB structure consists of two interpenetrating face-centred-cubic (FCC) sublattices, one of atoms A, the other of atoms B, displaced from each other along the body diagonal by $\frac{1}{4}a$, where a is the lattice constant for the ZB structure. Thus the stacking sequences is ABAB$\cdots$ along the c-axis for WZ as Fig. 1.5 (c) shows and ABCABC$\cdots$ along the [111] direction for ZB as shown in Fig. 1.5 (d).

1.2.3 Defects in crystals

During the crystal formation process, due to various factors, the arrangement of atoms may break the standard repeating arrangement, which leads to various forms of defects. Common types of defects in crystals has been sketched in Fig. 1.6 [15], which covers types of defects from simple vacancies to phase boundaries, as well as more complicated defects such as point defects, dislocations, stacking faults, grain boundaries. Crystal lattice defects

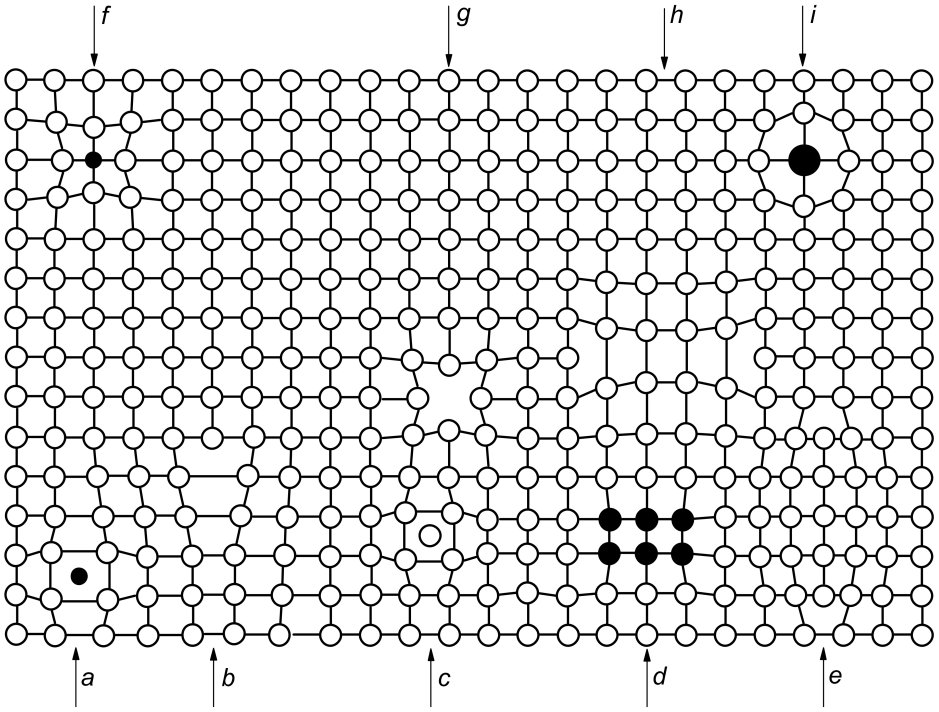

Figure 1.6: Fundamentals of Defects in Crystals. (a) impurity interstitial, (b) dislocation, (c) self-interstitial, (d) cluster of impurity atoms, (e) extrinsic dislocation loop, (f) small substitutional impurity, (g) vacancy, (h) intrinsic dislocation loop, (i) large substitutional impurity.

are usually classified according to their dimensions:

♢ Zero-dimensional (0-D) defects.

0-D defects are often called "point defects". Most prominent are vacancies and interstitials sketched as (a) & (c) & (f) & (g) & (i).

♢ One-dimensional (1-D) defects. 1-D defects include all kinds of dislocations; for example: rerfect dislocations, partial dislocations (always in connection with a stacking fault), dislocation loops, grain boundary and phase boundary dislocations, and even dislocations in quasi-crystals sketched as (b) & (e).

♢ Two-dimensional (2-D) defects. Here we have stacking faults(SF) and grain boundaries in crystals of one material or phase, and phase boundaries and a few special defects as *e.g.* boundaries between ordered domains.

♢ Three-dimensional (3-D) defects. 3-D defects include precipitates, usually involving impurity atoms. Voids(little holes, *i.e.* agglomerates of vacancies in 3-D form) which may or may not be filled with a gas, and Special defects, *e.g.* stacking fault tetrahedra and tight clusters of dislocations.

We simply classify the defects into three categories: stacking fault (SF), rotational twin-plane (TP), and polytype boundary (PB). The SFs are partial displacements affecting the regular sequence in the stacking of the lattice planes caused by either a vacant plane (intrinsic SF) or an insertion of extra plane (extrinsic SF). The TPs are planes where the crystal is rotated by 60° or 180°. The PBs are the planes between ZB and WZ phases whose density implies the size of segment of the phases.

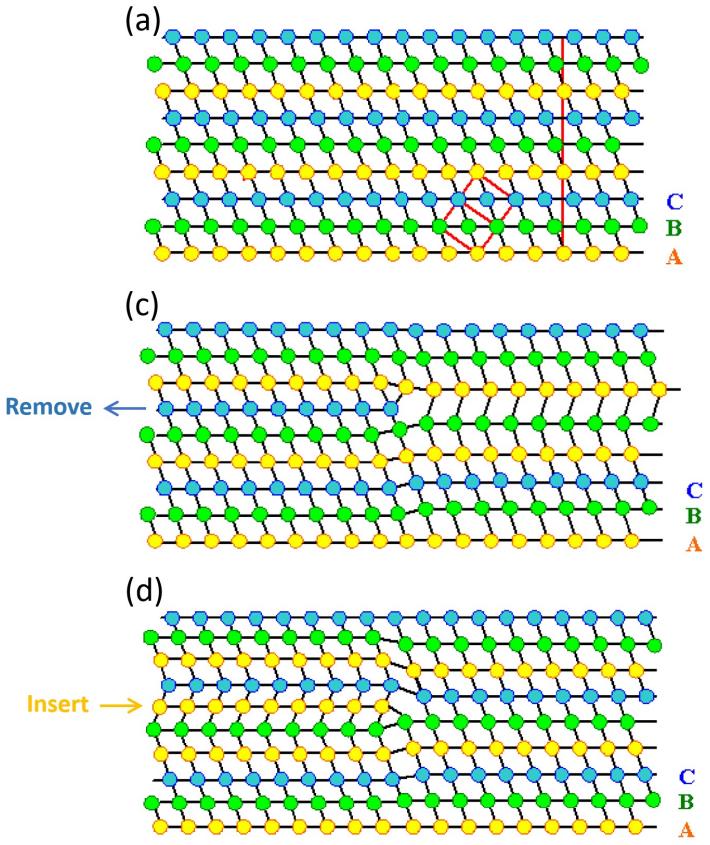

Figure 1.7: Schematic diagram of the formation of SFs.

As shown in Fig. 1.4 (d), when atoms stack in abnormal way, a mutation in the arrangement of atoms will occur at the interface where atoms arrange in different ways meet. Fig. 1.7 shows the specifics of SFs. Planes with the same letter are on lines perpendicular to the 111planes indicated by thin black lines, as shown in Fig. 1.7 (a). The projection of the elementary cell is shown with red lines. When parts of a horizontal 111 plane are removed—by agglomeration of vacancies on that plane—*e.g.* "C-plane" here as the blue arrow shows in Fig. 1.7 (b), A-plan and C-plane in the right part become neighbours. This produced a SF because the stacking sequence

ABCABC$\cdots$

has been changed to the faulty sequence

ABCAB$|$ABCA$\cdots$

The SF is at the line between the large letters. If a disk of agglomerated interstitials is inserted in the yellow position, insead of vacancies on a plane, the structure is sketched in Fig. 1.7 (c). the stacking sequence

ABCABC$\cdots$

is changed to the faulty sequence again:

ABCAB$|$A$|$CABCA$\cdots$

The SFs should also be at the lines between the large letters. This is a different kind of stacking fault than the one from Fig. 1.7 (b). For historical reasons, we call the stacking fault produced by vacancy agglomeration "intrinsic SF" and the stacking fault produced by interstitial agglomeration "extrinsic SF". Stacking faults by themselves are simple 2-D defects. They carry a certain stacking fault energy around a few 100 mJm^{-2} very roughly

.

TPs or called "twin boundaries" are the frequently encountered grain boundaries in many other CCP crystals. The formation process is easy to understand as sketched in Fig. 1.8. The up and down atoms on either side of the red line configurate mirror-

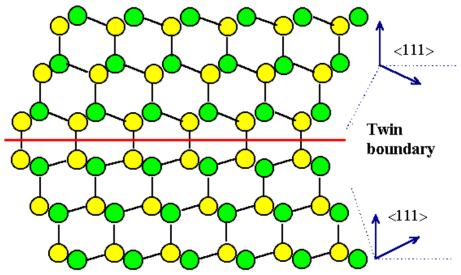

Figure 1.8: Schematic diagram of TPs.

symmetric layers without any bond lengths or bond angles being changed.

It is worthing note that in the real growth process of crystal, SFs and TPs may alternate or appear randomly in large numbers, resulting in uncontrollable mixed phases of WZ & ZB, which is called polytypism. Polytypism comes from the uncontrollable swtitch between WZ and ZB phases, and generally results in poor optical and optoelectronic performance for the device. Polytypism has density determining the size of segment of each phase. According to Caroff *et al.* [16], to form a segment of each phase, the minimum sequence should be at least (ABAB) for WZ and (ABC) for ZB. Considering the size of unit for kinds of materials is different, the minimam thickness for WZ and ZB differs. For example, the smallest WZ segment (ABAB) is 2.8 nm in length, while the smallest ZB segment (ABC) is 2.1 nm in length.

1.3 Traditional semiconductor materials

Semiconductor materials have been well studied in the past hundred years since Michael Faraday found the first semiconductor materials (AgS) in the the year of 1833 [17].

The first generation of semiconductor materials mainly refer to silicon (Si) and germanium (Ge) semiconductor materials. As the first generation of germanium and silicon semiconductor material and technology in the international information industry in all

kinds of discrete device is very popular and application of integrated circuit, electronic information network engineering, computer, mobile phone, TV, aerospace, military engineering and in the rapid development of new energy, silicon photovoltaic industry has been extremely widespread application. Due to the disadvantages such as high price, high noise and poor stability, Ge has almost withdrawn from the semiconductor market at present, and Si has become the representative and main force of the first generation of semiconductors. Silicon chips shine in every corner of human society, including personal computers and mobile phones.

Second generation semiconductor materials mainly refer to compound semiconductor materials, such as gallium arsenide (GaAs) and indium antimonide (InSb).Ternary compound semiconductors, such as GaAsAl, GaAsP; some solid solution semiconductors, such as Ge-Si, GaAs-GaP; glass semiconductors (also known as amorphous semiconductor), such as amorphous silicon, glass oxide semiconductor; Organic semiconductor, such as phthalocyanine, copper phthalocyanine, polyacrylonitrile, *etc.*. The second generation semiconductor materials are mainly used to make high speed, high frequency, high power and light-emitting electronic devices. Due to the rise of information superhighway and Internet, it is also widely used in satellite communication, mobile communication, optical communication, GPS navigation and other fields.

Si and compound semiconductor is two complementary material, compound of certain performance advantages make up for the shortcomings of Si crystal, and the production process of Si crystal clear has irreplaceable advantages, and both has certain limitation in application field, so on semiconductor applications often use compatible means will both compatible, take their own advantages, to produce products that meet the higher requirements, such as high reliability, high speed of the national defense military products.Therefore, the first and second generations are a long-term common state.

The third generation of semiconductor materials are wide bandgap ($E_g > 2.3$ eV)

semiconductor materials represented by silicon carbide, gallium nitride (GaN), zinc oxide (ZnO), diamond and aluminum nitride (AlN). In terms of application, according to the development of third-generation semiconductor, its main applications are semiconductor lighting, power electronic devices, lasers and detectors, and other four fields, each of which has different industrial maturity. In the frontier research field, wide bandgap semiconductor is still in the laboratory research and development stage. Compared with the first generation and second generation of semiconductor materials, the third generation of semiconductor materials with wide bangap width, high breakdown electric field, the high thermal conductivity, high electron saturation rate and higher ability to resist radiation, and thus more suitable for making high temperature, high frequency, resistance to radiation and high power devices, usually known as wide bandgap semiconductor materials (forbidden band width is greater than 2.2 eV), also known as the high temperature semiconductor materials.

It is worth mentioning that in addition to crystalline semiconductors, amorphous semiconductors have also been widely studied because they can be prepared by evaporating or sputtering, *etc.*, just like a film. And some materials can be even produced via solution process. In amorphous semiconductors, Bloch's theorem loses its meaning, and the electronic state can not be described by the exact k value. Thus the momentum selection rule for transitions is no longer strictly effective, so the light absorption edge will become blurred. Since the dependence between density of states and energy is still mainly determined by the bonding states of local electrons, the allowable band and the energy gap still exist in those materials. Their applications have also been extensive in recent years, such as solar cells, photodetectors, LEDs, lasers based on organic small molecule compounds or polymer materials, amorphous silicon hydride solar cell. However, these amorphous semiconductors are beyond the scope of this thesis. The semiconductors studied in this thesis, unless specified, are all single crystalline materials or polycrystalline

mixture of WZ & ZB.

1.4 Energy band theory of semiconductors

1.4.1 The foundation of energy band theory

Energy band theory is a theory that uses quantum mechanics and quantum statistics to study the electron motion inside a solid. It is an approximation theory developed in the early 20^{th} century after the establishment of quantum mechanics. It has qualitatively clarified the general characteristics of electron motion in crystals, and further illustrates the difference between conductors and insulators, semiconductors, and explains the mean free path of electrons in crystals. Since the 1960s, after the widespread use of electronic computers, it has become possible to use electronic computers to perform complex energy band structure calculations based on first principles. The band theory has evolved from qualitative to a quantitative precision science. The foundation of the semiconductor band theory is quantum mechanics, which is generally derived from the Schrödinger equation:

$$\left[-\frac{\hbar^2}{2m}\nabla^2 + V(\mathbf{r})\right]\psi(\mathbf{r}) = E\psi(\mathbf{r}) \tag{1.3}$$

where $\psi(\mathbf{r})$ is the wave function, m is quality, ∇ is differential operator, E is energy. For an ideal crystal, the atoms are arranged in lattice and have periodicity as shown in Sec. 1.2.1, so it can be considered that the potential field of the ions is a periodic equivalent potential field:

$$V(\mathbf{r}) = V(\mathbf{r} + \mathbf{R}_{\text{n}}) \tag{1.4}$$

Thus, the electrons in the crystal move in this periodic equivalent potential field.Bloch

proved that for the Schrödinger equation with the periodic potential field above, the solution must be in the form of a Bloch wave function:

$$\psi_{\mathbf{k}}(\mathbf{r}) = u_{\mathbf{k}}(\mathbf{r}) \exp(i\mathbf{k} \cdot \mathbf{r}) \tag{1.5}$$

which is called Bloch's theorem. This theorem shows that for the wave equation in the periodic potential field, its eigenfunction is in the form of a plane wave $\exp(i\mathbf{k} \cdot \mathbf{r})$ multiply by a periodic function $u_{\mathbf{k}}(\mathbf{r})$, in which $u_{\mathbf{k}}(\mathbf{r}) = u_{\mathbf{k}}(\mathbf{r} + \mathbf{T})$ has lattice periodicity, and $\mathbf{T}$ is the lattice translation vector. $\mathbf{k}$ is the wave vector and the electron energy E is a function of $\mathbf{k}$ written as

$$E = \frac{\hbar^2 \mathbf{k}^2}{2m^*} \tag{1.6}$$

where m^* is the effective mass.

From the perspective of energy band theory, for metals, the electron inside is not bound around a single atom, but moves inside the entire solid, only perturbed by the real field of the ion. The main part of the eigenwave function is the eigenstate of the momentum, and the scattering only gives the first order correction. This is named as nearly-free electron model. But for semiconductors and insulators, tight-binding approximation is required. The tight-binding approximation is to regard the electrons near one atom as being mainly affected by the potential field of the only atom. The action of other atomic potential fields is regarded as perturbation, so that the relationship between the atomic energy level of the electron and the energy band in the crystal can be obtained. In this approximation, the band's electronic wave function can be written in the form of the sum of the Bloch wave functions:

$$\psi_{\mathbf{k}}^{i} = \frac{1}{\sqrt{N}} \sum_{\mathrm{n}} e^{i\mathbf{k}\cdot\mathbf{R}_{\mathrm{n}}} \psi_i(\mathbf{r} - \mathbf{R}_{\mathrm{n}}) = \frac{1}{\sqrt{N}} \sum_{\mathrm{n}} e^{i\mathbf{k}\cdot\mathbf{R}_{\mathrm{n}}} \mathbf{W}_{\mathrm{n}}(\mathbf{r} - \mathbf{R}_{\mathrm{n}}) \tag{1.7}$$

where $\mathbf{W}_{\mathrm{n}}(\mathbf{r}-\mathbf{R}_{\mathrm{n}})$ is called Wannier function. Eq. 1.7 can be solved using the perturbation theory, and each solution corresponds to an atomic energy level. When N atoms are far apart, each atom has a different atomic energy level, and the single electronic state of the whole system is N-degenerate. When the atoms are put together to form the actual crystal, due to the overlap of the closest atomic wave function, N-degenerate is released. thus the energy level is broadened into energy bands. The tight-binding model is computationally intensive and the scope of application is much larger than the nearly-free electron model, thus it is suitable for calculating the energy bands for a considerable number of crystals.

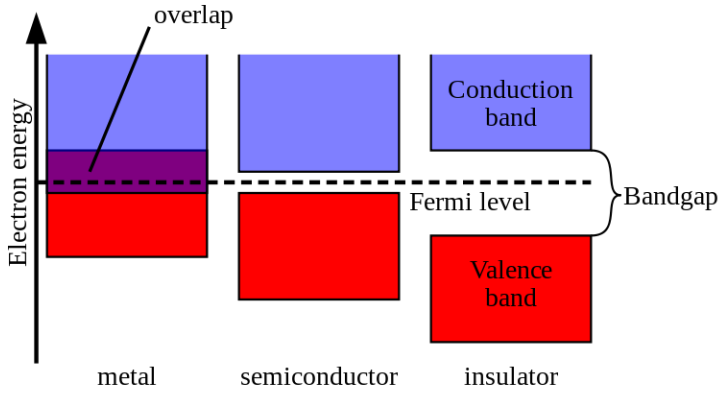

Figure 1.9: Schematic diagram of energy band structure for metal, semiconductor and insulator.

Fig. 1.9 shows a schematic diagram to qualitatively describe the relative position of the energy bands for metal, semiconductor, and insulator. The blue band is conduction band, the red band is valence band, and the middle dotted line is Fermi level. It can be seen that the metal has no energy gap, and the semiconductor and the insulator have energy gaps E_{g}, and the latter has a larger energy gap than the former. The atomic energy level can be occupied by electrons, and the conduction band and the valence band are both derived from the release of atomic energy levels, thus they could be occupied, whose implication is that the bangap between the energy bands is forbidden for electrons, as a results the bangap is also forbidden band.

The bottom of real conduction band and the top of real valence band are not flat. It is easy to know from Eq. 1.6 that:

$$E_{\mathrm{C}} = \frac{\hbar^2 k^2}{2{m_{\mathrm{C}}}^*} \tag{1.8}$$

and

$$E_{\mathrm{V}} = \frac{\hbar^2 k^2}{2{m_{\mathrm{V}}}^*} \tag{1.9}$$

where ${m_{\mathrm{C}}}^* = \hbar^2/(\mathrm{d}^2 E_{\mathrm{C}}/\mathrm{dk}^2)_{\mathrm{k}=0}$ and ${m_{\mathrm{V}}}^* = \hbar^2/(\mathrm{d}^2 E_{\mathrm{V}}/\mathrm{dk}^2)_{\mathrm{k}=0}$ are the effective mass of electrons at the bottom of the conduction band and at the top of the valance band, respectively. The E verses k relations for conduction band and valence band are illustrated in Fig. 1.10 [18], where E_{g} equals the energy difference between the bottom of the conduction band and the top of the valence band.

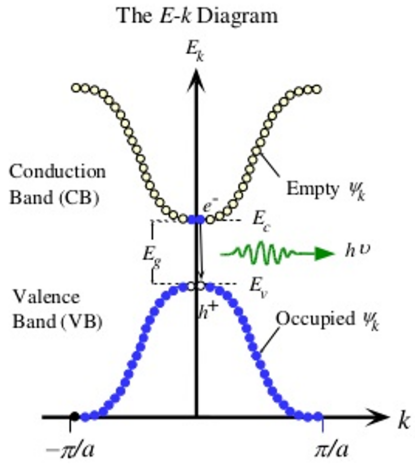

Figure 1.10: Energy verses k relation for a bulk semiconductor.

1.4.2 Density of states

As described above, each energy E in conduction band and valance band is available for electrons to occupy, but the number of energy states can be occupied is different for

each available energy value, *i.e.*, the number of energy states that can be occupied has a functional relationship to energy E. The number of energy states $p(\mathbf{k})$ can be derived by dividing the volume of the sphere $4k^3/3$ with the volume of the unit cell V and multiplying by a factor of two for the two electron spin states:

$$p(k) = \frac{k^3 V}{3\pi^2} \tag{1.10}$$

Thus the density of states (DoS), *i.e.*, the number of states per unit volume (in $\mathbf{k}$ space), can be written as:

$$D_{\mathrm{C,V}}(k) = \frac{\mathrm{d}p}{\mathrm{d}k}\frac{1}{V} \tag{1.11}$$

which is valid for both conduction band and valence band. The DoS plays an important role in the kinetic theory of solids. Considering the relationship between E and k shown in Eq. 1.11 & 1.9, the DoS in terms of electron/hole energy can also be calculated as:

$$D_{\mathrm{C}}(E_{\mathrm{C}}) = \frac{1}{2\pi^2}\left(\frac{2{m_{\mathrm{C}}}^*}{\hbar^2}\right)^{3/2} {E_{\mathrm{C}}}^{1/2} \tag{1.12}$$

and

$$D_{\mathrm{V}}(E_{\mathrm{V}}) = \frac{1}{2\pi^2}\left(\frac{2{m_{\mathrm{V}}}^*}{\hbar^2}\right)^{3/2} {E_{\mathrm{V}}}^{1/2} \tag{1.13}$$

The dependence of DoS against energy in free electron mode (green lines) and nearly-free electron mode (blue lines) is plotted in Fig. 1.11 (a) for the case where the band has no overlap ($E_{\mathrm{C}} < E_{\mathrm{V}}$), and in Fig. 1.11 (b) for band has overlap ($E_{\mathrm{C}} > E_{\mathrm{V}}$), respectively. The shape of energy band dirived from nearly-free electron mode is clearly shown in Fig. 1.11 (a) and could be understood as: 1) When $E < E_{\mathrm{A}}$, DoS in nearly-free electron mode (blue lines) is similar to the DoS in free electron mode (green lines); (2) When $E \simeq E_{\mathrm{A}}$, the volume increases due to the fact that the constant energy surface can be convex, so that DoS in nearly-free electron mode (blue lines) is large than the DoS in free

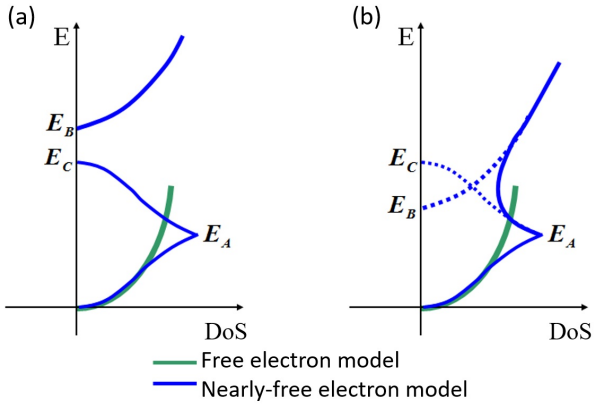

Figure 1.11: Schematic diagram of DoS in free electron mode and nearly-free electron mode.

electron mode (green lines); (3) When $E > E_{\mathrm{A}}$, the area reduced due to the breakage of the constant energy surface, especially when the E_{C} reaches the energy surface reduces to several apex angles, so the DoS will continuously drop to zero from E_{A} to E_{C} process. (4) When E reaches and exceeds the lowest energy E_{B} of the second Brillouin zone, the DoS will start increaseing rapidly from zero at E_{B}.

1.4.3 Level occupation

Under equilibrium conditions, the probability of an electron occupying a given energy state E can be described by Fermi-Dirac equation:

$$f(E) = \frac{1}{1 + \exp[(E - E_{\mathrm{F}})/k_{\mathrm{B}}T]} \tag{1.14}$$

where E_{F} is the energy of the Fermi level, k_{B} is the Boltzmann constant and T is the absolute temperature in degree Kelvin.

The conduction band and valance band are shown in Fig. 1.12 (a), the corresponding DoS and Femi-Dirac function are shown in Fig. 1.12 (b). The density of states that electrons or holes occupy can be written as:

$$n(E) = D_{\mathrm{C}} f(E_{\mathrm{C}}) \tag{1.15}$$

and

$$p(E) = D_{\mathrm{V}}[1 - f(E_{\mathrm{C}})] \tag{1.16}$$

where $n(E)$ and $p(E)$ are the density of states for electrons in CB and the density of empty states for holes in VB.

The density of states plays an important role in the kinetic theory of solids. The product of the density of states and the probability distribution function is the number of occupied states per unit volume at a given energy for a system in thermal equilibrium. This value is widely used to investigate various physical properties of materials.

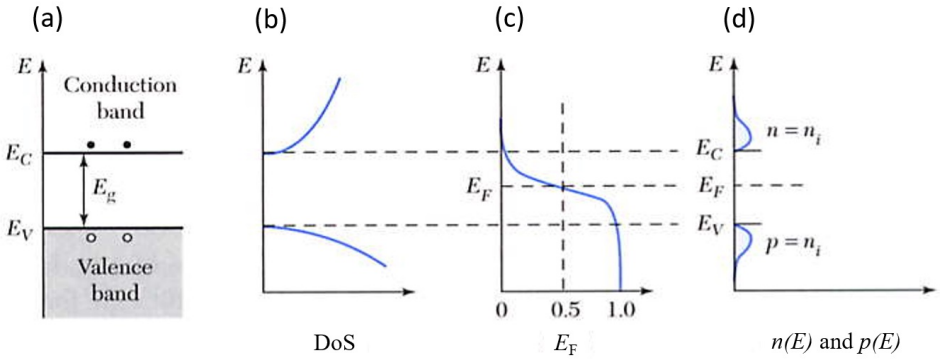

Figure 1.12: Schematic band diagram, DoS, Femi-Dirac distribution, and carrier concentrations for intrinsic semiconductor.

For intrinsic semiconductors E_{F} locates approximately in the middle of the energy gap as Fig. 1.12 (c) shows. As a result, the density of states that electrons and holes can occupy are symmetrically distributed for E_{F} as shown in Fig. 1.12 (d). Thus for $T > 0$, only a small fraction of electrons occupy the states in the conduction band of intrinsic semicondutors.

Doped semiconductors have different situation. For n-doped materials, large number of the ionized electrons exist at the bottom of the CB, which pull up the Fermi level E_{F}

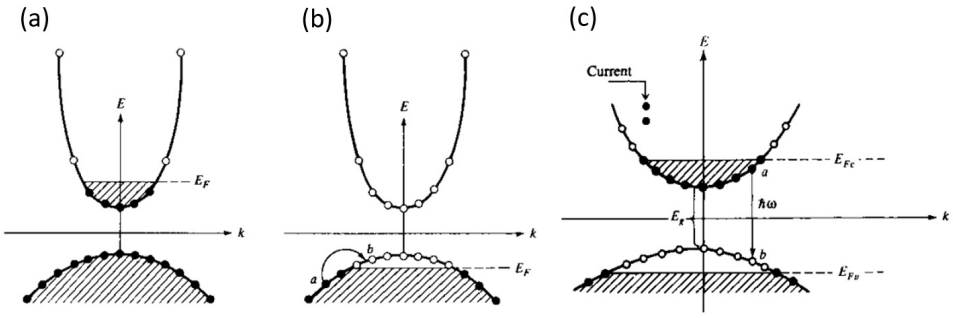

Figure 1.13: Energy bands and quasi Fermi levels in (a) *n*-doped semiconductors, (b) *p*-doped semiconductors and (c) in a *p*-*i*-*n* diode with external current injection.

(close to CB or into CB), causing the position of the Fermi-Dirac function increase as a whole. As a result of the product of DoS and its product, the $n(E)$ in CB increases sharply, and the $p(E)$ in VB slightly decreases. Falling, $n(E)$ and $p(E)$ are no longer symmetrically distributed as shown in Fig. 1.13 (a) [19]. For the case of *p*-type semiconductors, the absence of electrons on top of the VB results in the Fermi level E_{F} moving down (close to CB or into VB), leaving large number of holes in the bottom of the VB as shown in Fig. 1.13 (b). When both electrons and holes are externally injected into the material (*e.g.* in the middle of a *p*-*i*-*n* diode), electrons and holes can occupy the bottom of the VB and the top of the VB respectively at the same time, resulting in a large separation of quasi Fermi levels of electrons E_{FC} and of holes E_{FV} as shown in Fig. 1.13 (c).

1.4.4 Band alignment

Electronic devices typically require a combination of at least two semiconductors or two different doping types. When two different semiconductors are in contact, a sandwich structure is formed at the interface, thus different types of band alignments occur, whose shape depends on the difference in electron affinity and bangap of the two semiconductors.

In the type-I alignment, the CB of material-2 is lower than the CB of material-1 and its

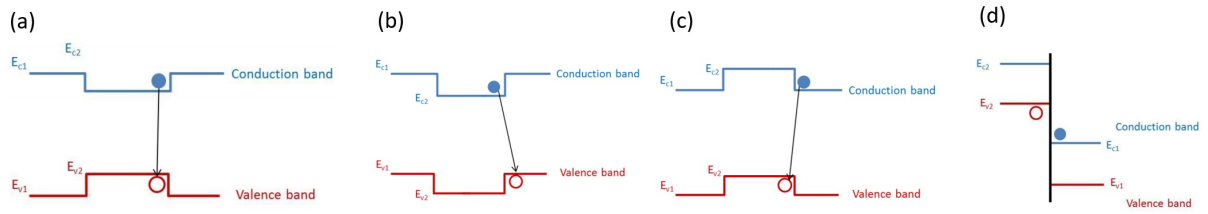

Figure 1.14: Schematic of band alignment for (a) type-I, (b)-(c) type-II, and (d) type-III.

VB is higher than the that of material 1 as shown in Fig. 1.14 (a). In this band alignment, the excited electrons in the VB and the excited holes in the VB tend to concentrate in material-2, as a result, most of the two types of carriers will recombine in material-2.

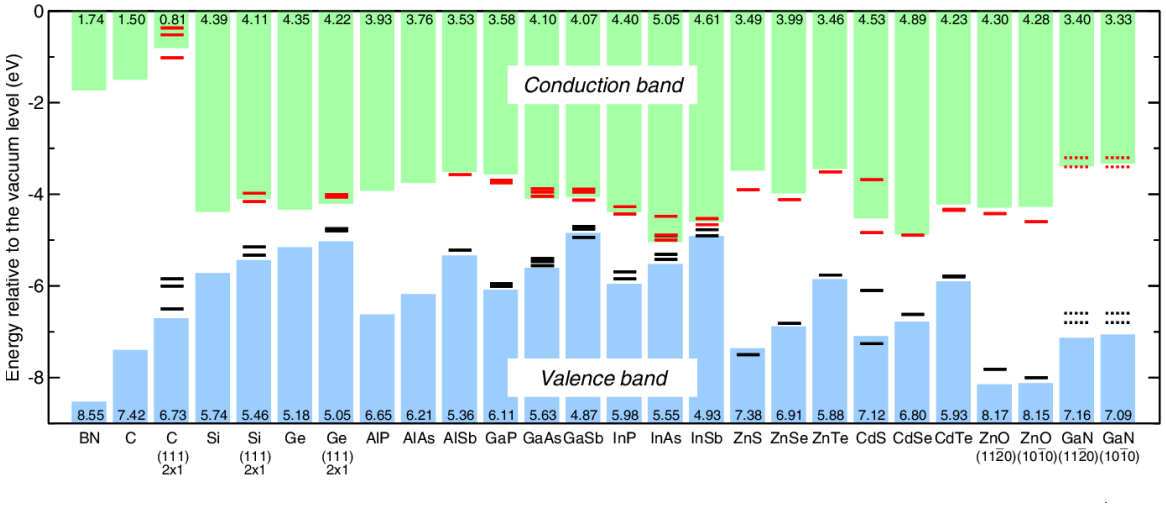

Figure 1.15: Schematic of band alignment for selected materials.

In the type-II alignment, the CB and the VB of the material-2 are lower (Fig. 1.14 (b)) than the CB or higher (Fig. 1.14 (c)) than the VB of material-1. In either case, the excited electrons and holes tend to separate and each of them concentrate in material-1 and material-2. Only one type of carrier tends to rise in the middle and recombination occurs between electrons and holes at the separation position, thus the recombination of electrons and holes happens at the interface of material-1 and material-2. In some material combinations, it is also possible that the CB of material-2 is lower than the CB

of the material-2 (*e.g.* InSb/InAs), creating a broken type-III band alignment, shown in Fig. 1.14 (d).

Fig. 1.15 shows the band alignments of selected materials based on the ionization potential (IP) and electron affinity (EA) obtained using GW 1@HSE [20]. The surface orientation is (110) unless otherwise noted. Experimental values reported for the corresponding surfaces are indicated by solid horizontal bars except for GaN, for which values for polar [0001] surfaces are shown with broken bars. The theoretical IP and EA values are shown as numbers at the bottom and top of the figure, respectively. The IP and EA correspond to the negatives of the top of VB and bottom of CB with respect to the vacuum level, respectively.

1.5 Common III-V group semiconductors and alloys

Semiconductors can be classified in a number of ways. According to the contained elements, semiconductors usually can be divided into element semiconductors and compound semiconductors. Compound semiconductors can be roughly divided into oxide semiconductor, III-V group semiconductor, II-VI group semiconductor, *etc.*.

Currently, III-V group compound semiconductors provide material basis for many mature commercial technologies as well as new electronic and photonic devices, including diode lasers, LEDs, photodetectors, opto-electric modulators, and frequency mixing components [21, 22]. The operational characteristics of these devices primarily depend on the physical properties of the materials. Because ternary and quaternary alloys can be included in addition to binary compounds, virtually unlimited flexibility can be achieved in design of heterostructure devices.

1.5.1 Bandgap and lattice constant

The ZB crystal consists of two interpenetrating FCC lattices, one having a group-III element atom (*e.g.*, B/Al/Ga/In) and the other a group-V element atom (*e.g.*, N/P/As/Sb). A ZB crystal is characterized by a single lattice constant a. Most of the III-V semiconductors have ZB phase, except for some of the III-nitride materials.

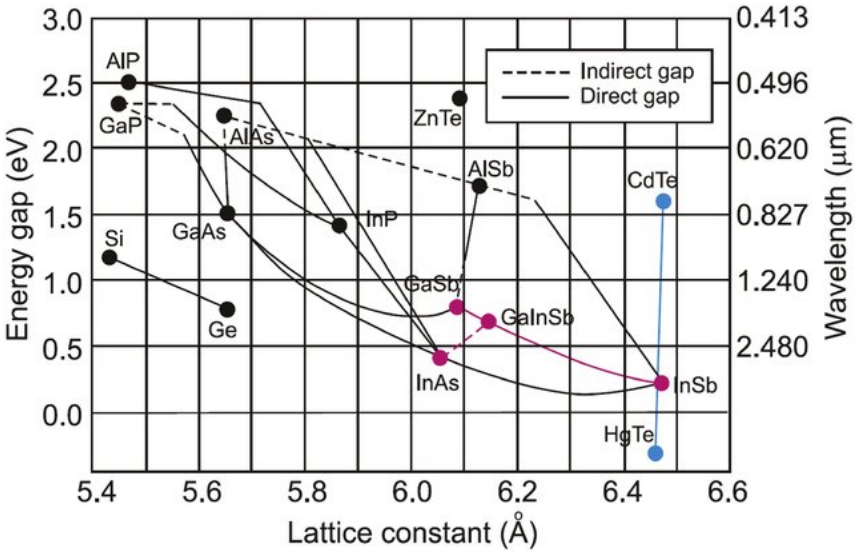

Figure 1.16: Bandgaps at 0 K and lattice constants for typical semiconductors and their alloys.

Fig. 1.16 shows bandgaps against their lattice constant for typical semiconductors and their alloys [23], including IV, III-V, II-VI, and IV-VI group semiconductors. The filled and unfilled circles indicate, respectively, direct and indirect bandgap materials. The five black dashed vertical lines indicate commonly used substrates for the epitaxial growth of materials: Si, GaAs, InP, InAs and GaSb. The ranges of available lattice constants and corresponding bandgaps for a 1% and 3% lattice mismatch with GaAs are indicated by the red and green shaded areas, respectively. High-quality materials with a few percent of mismatch can be readily grown at the nanoscale, leading to a large range of bandgaps in nanomaterials. Among all the binary III-V semiconductors, only InAs, GaSb and InSb

have the bangaps lower than 1 eV, corresponding to the wavelength for telecommunication range $\sim$ 1.3 µm. InSb has the narrowest bangap of 0.24 eV, corresponding to a wavelength of 5.17 µm. The lattice constant of InSb is 6.479 Å , the largest of the binary materials shown on the graph. InAs has the second narrowest bangap (0.415 eV) among these materials.

1.5.2 Direct and indirect bandgap semiconductor

If a transition between CB and VB happens without the change of momentum, this transition is called the direct transition and the semiconductors are called direct bandgap semiconductors as shown in Fig. 1.17 (a) for few examples of these semiconductors such as GaAs, InAs, GaSb, and InSb. In direct bandgap semiconductors, the transition of electrons from the CB to the VB can result in an emission of photons with energy equal to the energy bangap E_g. Unlike the direct bandgap semiconductors, indirect bandgap semiconductors have the CB minima and VB maxima at different locations (different momenta) as shown in Fig. 1.17 (b). For these semiconductors, electron transitions from

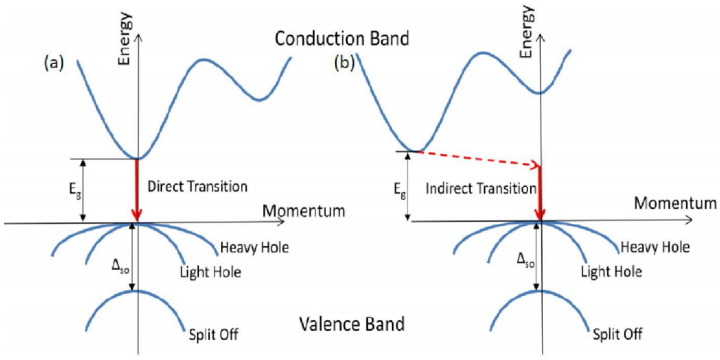

Figure 1.17: Schematic diagram of the electron energy at the bottom of CB and the top of VB against momentum for (a) direct bandgap semiconductors and (b) indirect bandgap semiconductors.

the CB to the VB at the bandgap energy must be accompanied by emission or absorption of phonons in order to account for the change in momentum, thus light emission and

absorption is usually difficult in indirect bandgap semiconductors.

1.5.3 Bandgap engineering

The energy of the emitted radiation from semiconductors can be tailored by altering the bandgap of a material. In nano-scale crystals, many parameters can be tuned so it is able to modulate their electronic bandgap, including size, shape, and composition. The bandgaps of ternary alloys (such as $AB_{1-x}C_x$) can be estimated by interpolating the binary semiconductors like:

$$E_g{}^{AB_{1-x}C_x} = (1-x)E_g{}^{AB} + xE_g{}^{AC} + x(1-x)\gamma \tag{1.17}$$

where $E_g{}^{AB_{1-x}C_x}$, $E_g{}^{AB}$, and $E_g{}^{AC}$ are the bandgaps for $AB_{1-x}C_x$, AB, and AC, respectively, and γ is the bowing parameter.

1.5.4 Temperaturedependence of bandgap

The bandgap decreases as temperature increases for semiconductors, which dependence follows the Varshni's Equation:

$$E_g(T) = E_g(0) - \frac{a\times 10^{-4}T^2}{T+b} \tag{1.18}$$

where $E_g(0)$ is the bandgap energy at 0 K, a and b are empirical parameters with different values for different semiconductors.

1.6 Recombination and generation

Under non-equilibrium conditions, excess carriers exist in the semiconductors. To restore the equilibrium condition, excessive electrons in the conduction band will recombine with holes in the valence band, either radiatively or non-radiatively.

During the radiative recombination process, the energy of the recombined electron-hole pairs is used to generate photons. In order to generate photons, the creation of excess electrons and holes can be achieved by various methods, *i.e.* bombardment with energetic electrons, ions or other particles. In experiments, the most common methods are: photo-luminescence — the radiative recombination of excess carriers which are generated by the absorption of light, and electro-luminescence — the radiative recombination of excess carriers which are generated by electrical injection. Different radiative recombination mechanisms are illustrated in Fig. 1.18 below:

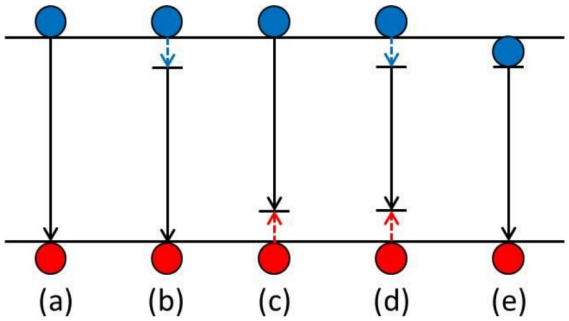

Figure 1.18: Schematic diagram of radiative recombination mechanisms in semiconductors. (a) band-to-band recombination, (b) donor-to-valence band recombination, (c) conduction band-to-acceptor recombination, (d) donor-to-acceptor recombination and (e) exciton recombination. The blue and red circles represent electrons and holes respectively. Straight line arrows and dotted vertical lines represent photon and phone emissions respectively.

1.6.1 Band-to-Band recombination

Band to band (BtB) recombination is the process in which an electron on the CB recombines with a hole on the VB as shown in Fig. 1.18 (a) and emits a photon whose energy equals to:

$$h\nu = E_{\mathrm{g}}(T) - \frac{1}{2}k_{\mathrm{B}}T \tag{1.19}$$

where $\frac{1}{2}k_{\mathrm{B}}$ accounts for the thermal effects. The rate of the band to band recombination can be written as:

$$R = -\frac{\mathrm{d}n}{\mathrm{d}t} = -\frac{\mathrm{d}p}{\mathrm{d}t} = Bnp \tag{1.20}$$

where n and p are the densities of free electrons and holes in the semiconductor, respectively, and the constant B is the bimolecular recombination coefficient. The typical value of B for direct bandgap III-V semiconductors is in the range of $10^{-11} - 10^{-9}$ $\mathrm{cm^3 s^{-1}}$. For indirect semiconductors, radiative BtB transition requires the participation of phonons as mentioned in Sec. 1.5.2, which is much less likely to happen because the value of B is smaller of three orders of magnitude as $10^{-15} - 10^{-14}$ $\mathrm{cm^3 s^{-1}}$.

1.6.2 Free to bound recombination

Donors and acceptors in the semiconductors can introduce energy states within the band gap, either close to the conduction band for donors or close to the valence band for acceptors. Other than the band-to-band recombination, radiative processes can also happen between electrons on the donors' state and holes on the valence band Fig. 1.18 (b), or between electrons on the conduction band and holes on the acceptor' state Fig. 1.18 (c). The energy of the emitted photons is:

$$h\nu = E_{\mathrm{g}}(T) - E_{\mathrm{i}} \tag{1.21}$$

Compared with Eq. 1.19, the additional term E_{i} represents the ionization energy of the donors or acceptors. For most direct band gap semiconductors, the donor / acceptor related recombination can be more clearly observed at low temperatures. With increasing temperature, donor-to-band (DtB) and band-to-acceptor (BtA) recombination shows a quicker decay compared with BtB transition, due to the thermal excitation of carriers out of the donor / acceptor states.

1.6.3 Donor to acceptor pair recombination

Radiative recombination can also happen if the density of both donors and acceptors are substantial $\sim 10^{16}\mathrm{cm}^{-3}$. The electrons in the donors can recombine with holes in the accpectors, both within the energy gap, as illustrated in Fig. 2.11d. The emitted photon energy equals to:

$$h\nu = E_{\mathrm{g}} - (E_{\mathrm{D}} + E_{\mathrm{A}}) + \frac{e^2}{\epsilon r} \tag{1.22}$$

where E_{D} and E_{A} are the ionization energy of donors and acceptors, respectively. The last term in this equation represents the Coulomb force between carriers on the donor and acceptor states, in which ϵ is the static dielectric constant and r is the donor-acceptor separation. Similar to DtB and BtA recombination, the donor-acceptor recombination can only be clearly seen at low temperatures.

1.6.4 Exciton recombination

Excitons are electron-hole pairs held together through Coulomb interactions. For free excitons, the energy of the emitted photon from an exciton recombination is:

$$h\nu = E_{\mathrm{g}} - E_{\mathrm{exc}} \pm KE_{\mathrm{p}} \tag{1.23}$$

where $K \cdot E_{\mathrm{p}}$ denotes the emission or absorption of K lattice phonons with the energy E_{p}. The value of E_{exc} is usually in the range of a few milli-electronvolts (meV). If the exciton is bounded next to a donor, acceptor or neutral atom (bound exciton), the energy of the emitted photon becomes smaller than the free exciton due to the lack of kinetic energy. The value becomes:

$$h\nu = E_{\mathrm{g}} - E_{\mathrm{bx}} - E_{\mathrm{exc}} \tag{1.24}$$

where E_{bx} is the binding energy of the exciton to the impurity. E_{bx} is also in the range of a few meV. The spectrum of bound exciton emission is usually narrower than free exciton and BtB emission spectra. Both free and bound exciton emissions can only be significant at low temperatures, since at high temperature the thermal energy can far exceed the exciton binding energy.

Besides the emission of photons, the energy released from the recombination of electrons and holes can also be transferred in non-radiative forms. The most common non-radiative recombination mechanisms will be discussed in this section.

1.6.5 Surface recombination

Surface states can be defined as a number of localized energy states or generation-recombination centres that may be introduced at the surface region. Surface states are related to the dangling bonds that are formed in semiconductors due to the lack of neighboring atoms. The danglingbonds trap impurities causing non-radiative emission. Surface state is common problem in nanowires due to the large area-to-volume ratio. However, it can be suppressed by surface passivation.

1.6.6 Auger recombination

During the Auger recombination, the released energy from an electron-hole pair recombination is used to excite another free electron to higher into the conduction band, or excite another hole deeper into the valence band. The excited electron or hole will quickly relax to the low energy end of their respective energy band through multiple phonon emissions. In this process, no photons are emitted. The three most common Auger recombination processes (CHCC, CHSH and CHLH) are schematically shown in the Fig. 1.19. As the mechanism of droop in LEDs is discovered, future research directions will focus on removing or reducing the losses caused by Auger recombination.

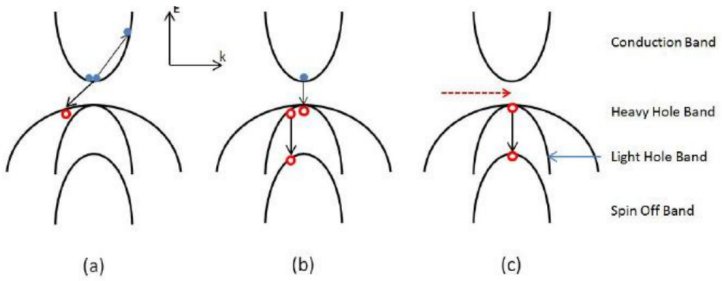

Figure 1.19: Schematic diagram of Auger recombination with different machanisms: (a) CHCC, (b) CHSH, and (c) CHLH.

1.6.7 Shockley-Read-Hall Recombination

In Shockley-Read-Hall (SRH) recombination, electrons and holes recombine via energy levels induced by impurities or lattice defects within the energy gap. As recombination centres, they trap electrons or holes; as generation centres, they emit carriers [24].

1.6.7.1 Inter-valence band absorption

The inter-valence band absorption (IVBA) process happens when the photon generated from electron-hole recombination is re-absorbed by lifting an electron in the spin split-off band to an injected hole state in the heavy hole band. The IVBA can be significant in materials where the energy gap between spin split-off band and heavy hole band is close to the bandgap E_g. The re-absorption needs to happen at larger wavevector k, making the process less likely [25].

1.6.7.2 Free carrier absorption

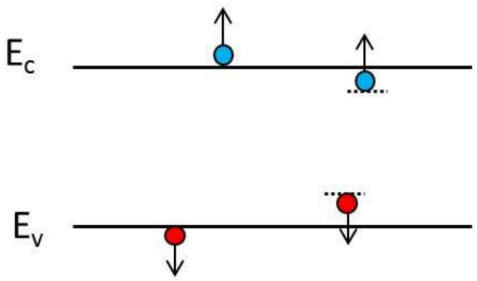

Figure 1.20: Schematic diagram of carrier transitions during free carrier absorption. Red dots: electrons, blue dots: holes, arrows: direction of carrier movement, short dotted lines: donor/acceptor states.

Free carrier absorption (or intra-band absorption) happens when a photon gives up its energy to an electron already in the conduction band or a hole in the valence band, thus raising it to a higher energy as illustrated in Fig. 1.20). Usually free carrier absorption also includes the absorption in which electrons/holes are excited from the shallow donor/acceptor states near the band edges into the conduction/valence band. For energies sufficiently lower than the band gap energy, free carrier absorption can become the dominant recombination mechanism. The rate of free carrier absorption is proportional to the carrier concentration, since one free carrier is required for an absorption event.

According to Drude free electron model, free carrier absorption increases as the square of the wavelength:

$$\alpha_{fc} = N\lambda^2 \tag{1.25}$$

where N is the concentration of electrons or holes and λ is the wavelength. From this quadratic relation, it is obvious that the free carrier absorption is stronger at longer wavelength range. So in mid-infrared devices, the effect of free carrier absorption can possibly be more significant than in near-infrared and visible devices.

1.6.7.3 Free carrier absorption

The mechanisms of the major non-radiative processes have been discussed, including Auger recombination, SRH recombination and surface recombination. Even though these nonradiative recombination rates can be reduced, they can never be totally eliminated. Besides, any semiconductor material contains some native defects which can induce non-radiative recombination. It is difficult to fabricate materials with impurity levels lower than parts per billion. Thus even the purest material contains impurity in the level of 10^{12} cm^{-3}. If the total radiative recombination lifetime is denoted as τ_{r} and the total non-radiative recombination lifetime is denoted as τ_{nr}, the overall recombination rate can be given by:

$$\tau^{-1} = {\tau_{\mathrm{r}}}^{-1} + {\tau_{\mathrm{nr}}}^{-1} \tag{1.26}$$

The probability of radiative recombination or internal quantum efficiency is:

$$\eta_{\mathrm{int}} = \frac{{\tau_{\mathrm{r}}}^{-1}}{{\tau_{\mathrm{r}}}^{-1} + {\tau_{\mathrm{nr}}}^{-1}} \tag{1.27}$$

It is worth to note that not all photons emitted internally can escape from the semi-

conductor due to the light-escape problem and re-absorptions.

1.6.8 Generation due to light

Carriers can be generated in semiconductors by illuminating the semiconductor with light. The energy of the incoming photons is used to bring an electron from a lower energy level to a higher energy level. In the case where an electron is removed from the valence band and added to the conduction band, an electron-hole pair is generated. A necessary condition is that the energy of the photon, E_{ph}, is larger than the bandgap energy, E_{g}. As the energy of the photon is given off to the electron, the photon no longer exists. If each absorbed photon creates one electron-hole pair, the electron and hole generation rates are given by:

$$G_{\mathrm{p,lignt}} = G_{\mathrm{p,lignt}} = \alpha \frac{P_{\mathrm{opt(x)}}}{E_{\mathrm{phA}}} \tag{1.28}$$

where α is the absorption coefficient of the material at the energy of the incoming photon. The absorption of light in a semiconductor causes the optical power to decrease with distance. This effect is described mathematically by:

$$\frac{\mathrm{d}P_{\mathrm{opt(x)}}}{\mathrm{d}x} = -\alpha P_{\mathrm{opt(x)}} \tag{1.29}$$

The calculation of the generation rate of carriers therefore requires first a calculation of the optical power within the structure from which the generation rate can then be obtained using Eq. 1.28.

1.7 Principle of detectors

Photodetectors are semiconductor devices that convert the optical signal into electrical current. They have been used widely, in military applications (*e.g.* navigation, night vision, weapons detection) and commercial applications (*e.g.*, communications, aerospace, medical imaging), public applications (*e.g.*, atmospheric sounding, pollution control, meteorology, environmental monitoring), and academic applications (*e.g.*, astronomy). The operation principle of photodetectors is based on the quantum photoelectric effect: incident photons generate carriers, which contribute to the photocurrent or photovoltage. Their output depends on the number of absorbed photons. In order to initiate photoelectric emission, a certain minimum energy of the incident photon is required. Therefore, photondetectors show a wavelength dependence of response per unit of incident photon power.

There are a few dominant technologies for photodetectors in the market. The first type is based on HgCdTe (MCT) and InSb. Photodetectors based on these materials encountered weakness such as noise non-uniformity and cooling requirements for photondetector with wavelengths exceeding 3 µm. Cooling is important to avoid thermal generation of charge carriers. Non-cooled devices are very noisy because thermal transition competes with optical ones. To avoid this, the device must be cooled. The cooling requirement is the most common problem in the IR systems making them heavy, bulky and expensive. This created a need to invent a new group of materials to improve the photodetector performance.

Quantumwell IR photodetectors (QWIPs) is another existing IR technology have been used as an alternative solution. They must grow on lattice-matched expensive substrates (InGaAs, InAs, InSb) and suffer from high dark current, low quantum efficiency and lack of normal incidence absorption. QD IRPs based on III-V materials have some issues

in their growth and in the variability in the size and shape of the dots. Type-II super lattice (T2SL) has been developed in the area of device design because of their versatility in bandgap engineering which are not existing in other material systems. However, T2SL photodetectors have their own challenges, such as producing thick super lattice (SL) structure without degrading the material quality. Thick SL is necessary for achieving high quantum efficiency photodiode. Considerable surface leakage is a serious problem of in T2SL which results by the discontinuity in the periodic crystal structure. All the above drawbacks remain a problem for infrared photodetection.

Semiconductor nanowires (NWs) are a new class of materialsthat can improve the photodetection technology. The small footprint of NWs makes them readily release the strain induced by the lattice-mismatch without the generation of dislocations. This feature enables epitaxial growth on inexpensive Si substrates and therefore could solve the problems mentioned above.

1.7.1 Common type of photodetectors

Photodetectoris a device that convert incident optical signal into electric current. Photodetectors can be fabricated in many different ways. They can be *p*-*n* junction photodetectors, *p*-*i*-*n* diodes, metal-semiconductor diodes (or Schottky barriers) and heterojunction diodes. When photons strike the active region (depletion region) of the device, the photo-generated electron-hole pairs, which will be separated because of strong built-in electric field in the depletion region. This occurs without applying any external electric field. By applying reverse bias, the photo-generated carriers are swept apart to the opposite terminal of the applied electric field (holes to the cathode and electrons to the anode). Consequently, these carriers will contribute to the photo current of the external circuit. The photo detector devices may be reversely biased to improve the response speed; the devices also have a small area to ensure a low junction capacitance. Several other types

of photodetectors will be described in the next sections.

1.7.1.1 *p*-*i*-*n* photodetector

A *p*-*i*-*n* diode is a *p*-*n* junction with an extra-undoped layer sandwiched between *p*- and *n*-regions. The question that may be raised is why i-layer is required? In photodetector it is important to have a thick active region so that it absorbs all the incident photons. To further widen the depletion region that acts as an active region of the photodetector, intrinsic layer should be sandwiched between *p*- and *n*-side. Adding this layer will decrease the capacitance of the photodetector according to the fomulars:

$$C_{\mathrm{j}} = \epsilon \frac{A}{d} \tag{1.30}$$

Where C_{j} is the junction capacitance, ϵ is the dielectric constant, A is the area of depletion region in the device and d is the distance between positive and negative charge in the depletion region. Reducing the capacitance leads to a high frequency response according to the fomular:

$$f = \frac{1}{2\pi R C_{\mathrm{j}}} = \frac{d}{2\pi \epsilon A R} \tag{1.31}$$

Where f is the frequency, R is the resistance and C_{j} is the capacitance. Consequently, the speed of the photodetector will increase. In addition, when capturing area of the light (which represents *i*-layer) becomes larger, the efficiency of the device becomes higher due to better light absorption, which increases the responsivity of the photodetector increases.

1.7.1.2 Heterostructure photodetector

Heterojunction device can be formed by epitaxially depositing a semiconductor a large bandgap on a small bandgap semiconductor. The lattice mismatch between the two

materials should be very small in order to obtain heterojunction without dislocations. The heterojunction can be fabricated in different ways so that the material combinations can make the device parameters easily optimized. These device parameters include specific optical-signal wavelength, quantum efficiency, and response speed *et al.*.

1.7.1.3 Metal-semiconductor photodiode

This kind of detectors are particularly useful in the ultraviolet and visible light regimes of the spectrum. It consists of semiconductor materials with thin layer of metal ($\sim$ 10 nm) coated with anti-reflection layer. In order to ensure that all or most of the incident radiation is absorbed by the semiconductor surface, it is important to choose an appropriate metal and the anti-reflection coating for specific wavelength. For example, Au-Si photodetector with 10 nm gold and 50 nm anti-reflection (zinc sulphide) coating, can allow more than 95% of the incident light ($\lambda = 0.6328$ µm) transmit into the Si substrate.

1.7.2 Photodetector characterization parameters

When photodetector is designed there are main parameters of it should be measured to ensure that the device is working, such as quantum efficiency η, responsivity R_λ, impulse response t_r and noise equivalent power (NEP), and dark current. The details of each of these parameters are stated in the following.

1.7.2.1 External quantum efficiency

External quantum efficiency (EQE) is the fractional number of incident photon flux, which generate electron-hole pairs contributing to the photocurrent:

$$\eta = \frac{I_\mathrm{p}/q}{\phi} \tag{1.32}$$

where $I_{p/q}$ is is the photocurrent generated, q is the electron charge, ϕ is the flux of incident photons which is given by:

$$\phi = \frac{P_{opt}}{h\nu} \tag{1.33}$$

where P_{opt} is the incident optical power and $h\nu$ is the photon energy. Making use of Eq. 1.32 & 1.33, the quantum efficiency can be obtained as:

$$\eta = \frac{hI_p}{q\phi} \tag{1.34}$$

1.7.2.2 Internal quantum efficiency

Internal quantum efficiency (IQE) is the ratio of generated electron-hole pairs, which contribute to the photocurrent, per absorbed photon. This efficiency excludes the photons reflected from or transmitted through the device. The EQE can be expressed in terms of IQE as follows:

$$\eta = \eta_i(1 - R)[1 - \exp(-\alpha d)] \tag{1.35}$$

where η_i is the IQE, R is the reflectance, R is the absorption coefficient, and d is the width of the absorption area (active region). It can be noticed according to Eq. 1.35 that the factors affecting the EQE are η_i, R, α, and d. Therefore, to maximize EQE, η_i should be increased, materials should be chosen to increase α, and anti-reflection layer should be applied on to the device.

1.7.2.3 Responsivity

The ratio of the electric power generated to the incident optical power gives the responsivity:

$$R_\lambda = \frac{I_\mathrm{p}}{q} \tag{1.36}$$

By substituting Eq. 1.34, the responsivity will be given by

$$R_\lambda = \eta \frac{q}{h\nu} \tag{1.37}$$

It can be noticed that R_λ depends on the EQE of the photodetector and the energy of incident photons.

1.7.2.4 Noise equivalent power

It is the weakest detectable signal per square root of bandwidth for a given detector. There are many factors cause the noise in detectors such as dark current. Dark current is generated when the detector operates under electric field without light source, diffusion current due to Auger or radiative recombination in *n*- or *p*-region, generation and recombination in depletion region and BtB current. Another source of noise is surface states, which trap the generated carriers, causing non-radiative recombination.

1.8 Nanowires

1.8.1 The significance of Nanowires

Nanowires (NWs) are 1-D structures with length of the order of few microns and diameter in the range of tens to hundreds of nanometres. NWs have exhibited attractive physical properties that are not available in bulk materials, such as electrical carrier confinement in two dimensions of the NWs. Quantum confinement becomes significant when the wavelength of the electron wavefunction in a material is of the same dimension

as the material. This means that the motion of the electrons be comes quantized in the confining dimension. This implies that the energy levels of NWs will be discrete instead of continuous as found in bulk materials, as shown in Fig. 1.21. All the above features make NWs favorable to opto-electronic applications. For instance, NWs have demonstrated enhanced light absorption, efficient carrier separation and collection, leading to applications in NWs solar cells, InAs NWs photodetectors, InAs NWs phototransistors, and field-effect transistors.

1.8.2 Quantum theory in 1-D nanowires

1.8.2.1 Density of states in 1-D nanowires

It has been known that any reduction of dimensionality of materials results low dimensional materials, in which confined electrons (or holes) lead to a dramatic change in their behaviour. The general 3-D Schrödinger Eq. 1.3 for constant effective mass could be written as:

$$-\frac{\hbar^2}{2m^*}\nabla^2\psi(x,y,z) + V(x,y,z)\psi(x,y,z) = E\psi(x,y,z) \tag{1.38}$$

in a Cartesian coordinate system.

Fig. 1.21 shows the difference between density of states in bulk materials and low dimensional materials. Density of states per unit length in 1-D materials could be presented as:

$$D_{1-\mathrm{D}}(E) = \frac{2}{h}\sqrt{\frac{2m}{E}} = \frac{2}{h\nu(E)} = \frac{2}{\pi}\left(\frac{\mathrm{d}E}{\mathrm{d}k}\right)^{-1} \tag{1.39}$$

1.8.2.2 Quantum confinement in 1-D NWs

1-D nanowires have confined cross-sectional planes and an infinite length positioning along x-axis. So it is possible to decouple the motion into x-axis and y, z-plane. The total

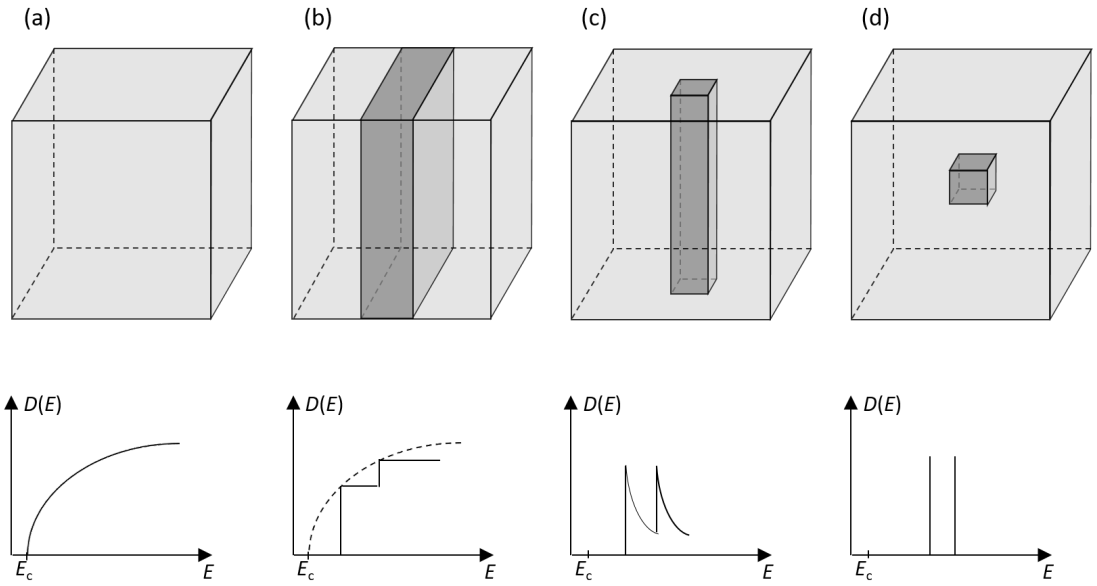

Figure 1.21: Schematic of effect of electronic confinement on the density of states moving from (a) bulk to (b) 1-D confinement in a quantum well, (c) 2-D confinement in a quantum wire, and (d) 3-D confinement in a quantum dot.

potential $V(x, y, z)$ and wave function $\psi(x, y, z)$ could be written as:

$$V(x, y, z) = V(x) + V(y, z) = V(y, z) \tag{1.40}$$

considering $V(x) = 0$ for NWs with infinite length.

$$\psi(x, y, z) = \psi(x) + \psi(y, z) \tag{1.41}$$

By substituting both Eq. 1.40 and Eq. 1.41 into Eq. 1.38, we get the two equations in x-direction and y, z-plane:

$$-\frac{\hbar^2}{2m^*}\frac{\partial^2\psi(x)}{\partial x^2} = E_x\psi(x) \tag{1.42}$$

$$-\frac{\hbar^2}{2m^*}\left[\frac{\partial^2\psi(y,z)}{\partial y^2} + \frac{\partial^2\psi(y,z)}{\partial z^2}\right] + V(y,z)\psi(y,z) = E_{y,z}\psi(y,z) \tag{1.43}$$

It is easy to show the solution of Eq. 1.42 that:

$$E_x = \frac{\hbar^2 {k_x}^2}{2m^*} \tag{1.44}$$

The second Eq. 1.43 in y, z-plane presents the Schrödinger equation for the 2-D confinement potential characterizing NWs, and could be solved by using a full 2-D solution. To study the confined energy of NWs, special cases of the solution of Eq. 1.43, for the relevant or similar geometries in this work, will be illustrated later, such as circular cross-sectional NWs. Such particular solution relies on the ability of further decoupling the motion into independent components.

For circular cross-section NWs as an example , seeing the cylindrical symmetry of the NW shown in Fig. 1.8.2.2, we can write the Cartesian coordinates in the form of:

$$y = r\sin(\theta) \tag{1.45}$$

$$z = r\cos(\theta) \tag{1.46}$$

and

$$r = \sqrt{y^2 + z^2} \tag{1.47}$$

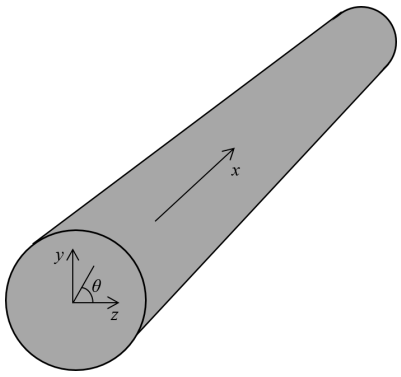

Figure 1.22: Schematic illustration of a circular cross-section NW.

Thus, the total potential $V(y,z)$ and wave function $\psi(y,z)$ could also be written in the term of the new variables r and θ. In addition, the circular symmetry the total potential and wave function should not have a dependence on the angle θ. So the Schrödinger equation follows as:

$$-\frac{\hbar^2}{2m^*}\left(\frac{\partial^2}{\partial y^2}+\frac{\partial^2}{\partial z^2}\right)\psi(r)+V(r)\psi(r)=E_r\psi(r) \tag{1.48}$$

By using the following mathematical transformation relation:

$$\frac{\partial^2}{\partial y^2}\psi(r)=\frac{1}{r}\frac{\partial}{\partial r}\psi(r)-\frac{y^2}{r^3}\frac{\partial}{\partial r}\psi(r)+\frac{y^2}{r^3}\frac{\partial^2}{\partial r^2}\psi(r) \tag{1.49}$$

$$\frac{\partial^2}{\partial z^2}\psi(r)=\frac{1}{r}\frac{\partial}{\partial r}\psi(r)-\frac{z^2}{r^3}\frac{\partial}{\partial r}\psi(r)+\frac{z^2}{r^3}\frac{\partial^2}{\partial r^2}\psi(r) \tag{1.50}$$

and

$$\left(\frac{\partial^2}{\partial y^2}+\frac{\partial^2}{\partial z^2}\right)\psi(r)=\frac{1}{r}\frac{\partial}{\partial r}\psi(r)+\frac{\partial^2}{\partial r^2}\psi(r) \tag{1.51}$$

Therefore, the final form of the Schrödinger equation becomes:

$$-\frac{\hbar^2}{2m^*}\left(\frac{1}{r}\frac{\partial}{\partial r}+\frac{\partial^2}{\partial r^2}\right)\psi(r)+V(r)\psi(r)=E_r\psi(r) \tag{1.52}$$

From the above form of Schrödinger equation, reliance has been made on the specific form of the kinetic energy operator, hence this Schrödinger equation is only valid for a constant effective mass.

Fig. 1.23 displays the results of calculations of the electron confinement energy versus the wire radius, for a GaAs NW surrounded by $Ga_{0.8}Al_{0.2}As$, for constant effective mass. It is easy to understand, the confinement energy decreases as the radius increases and the even-parity eigenstate is of lower energy than the odd [26].

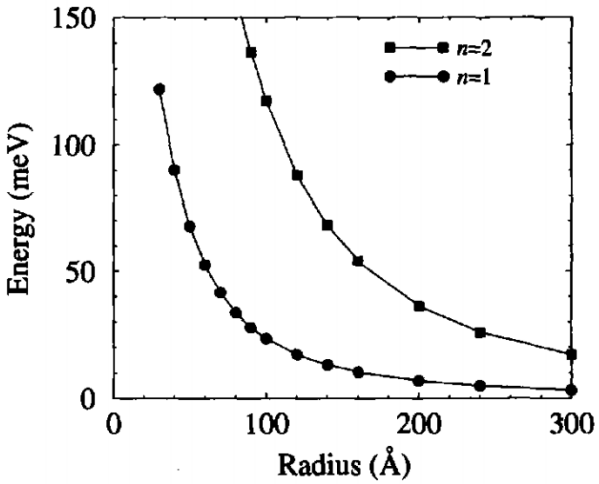

Figure 1.23: The confinement energy in a finite barrier circular cross-section NW.

Equation 1.53 shows the energy consists of the bulk material bandgap and another part related to quantum confinement.

$$E = E_{\mathrm{g}} + \frac{2\hbar^2\xi^2}{d^2}\left(\frac{1}{m_{\mathrm{e}}} + \frac{1}{m_{\mathrm{h}}}\right) \tag{1.53}$$

where E_{g} is the bulk bangap, ξ is the zero-point of the cylindrical Bessel function (2.4048), d is the diameter of the nanowires and m_e=0.042 and m_h=0.084 the effective electron and hole masses, respectively for InAs.

1.8.2.3 Emission from real NWs samples

The morphology of the real as-grown NWs is not uniform, and the length and diameter will affect the quantum confinement of in NWs. Fig. 1.24 shows an example. Quantum confinement causes the wavelength of the light shift toward high energy. Quantum confinement in uneven NWs is not uniform, so the offsets of energy are not the same, eventually leading to the broadening of the emission spectrum.

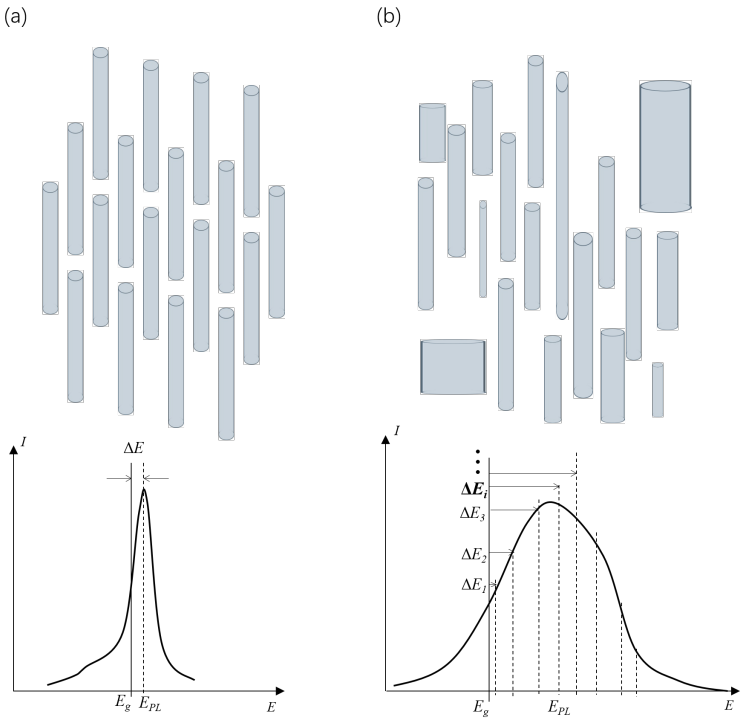

Figure 1.24: Ideal quantum dots, exhibiting perfect uniformity and resonant density of states for all electronic states and optical transitions (a). The effect of structural and compositional inhomogeneity (b) is to introduce an inhomogeneous broadening to these states and transitions.

1.8.3 The challenges of nanowires

Although there are a number of advantages of using NWs grown on silicon substrates, several challenges still stand in the way of further improvement of NW device performance, in particular the crystalline quality, surface states, efficient recombination and quantum confinement. It is difficult to control the geometry and density of NWs, stacking faults, and the variations in stacking that produce mixed phases of WZ & ZB [27]. These difficulties can be controlled through optimized growth conditions and the use of impurities [28] and surfactants [29]. Due to the huge surface area-to-volume ratio of NWs, the surface states significantly degrade their optical and electronic properties and impede their use in opto-electronic devices [30]. This problem could be eliminated through engineering a chemically in active surface to produce a proper surface passivation hence to prevent the formation

of surface states. Several approaches have been developed including coating the surface with polymers [31], treating the NWs with chemicals solution [32], and monolithic growth of a shell layer to encapsulate the core NWs [33]. Amongst these approaches, the latter offers several advantages *e.g.*, avoiding the risk of contamination and oxidation in device processing, providing a bandgap engineering capability and efficient quantum confinement if appropriate materials combinations are realized.

1.8.4 The growth of Nanowires

There are two basic approaches to synthesizing NWs: top-down and bottom-up. A top-down approach reduces a large piece of material to small pieces, by various means such as lithography, milling or thermal oxidation. A bottom-up approach synthesizes the nanowire by combining constituent adatoms. Most synthesis techniques use a bottom-up approach. Initial synthesis via either method may often be followed by a nanowire thermal treatment step, often involving a form of self-limiting oxidation, to fine tune the size and aspect ratio of the structures.[5]

Nanowire production uses several common laboratory techniques, including suspension, electrochemical deposition, vapor deposition, VS / VLS growth, and even template methods. Ion track technology enables growing homogeneous and segmented nanowires down to 8 nm diameter [34, 35]. As nanowire oxidation rate is controlled by diameter, thermal oxidation steps are often applied to tune their morphology.

1.8.4.1 The vapor-liquid-solid method

A common technique for creating NWs is vapor-liquid-solid (VLS) method, which was first reported by Wagner and Ellis in 1964 for silicon whiskers with diameters ranging from 100s of nm to 100s of µm [36]. VLS synthesis requires catalyst. For NWs, the best catalysts are liquid metal (such as gold) nanoclusters, which can either be self-assembled

from a thin film by dewetting, or purchased in colloidal form and deposited on a substrate. This method uses a source materials, which is suitable for metal-organic chemical vapor deposition (MOCVD) and molecular beam epitaxy (MBE) techniques. The source enters these catalyst and begins to saturate them. On reaching supersaturation, the source solidifies and grows outward from the nanocluster. Simply turning off the source can adjust the final length of the nanowire. Switching sources while still in the growth phase can create compound nanowires with super-lattices of alternating materials.

1.8.4.2 The vapor-solid-solid method

Similar to VLS synthesis, vapor-solid-solid (VSS) synthesis of NWs proceeds through thermolytic decomposition of a precursor. Unlike VLS, the catalytic seed remains in solid state when subjected to high temperature annealing of the substrate. This such type of synthesis is widely used to synthesise metal silicide/germanide nanowires through VSS alloying between a copper substrate and a silicon/germanium precursor.

1.8.4.3 The vapor-solid method

Unlike VLS and VSS, NWs can be also grown without the help of catalysts via VS method. The precursor reach the two terminals of NWs, and start to form new layers of NWs at the terminals other than the sidewalls. The NWs systhesized vis VS method has high purity because there is no external catalyst.

1.9 Motivation of this work

III-V semiconductors have leapfrogged developments and remarkable applications over the past few decades on luminescence, detection, information transmission, com-

putation, and energy harvesting. However, limitations such as the requirement of lattice match hinder the design of the device structure and the realization of material growth. Molecular beam epitaxy brings possibilities to novel quantum structures. Among them, low dimensional materials based on 1-D nanowires show great promise. 1-D nanowires have received extensive attention due to their unique advantages: The small diameter helps to overcome the limitations of the lattice match, and inexpensive silicon wafers can be used as a substrate, expanding the range of use. The high area-to-volume ratio results in a stronger surface effect, a closer interaction with the outside world, and a stronger absorption. The specific growth process facilitates the formation of a variety of hetero-junctions, making the structural design more flexible, such as the introduction of ternary alloys to achieve energy band engineering.

Starting from Au-assisted growth, the growth of nanowires flourished, and for the III-V NWs, the self-catalysed method was developed. To the current research, the growth of nanowires and heterogeneous structures is still ambiguous, the exploration of the structure and optical properties of nanowires is far from complete, and the development of devices and applications can not meet the needs.

Since the bandgaps of materials such as InAs, InSb, and GaSb are less than 1 eV, they and their alloy nanowires are expected to be suitable for dry-fiber-optic communication and gas detection. This work will concentrate on arsenic-containing nanowires, with a focus on material growth, structural regulation, performance characterization, and device construction, in order to obtain quantum heterostructures with excellent performance near the telecommunication characteristic wavelength. Specifically, it contains the following sections:

1. Study and optimize the growth of InAs NWs and GaAs NWs, clarify the role of the oxide layer on the surface of the silicon wafer, explore the influence of the doping species of the silicon on the optical properties of the nanowire, for the discover the device

performance.

2. Study the growth, compositional regulation, structural changes and optical properties of Sb-containing InAsSb NWs.

3. Study the construction and device performance of InAs/AlSb and InAs/InGaAs core-shell heterojunction nanowires, and compare the difference between In and Ga for nanowire growth.

4. Study the axial heterostructure based on Sb-containing GaAs NWs, to obtain excellent optical properties through the axially embedded nano disk heterostructure.

Chapter 2

Experimental technics and characterization methods

2.1 Molecular Beam Epitaxy

Molecular beam epitaxy (MBE) is a method of growing single crystal materials and was invented by J. R. Arthur and Alfred Y. Cho of Bell Laboratories in the late 1960s [37]. Molecular beam epitaxy is carried out in an environment of high vacuum or ultra-high vacuum (UHV, 10^{-8} Pa). The term "(molecular) beam" means that the gas atoms in the process do not interact and do not react with the UHV chamber material unless they are in contact with the wafer. This is because these gases have a longer mean free path. The most important aspect of molecular beam epitaxy is its low deposition rate, which typically causes the film to epitaxially grow at a rate of less than 1000 nm/h. Such low deposition rates require a high degree of vacuum to achieve the same level of cleanliness in other deposition methods.

Some systems need to cool the bottom layer. The UHV environment of the growth chamber must be maintained using a cryopump and ion pump as shown in Fig. 2.1, while liquid nitrogen or low-temperature nitrogen can cool the internal temperature to 77 K. The low temperature environment can further reduce the content of impurities in the vacuum, providing better conditions for depositing thin films. In other systems, crystal

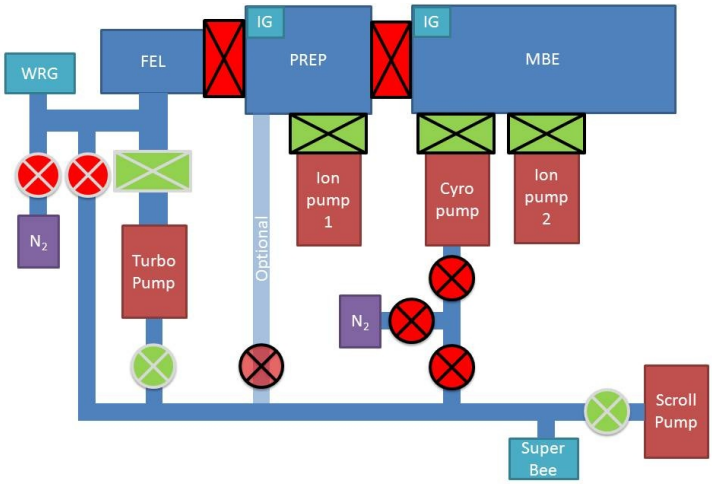

Figure 2.1: Schematic diagram illustrating the structure of a MBE system.

grown wafers may be mounted on a rotating disk that can be heated to a few hundred degrees Celsiu as the schematic diagram of typical MBE system [38] shows in Fig. 2.2.

During molecular beam epitaxy of solid sources, elements such as Ga and As are heated in ultra-pure form in separate effusion cells until they begin to sublimate slowly. These gaseous materials then condense on the hot wafer and they interact there. Taking Ga and As as examples, the above effects can produce single crystal GaAs.

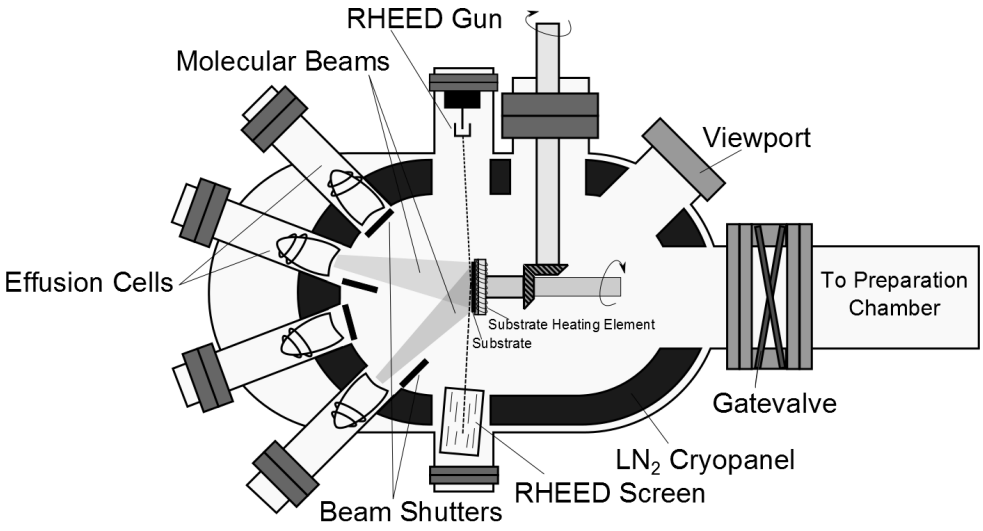

Figure 2.2: Schematic diagram illustrating the structure of a typical grwoth chamber in a MBE system.

In the epitaxy process, Reflection high-energy electron diffraction (RHEED) is often used to detect the progress of crystal gradation. A computer is able to control the beam flux in the reaction chamber, enabling precise control of each level with a single layer of atoms. The fluxes from the material sources can not be directly measured in the MBE system. The reading of beam equivalent pressure (BEP) is proportional to the flux arriving at the sample surface and hence the growth rate. In the calibration stage, for group-III material, the BEP dependence on cell temperature is measured. And for group-V material, the values of BEP is measured with different valve positions. By comparing the BEP values, the cell temperature or valve positon can be adjusted to obtain the desired growth rate. Fine structures of different material layers can be produced in this way. This type of control can bind electrons in a certain space, producing quantum wells, NWs and quantum dots. These structures described above are critical to many modern semiconductor devices, including laser diodes, detectors and LEDs. The latest MBE technology is also used in the deposition of oxide materials, 2-D materials, and topological insulators [39–44].

2.2 Contact angle

Contact angle means the angle formed by the liquid/gas interface contacting the solid surface. The contact angle is a system that interacts by three different interfaces. The most common conceptual explanation is that a small droplet is in the solid surface of a unit lateral direction, the shape of the water droplet defined by the Young's-Laplace equation, and the contact angle plays a constraint. The contact angle measurement can be measured by a contact angle protractor. A droplet on a solid surface, if the liquid is strongly stressed by a solid surface (such as water and a surface of a strongly hydrophilic solid), the droplet will tend to flatten on the solid surface while it is in contact The angle

is small. Instead of a strongly hydrophilic solid, the contact angle will be larger. On many highly hydrophilic surfaces, water droplets are expressed from 0° to 30°. For highly hydrophobic surfaces, the contact angle to water can be high. On this surface, the water droplets only stay on it, rather than actually infiltrating the surface. It can be called superhydrophobic. We can observe it on the surface which is properly fluorinated, and it can be called the lotus effect [45].

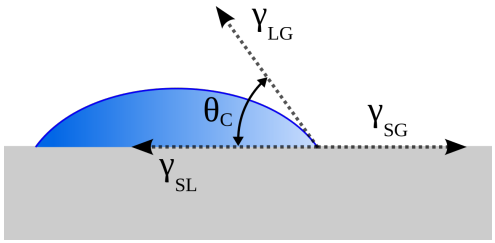

Figure 2.3: Schematic diagram illustrating the contact angle of liquid on solid in gas.

The surface of fresh Si is hydrophobic. In the atmospheric environment, there is a natural oxide layer on the surface of the silicon wafer, which is hydrophilic, showing that the oxide layer is about complete and the hydrophilicity is better. Due to this connection, the strength of the hydrophilicity can be expressed by the size of the contact angle, thereby comparing the surface oxide layer.

2.3 Atomic force microscopy

An atomic force microscope (AFM), also known as a scanning force microscope (SFM), is a nanometer-scale high-resolution scanning probe microscope that is 1000 times better than the optical diffraction limit. The typical configuration is shown in Fig. 2.4 [46]. AFM is the most important tool for manipulating materials at the nanoscale and for their imaging and measurement. The information is collected by the microcantilever

sensation and the "feel" of the surface of the sharp probe on the cantilever, while the piezoelectric element can control the very precise minute movement of the sample or scanner. The microcantilever is used to sense and amplify the force between the sharp probe on the cantilever and the atom of the sample to be tested, and has an atomic resolution. The atomic force microscope was formerly a scanning tunneling microscope. The biggest difference between AFM and scanning tunneling microscopy (STM) is that it does not use electron tunneling effects, but detects the contact between atoms, atomic bonding, van der Waals force or Casimir effect, *etc.*. to present the surface characteristics of the sample. Because the atomic force microscope can observe both the conductor and the non-conductor, it can make up for the shortcomings of the scanning tunneling microscope.

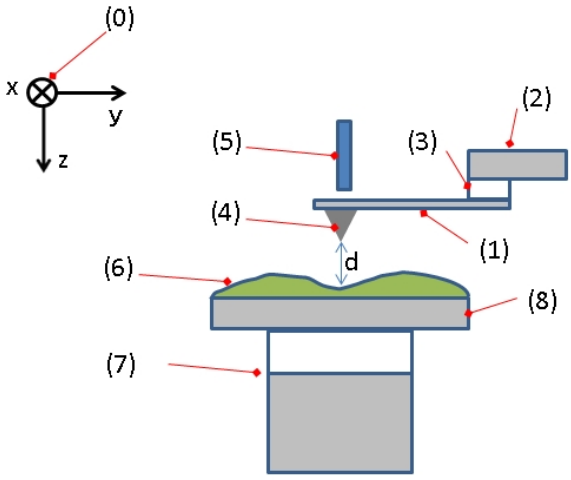

Figure 2.4: Typical configuration of an AFM setup. (1) Cantilever, (2) Support for cantilever, (3) Piezoelectric element(to oscillate cantilever at its eigen frequency.), (4) Tip (Fixed to open end of a cantilever, acts as the probe), (5) Detector of deflection and motion of the cantilever, (6) Sample to be measured by AFM, (7) xyz drive, (moves sample (6) and stage (8) in x, y, and z directions with respect to a tip apex (4)), and (8) Stage.

AFM can operate in different modes. These modes can be divided into static mode (also known as contact mode), or a series of other dynamic modes, such as non-contact mode, tapping mode, and lateral force mode.

AFM has many advantages over scanning electron microscopy. Unlike electron mi-

croscopy, which only provides 2-D images, AFM provides a true 3-D surface map. At the same time, AFM does not require any special treatment of the sample, such as copper or carbon, which can cause irreversible damage to the sample. Third, the electron microscope needs to be operated under high vacuum conditions, and the atomic force microscope can work well under normal pressure even in a liquid environment. This can be used to study biological macromolecules, even living biological tissues. It is like a blind person touching the image, slowly touching on the surface of the object, the shape of the atom is very intuitive. Compared with scanning electron microscope, AFM has the disadvantage that the imaging range is too small, the speed is slow, and it is too much affected by the probe.

In this work, AFM is used to characterize the morphology of metal catalyst on the surface of silicon substrate.

2.4 Scanning Electron Microscope

Scanning electron microscope (SEM) is an electron microscope that produces an image of a sample surface by scanning a surface of the sample with a focused electron beam as Fig. 2.5 [47] shows. The electrons interact with atoms in the sample to produce a variety of signals containing information about the surface topography and composition of the sample. The electron beam is typically scanned in a raster scan pattern and the position of the beam is combined with the detected signal to produce an image. Scanning electron microscopy can achieve resolutions better than 1 nanometer. Samples can be observed under high vacuum, low vacuum, wet conditions (using an environmental SEM) and a wide range of low or high temperatures.

The most common SEM mode is the detection of secondary electrons emitted by atoms excited by an electron beam. The number of secondary electrons that can be

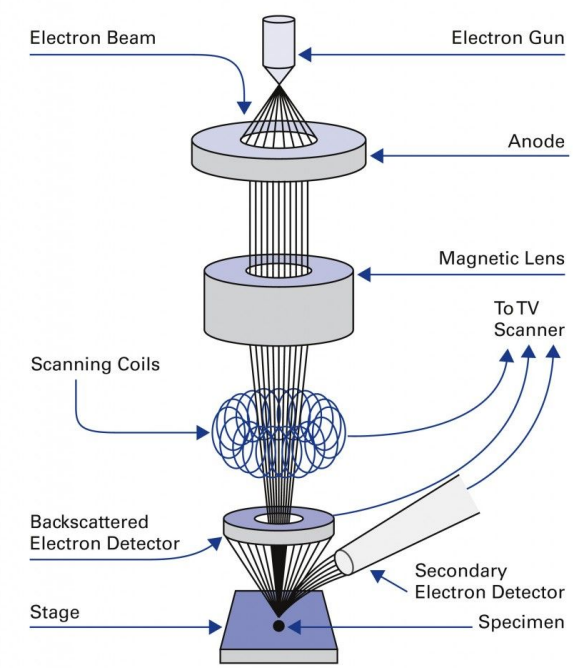

Figure 2.5: Schematic drawing the fundamental of SEM.

detected depends on the morphology of the sample and the other factors. An image showing the topography of the surface is created by scanning the sample and collecting the emitted secondary electrons using a special detector. It can also produce high-resolution images of the surface of the sample, and the image is three dimensional, identifying the surface structure of the sample.

2.5 Transmission electron microscope

Transmission electron microscope (TEM) projects an accelerated and concentrated electron beam onto a very thin sample. A typical image of TEM setup is shown in Fig. 2.6 (a) and the fundamental is shown in Fig. 2.6 (b) [48]. The electrons collide with atoms in the sample to change direction, resulting in solid angle scattering. The size of

the scattering angle is related to the density and thickness of the sample, so that images with different brightness and darkness can be formed, and the image will be displayed in the image after being enlarged and focused. Since the electron De Broglie wavelength is

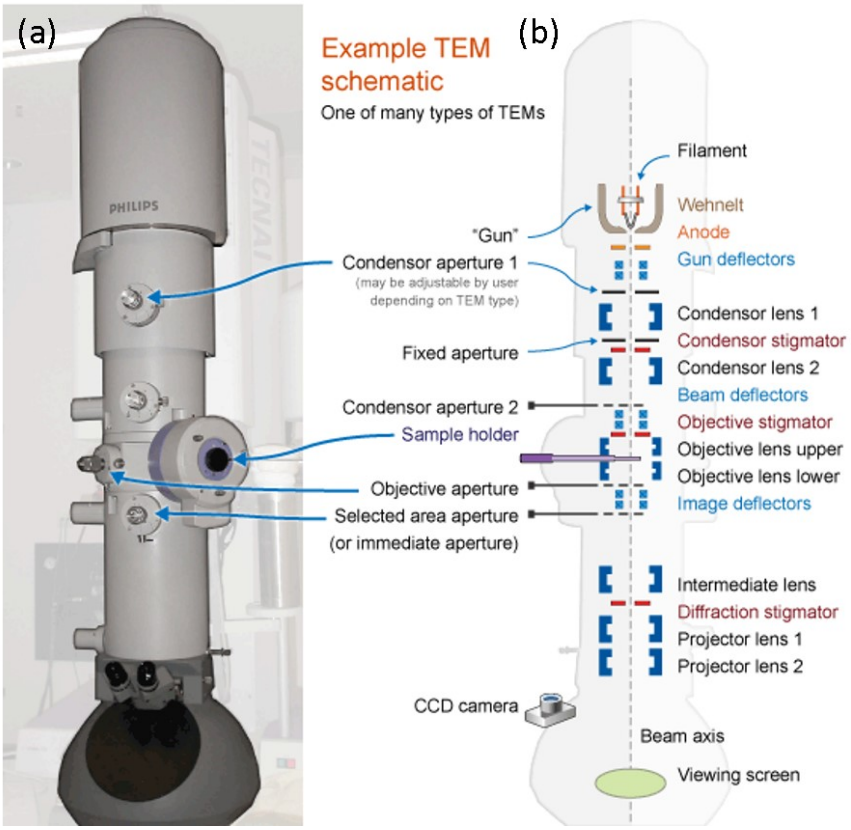

Figure 2.6: Image of TEM setup and schematic drawing of the fundamental of TEM.

very short, the resolution of the transmission electron microscope is much higher than that of the optical microscope, and can reach 0.1 to 0.2 nm, and the magnification is tens of thousands to millions of times. Therefore, the use of transmission electron microscopy can be used to observe the fine structure of the sample, and can even be used to observe the structure of only one column of atoms, which is tens of thousands times smaller than the smallest structure that can be observed by optical microscopy. At lower magnifications, the contrast of TEM imaging is primarily due to the different absorption of electrons due to the different thicknesses and compositions of the material. When the magnification

factor is high, complex fluctuations will cause different brightness of the image, so professional knowledge is needed to analyze the image obtained. By using different modes of TEM, the sample can be imaged by the chemical properties of the material, the crystal orientation, the electronic structure, the electronic phase shift caused by the sample, and the usual electron absorption. The most common mode of operation for TEM is the bright field imaging mode. In this mode, the classic contrast information is obtained from the absorption of the electron beam by the sample. Thicker areas in the sample or areas with more atoms have more electron absorption, so they appear darker on the image, while areas with smaller electron absorption appear brighter. This is also the term bright field. origin. The image can be thought of as a 2-D projection of the sample along the optical axis and can be approximated using Beer's law [49]. A more sophisticated analysis of the bright field mode requires consideration of the phase information of the electron wave as it passes through the sample [25].

Since Bragg scattering occurs when an electron beam is injected into the sample, the diffraction contrast information of the sample is carried by the electron beam. For example, a crystal sample will scatter the electron beam onto discrete points on the back focal plane. By placing the aperture on the back focal plane, a suitable reflected electron beam can be selected to observe the image of the desired Bragg scattering. Usually only a very small number of samples cause electron diffraction to be projected onto the imaging device. If the selected reflected electron beam does not include an unscattered electron beam at the focal point of the lens, then the area where no sample scatters the electron beam on the image, *i.e.*, the area without the sample, will be dark. Such an image is called a dark field image. Modern TEMs are often equipped with fixtures that allow the operator to tilt the sample at an angle to achieve specific diffraction conditions, and an aperture is placed over the sample to allow the user to select an electron beam that can enter the sample at a suitable angle. This imaging method can be used to study crystal lattice defects.

By carefully selecting the direction of the sample, it is possible to determine not only the position of the crystal defect but also the type of the defect. If a particular crystal plane of a sample is only a little smaller than the strongest diffraction angle, any crystal plane defect will produce a very strong contrast change. However, atomic dislocation defects do not change the Bragg scattering angle and therefore do not produce strong contrast [50]. The analysis of the point-to-point of the diffraction pattern is very complicated. Although the contrast of the grid image can be quantitatively explained, the analysis is very complicated in nature and requires a lot of computer simulation to calculate, for example, the Kikuchi line caused by multiple diffraction of the crystal lattice point [47], but it can provide more structural information of the sample, even information beyond the structure.

2.6 Energy-dispersive X-ray spectroscopy

Energy-dispersive X-ray spectroscopy (EDX) is an analytical tool for elemental analysis and chemical characterization. The means analyzes by collecting X-rays generated by an X-ray machine or other X-ray source and X-rays emitted when the sample interacts. Since different elements have different emission spectra due to different atomic structures, the X-ray spectrum can be used to distinguish the different components contained in the sample [51]. The characteristic X-rays that excite the sample generally require electron beams, proton beams or X-rays that are very energetic. First, the incident electrons (or protons, photons) excite the inner electrons of the ground state atoms. The inner electrons leave holes after leaving the atom. When the outer, high-level electrons fill these low-level holes, the excess energy may be emitted as X-rays. The energy dispersive X-ray spectrometer collects and measures the energy and intensity of these X-rays. Since the energy

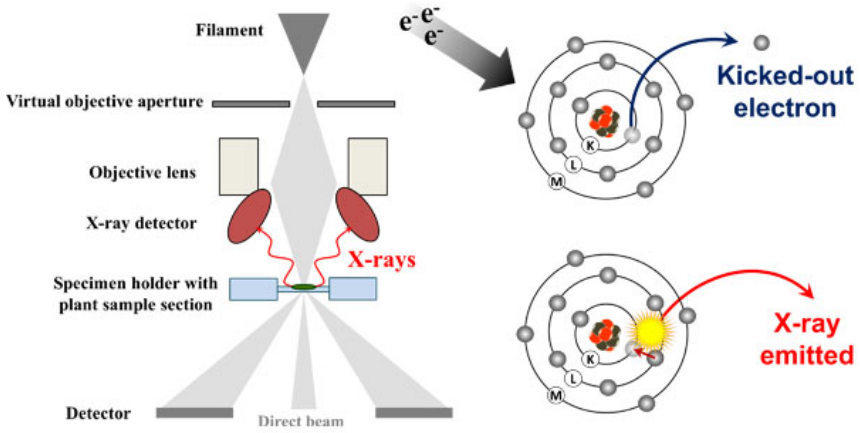

Figure 2.7: Schematic drawing and the principle of EDX.

distribution of these X-rays can reflect the atomic characteristics of a particular element, an energy dispersive X-ray spectrum can be used to determine the elemental composition in a sample [51].

2.7 Photoluminescence

Photoluminescence (PL) is a type of cold luminescence, which refers to the process in which a substance absorbs photons (or electromagnetic waves) and re-radiates photons (or electromagnetic waves). From the theory of quantum mechanics, this process can be described as the process in which a material absorbs a photon transition to a higher energy level and returns to a lower energy state, while releasing photons. PL can be classified into fluorescence and phosphorescence according to the delay time. Photoexcitation causes an electronic transition inside the material to an allowed excited state. When these electrons return to their thermal equilibrium state, excess energy can be released through the illuminating process and the non-radiative process. The energy of PL is related to the difference

in energy levels between the two electronic states, which involves a transition between the excited state and the equilibrium state. The amount of excitation light is related to the contribution of the radiation process.

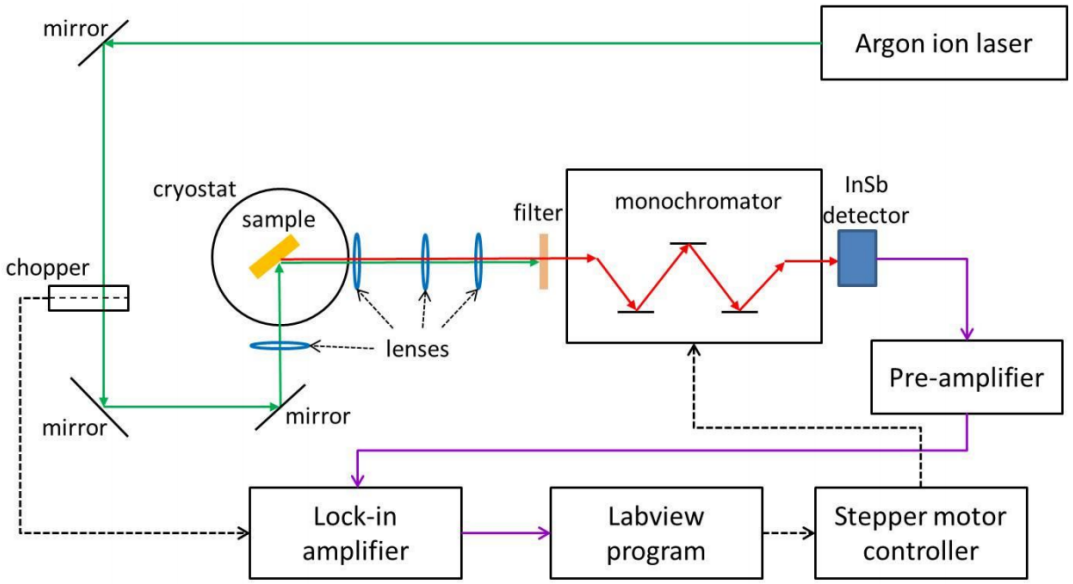

Figure 2.8: Schematic drawing of a PL measurement setup. Green lines: Ar laser optical path; red lines: PL emission optical path; purple lines: detected signal flow; dashed back lines: electronic control signal flow.

Photoluminescence is a method of detecting the electronic structure of a material that is not in contact with the material and does not damage the material. Light is directly incident on the material, absorbed by the material and transferred to the material. This process is called photoexcitation. This excess energy can be consumed by the form of illumination. The process of illuminating due to photoexcitation is called photoluminescence. The spectral structure and intensity of photoluminescence are direct means of measuring many important materials. Photoluminescence can be applied to: bandgap detection, impurity level and defect detection, composite mechanism and material quality identification.

2.8 Fourier Transform Infra-Red Spectrometer

Fourier Transform Infra-Red (FTIR) Spectrometer is mainly composed of infrared light source, Michelson interferometer (beam splitter, movable mirror, fixed mirror), sample chamber, detector and computer as shown in Fig. 2.9. Its principle is different from the dispersive infrared spectroscopy. It is an infrared spectrometer developed based on the principle of Fourier transform of infrared light after interference. The main function of the

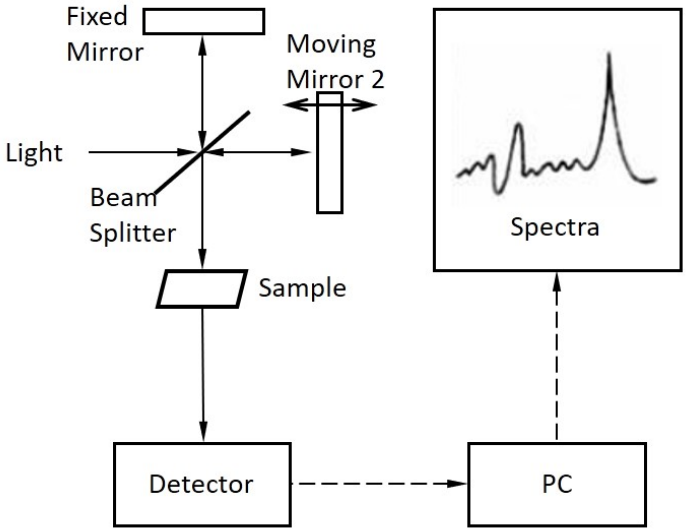

Figure 2.9: Schematic drawing of a FTIR measurement setup.

Michelson interferometer is to split the light emitted by the light source into two beams to form a certain optical path difference, and then recombine them to generate interference. The obtained interferogram function contains all the frequency and intensity information of the light source. Using a computer to Fourier transform the interferogram function, the distribution of the intensity of the original light source according to frequency can be calculated. There are few components used, no grating or prism splitter, which reduces the loss of light, thus it overcomes the shortcomings of the dispersive spectrometer, results in high signal-to-noise ratio, good reproducibility, and fast scanning speed.

Chapter 3

Role of droplets and SiO_2 layer in the growth of InAs NWs and GaAs NWs

3.1 Gold assisted growth of NWs via MBE

Gold (Au) assisted growth for NWs is a commonly used method in MBE and MOCVD. Au nanoparticles are required to alloy and initiate the growth of NWs. There are two common ways to form qualified nanoparticles. The first way is to deposit the synthesized nanoparticles onto the silicon wafer via mechanical methods such as spin-coating. The second way is to deposit a thin film on the surface of the silicon wafer and then anneal it. After annealing at a proper temperature, the Au film breaks and then Au nanoparticles form randomly on the surface of the silicon wafer.

Fig. 3.1 shows the steps of the growth progress. In Fig. 3.1 (a), the nanoparticles are positioned on Si substrate, in Fig. 3.1 (b), the precursors (such as Ga and As for GaAs NWs) are introduced and co-melt into the liquid Au droplets at proper substrate temperature. With the continual addition of the precursors, the precursors in the nanoparticles supersaturates and begin to crystallize into crystals of the desired composition at the interface of the nanoparticles with the silicon substrate, which is the initial of growth as shown in Fig. 3.1 (c). The precursors are continuously incorporated into the nanoparticles and crystallize at the interface between the nanoparticles and the new formed crystal, causing

the crystal to grow longer and the nanoparticles to be constantly elevated, thus the NWs grow longer untill the progress is terminated by stopping the supply of the precursors.

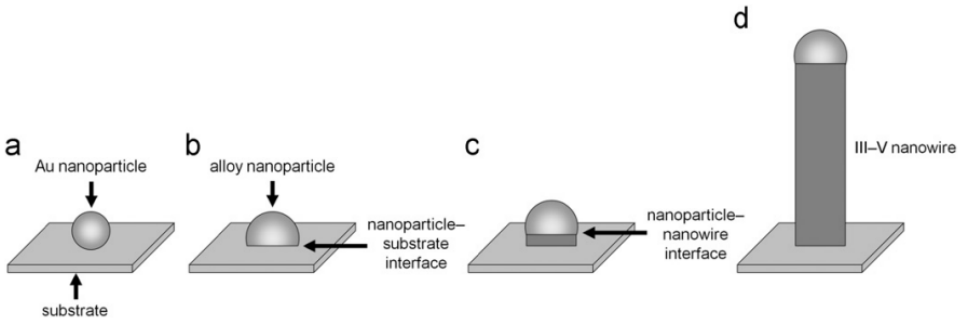

Figure 3.1: Schematic diagram illustrating the steps of nanowires growth via Au assisted method.

During the growth process, the gaseous precursors enter the nanoparticles to form liquid eutectic, which is continuously crystallized into new solid crystal at the interface between the liquid eutectic and the nanowire due to supersaturation. This method from gaseous to liquid to solid is called vapor-liquid-solid (VLS) mode. The VLS mechanism was proposed in 1964 as an explanation for silicon whisker growth from the gas phase in the presence of a liquid gold droplet placed upon a silicon substrate [36]. And now it is widely used for the growth of III-V group NWs. This Au assisted VLS mode is simple, but it also has disadvantages. First, the position of the nanowires is random, and second, the introduction of Au will form a slight doping in the nanowires resulting in a impurity related deep energy level.

3.2 Selective area growth of GaAs NWs via self-catalyzed MBE

In order to overcome the above two shortcomings, a new Au-free method has been proposed in this section. Taking GaAs NWs grown in this way as an example, Au is replaced by Ga itself, and its position is also predetermined.

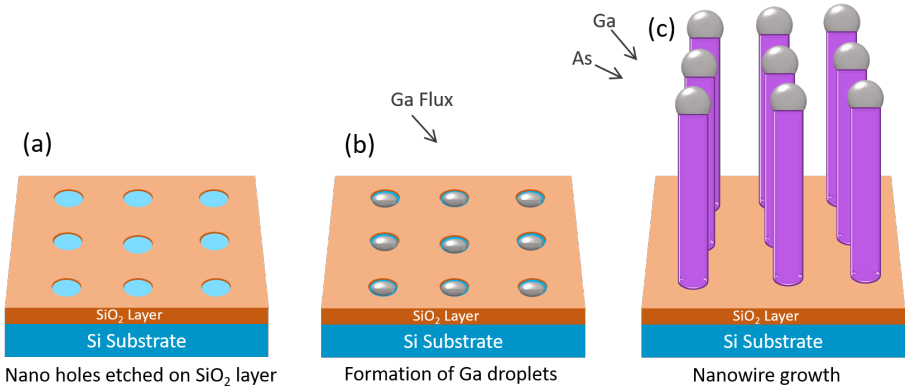

Figure 3.2: Schematic diagram illustrating the steps of selective area growth of GaAs NWs via self-catalyzed method.

As Fig. 3.2 (a) shows, the SiO_2 layer is partially etched to obtain nanoscale holes and expose the fresh Si in the nanoscale holes. The tickness of SiO_2 layer is usualy in the order of 10 nm, and electronbeam lithography and wet etching is widely used to achieve this ordered hole array. Ga is deposited on the substrate and forms Ga droplets in the holes as shown in Fig. 3.2 (b). Due to the high migration of Ga on SiO_2 layer, Ga atoms moves on the SiO_2 layer till fall into the nanoscale holes, thus the Ga atoms start to form Ga droplets and grow larger. The temperature of substrate and the deposition time is optimized to controlled the size of Ga droplets. By opening Ga and As flux, GaAs NWs are achieved in the nanoscale holes as shown in Fig. 3.2 (c). GaAs NWs are positioned at the nanoscale holes, so this method is called "selective area growth (SAG)". GaAs NWs In the growth of GaAs NWs, low $F_{V/III}$ is usually used which is called Ga-rich condition. Ga

droplets always exist during the entire growth process and play the role of catalyst under this Ga-rich condition.

3.3 Two-step growth of GaAs NWs via self-catalyzed MBE

The NWs obtained by the above method are distributed regularly and have uniform size, but the biggest difficulty is to prepare nanoscale holes. The size of nanoscale holes is generally in the range of $60 - 120$ nm, which is much smaller than the feature size of optical lithography using mercury lamp. Therefore, optical lithography has no way to obtain nanoscale holes of this size, and it needs to be realized by EBL or nano-printing, which is cumbersome process. Thus, we used a two-step growth (TSG) method of GaAs NWs. In this TSG method, the Ga-droplets were grown randomly on the substrate. For studying the properties of GaAs NWs, the random distribution is not a serious problem, at the same time, the SAG method proposed in Sec. 3.2 is usefull for understanding the TSG method in this section.

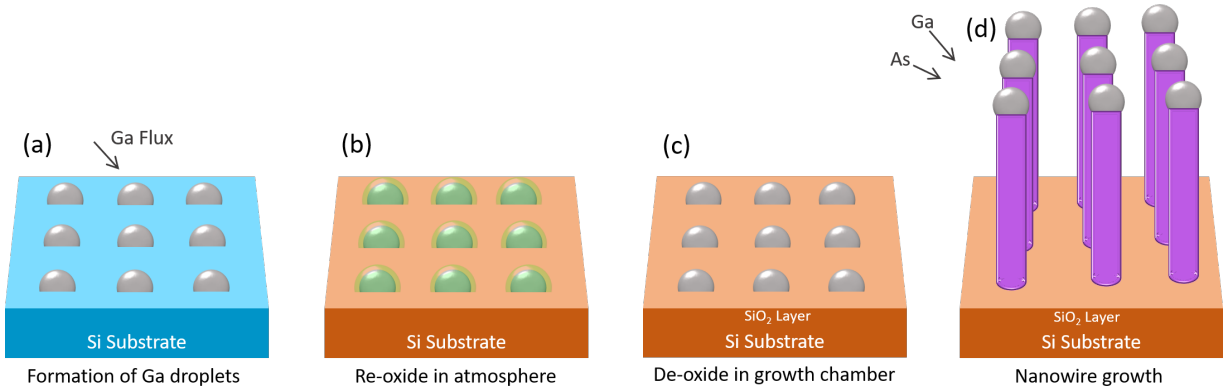

Figure 3.3: Schematic diagram illustrating the 2-step method for the growth of GaAs NWs via self-catalyzed method.

For the first step, Ga droplets are deposited directly on fresh Si substrate, as shown in Fig. 3.3 (a). Then the sample was taken out from the growth chamber into atomosphere and heated at 180 °C for 3 minutes. Then both the surface of Ga droplets and Si substrate was oxided as shown in Fig. 3.3 (b). Then for the second step, the sample was sent into the growth chamber again (so called "two-step method") for de-oxidation in UHV at temperature about 600 °C. After the deoxidation, the GaO_x layer around Ga droplets was removed as shown in Fig. 3.3 (c) but the SiO_2 layer on Si surface remained because the temperature is not high enough to decompose SiO_2. As a result, Ga droples forms on Si surface and surounded with SiO_2 layer similar to Fig. 3.2 (b). Thus, the growth of GaAs NWs starts as shown in Fig. 3.3 (d). The GaAs NWs grown in this two-step method are similar to those grown in the method of SAG, with the only difference of random distribution.

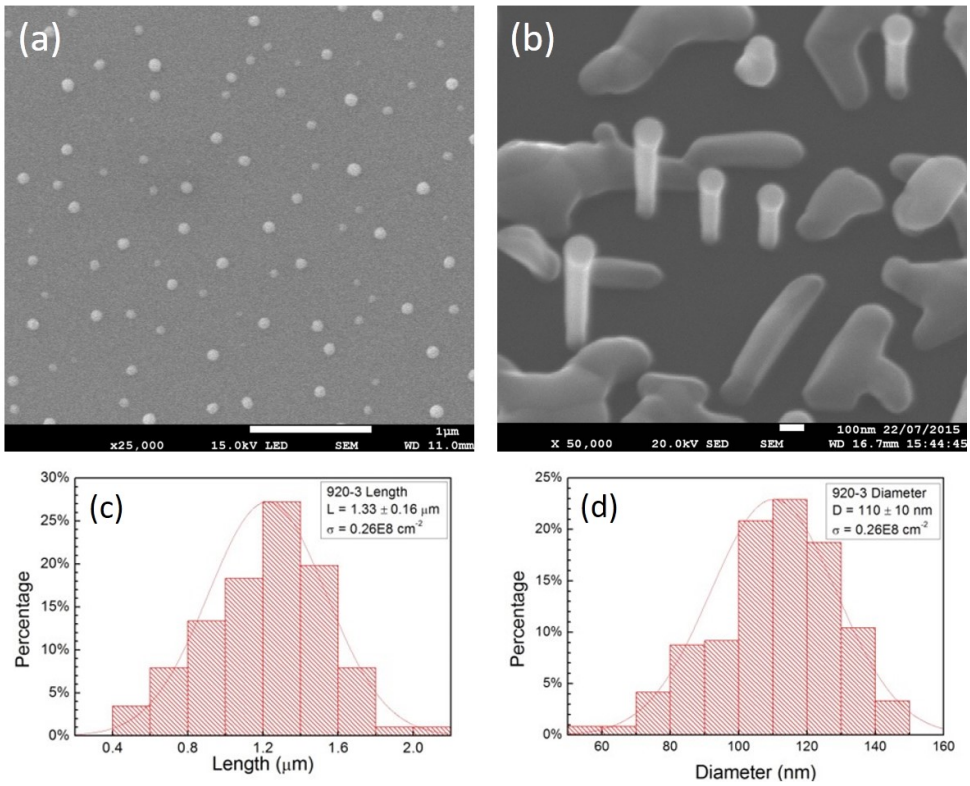

Figure 3.4: SEM images of (a) Ga droplets after the first step and (b) GaAs nanowires after the second step grown in TSG method.

6 MLs of Ga was deposited onto fresh Si surface, and then the sample was heated in UHV at 500 °C. After the re-oxidatation in air at 180 °C for 3 minutes SEM images have been taken for the sample. Fig. 3.4 (a) shows the Ga droplets distributing randomly on the substrate. The average diameter is about 74 nm, and the density is about 6.9×10^8 cm^{-2}. In the second step, the temperature of substrate was set between $560 - 600$ °C, the nominal Ga growth rate is around $0.1 - 0.3$ML/s, and the $F_{\mathrm{V/III}}$ is set about 10. After the second step, GaAs NWs have successfully grown vertically on Si substrate as Fig. 3.4 (b) shows. The average length is 1.33 ± 0.16 µm, and the diameter is 110 ± 10nm as shwon in Fig. 3.4 (c) & (d). Comparing the SEM images in Fig. 3.4 (a) & (b), not all the droplets promotes successfully the growth of NWs. The possible reason is the time for re-oxidation is not enough, so SiO_2 layer is not thick enough to prevent the growth of GaAs bumps.

3.4 Droplet assisted growth of InAs NWs via MBE

The growth of InAs NWs are in different mode rather than the VLS mode of GaAs NWs. Park and Coworkers have demonstrated that 10 nm sized indium nanoparticles can initiate growth of InAs NWs on SiO_2 with a growth mechanism which is different from the conventional VLS mechanism observed in most of the epitaxial growth of NWs [52]. InAs NWs can be achieved without the help of droplets as called VS mode, in which the gaseous precursors arrive on the top of NWs and crystallize into solid directly. But it can also be grown by droplet assisted method. Before our growth of InAs NWs, the natural oxide layer on Si(111) was removed in BOE solution and the substrate was dried after being rinsed in DI water. The substrate was mounted onto holder using moderate melted indium as solder. This operation was proceed in the atmosphere with the holder heated at appropriate temperature ($150 - 250$ °C) and for proper period of time ($1 - 2$ minutes),

we believe discontinuous oxide layer reformed on the surface, resulting in a large amount of randomly distributed pinholes. These pinholes would help indium form properly sited In-droplets during the seeding process under pre-optimized conditions, hence prompt the formation of growth of the NWs.

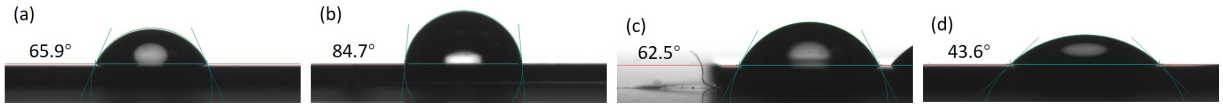

Figure 3.5: Images of contact angles for water drops on different type of Si substrates: (a) Si substrate without treatment, (b) Si substrate treated in HF for 30 seconds, (c) Si substrate treated in HF for 30 seconds and then in H_2O_2 for 40 seconds, and (d) Si substrate treated in HF for 30 seconds and then in H_2O_2 for 60 seconds.

Fig. 3.5 shows the contact angles for water drops on different type of Si substrates. The silicon wafer without any treatment has a contact angle of approximately 66 ° as shown in Fig. 3.5 (a). After HF treatment for 30 seconds, the surface SiO_2 was removed, revealing fresh Si and modified with F-ion, the surface became hydrophobic and the contact angle increases to about 85/,° as shown in as shown in Fig. 3.5 (b). Fresh Si(111) is quite stable in dry air at room temperature, and it often takes many days to reform the native oxide layer. H_2O_2 is used to simulate the oxidation of Si by oxygen. After 40 seconds of treatment with H_2O_2 , the contact angle in Fig. 3.5 (c) returned to 63 °, similar to the contact angle of the untreated wafer. The longer oxidation time will result in a thicker oxide layer, the surface becomes more hydrophilic, and the contact angle is further reduced to 44 ° as shown in Fig. 3.5 (d).

In order to evaluate and optimize the growth of In droplets, a series of In droplets samples were grown at various temperatures of $145 - 310$ °C using In flux in the range of $2.2 - 6.0 \times 10^{-7}$ mBar for a nominal thickness of 3 MLs. The growth of the InAs NWs was initiated by the simultaneous introduction of As and In species at growth temperature ranging from $440 - 500$ °C. The growth was terminated by closing both In and As shutters simultaneously. It is found that the geometry of the droplets is sensitive to both growth

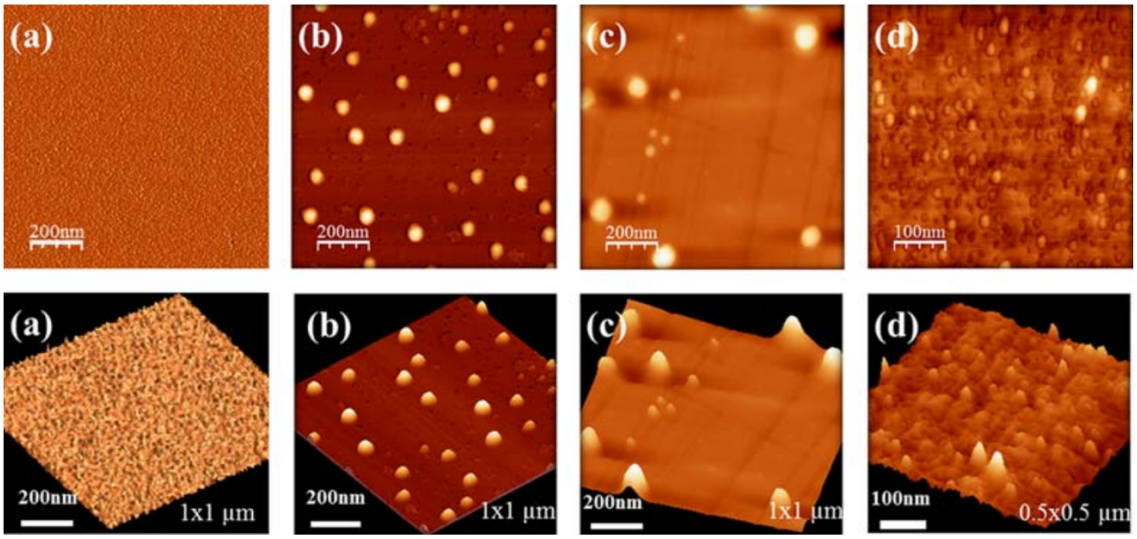

Figure 3.6: AFM images showing the top-view (top panel)and 3D view (bottom panel) of indiumdroplets deposited on bare Si(111) at various temperatures and In fluxes: (a) 145 °C, 2.2×10^{-7} mBar; (b) 220 °C, 2.2×10^{-7} mBar; (c) 310 °C, 2.2×10^{-7} mBar; (d) 220 °C, 6.0×10^{-7} mBar.

temperature and In deposition rate. We found that a low deposition temperature (145 °C) led to small and highly dense droplets as shown in Fig. 3.6 (a). A increased deposition temperature (220 °C) led to droplets with medium size (55 nm), height (20 nm) and density (2×10^{-9} nm) as shown in Fig. 3.6 (b). A further increase in growth temperature (310 °C) resulted in droplets with increased diameter, height but reduced density as shown in Fig. 3.6 (c). This behaviour is connected to the increased diffusion length of In adatoms which results in larger and less dense droplets. An increase in indium flux led to the formation of nearly coalescent droplets with an average diameter, height and density as shown in Fig. 3.6 (d), attributed to the reduced adatom diffusion time which leads to dense and small droplets.

During the growth of InAs NWs, the temperature of substrate was set between $440 - 500$ °C, the nominal In growth rate is around 0.1ML/s, and the $F_{\mathrm{V/III}}$ is in the range of $20 - 120$. Fig. 3.7 shows the SEM images of the InAs NWs grown for 25, 40, 60 and 144 min with the In droplets shown in Fig. 3.6 (b). From Fig. 3.7 (a)-(d), it can be seen

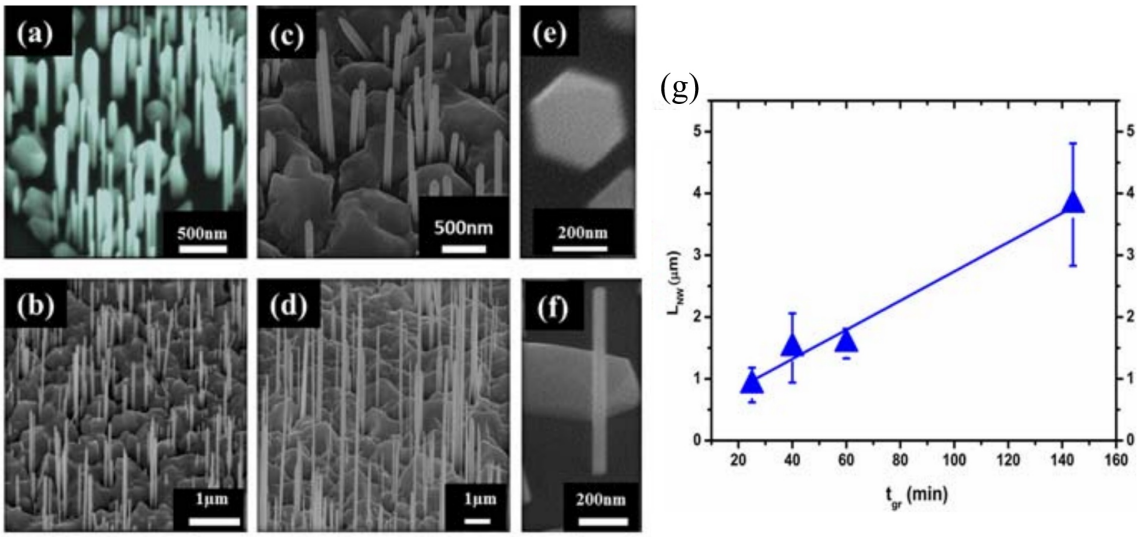

Figure 3.7: Tilted SEM images of vertically-aligned InAs NWs grown for (a) 25 min, (b) 40 min, (c) 60 min, and (d) 144 min. (e) and (f) are the cross-section and high-magnification images of NWs grown for 40 min. The evolution of the NW length (L_{NW}) as a function of growth time (h) are also shown. Tilt angles for (a) and (b) are 30 °, while for (c) and (d) they are 40 ° and 60 °, respectively. The given error bars denote the standard deviation.

that vertically aligned and non-tapered InAs NWs without kinking across the entire wire length were obtained. The NWs have well-facetted hexagonal cross-sections as shown in Fig. 3.7 (e), and it is clearly shown that the In droplets is absent from the top of the NW as a certain result of VS growth mode. The uniform diameter across the NWs length can also be observed in Fig. 3.7 (f). In Fig. 3.7 (g) the evolution of L_{NW} as a function of growth time is depicted. The observed linear increase of L_{NW} with t_{gr} indicates a constant growth rate up to 3.8µm/h. Although the axial growth rate of NWs is basically determined by the III-element flux [53] and the nominal growth rate of InAs in our growths was low, we still observed a high axial growth rate. We attribute this high axial growth rate to the large diffusivity of In adatoms on the Si surface [54], low number density of the NWs and their narrow diameter.

Chapter 4

InAs nanowire based quantum hybrid structures

InAs NWs have attracted great interest during the past decades for advanced optical and opto-electronic device applications, such as LEDs, Laser diodes, detectors, solar cells, and transistors. The device performance depends on the properties of NWs, such as morphology, crystal structures, bandgap structures & alignment / confinements in NW-related heterostructures. We recognize that the introduction of the Ga and Sb elements results in distinct changes in morphology, crystal structure, electrical properties, and optical properties. In this chapter we will introduce the following two parts: the first is the growth of InAs NWs, and the modification of Sb on InAs NWs in terms of the morphology, structure, and bandgap. The second is core-shell heterostructures, *e.g.* InAs-InGaAs core-shell NWs and InAs-GaSb core-shell NWs.

4.1 Growth and basic characterization of InAs NWs

The InAs NWs were grown via a previously established droplet-assisted growth technique described in Chapter 3 on both n- and p-type Si(111) wafers. Before the growth, the natural oxide layer on Si(111) was removed in BOE solution and the substrate was dried after being rinsed in DI water. The substrate was mounted onto holder using moderate melted indium as solder. This operation was proceed in the atmosphere with the

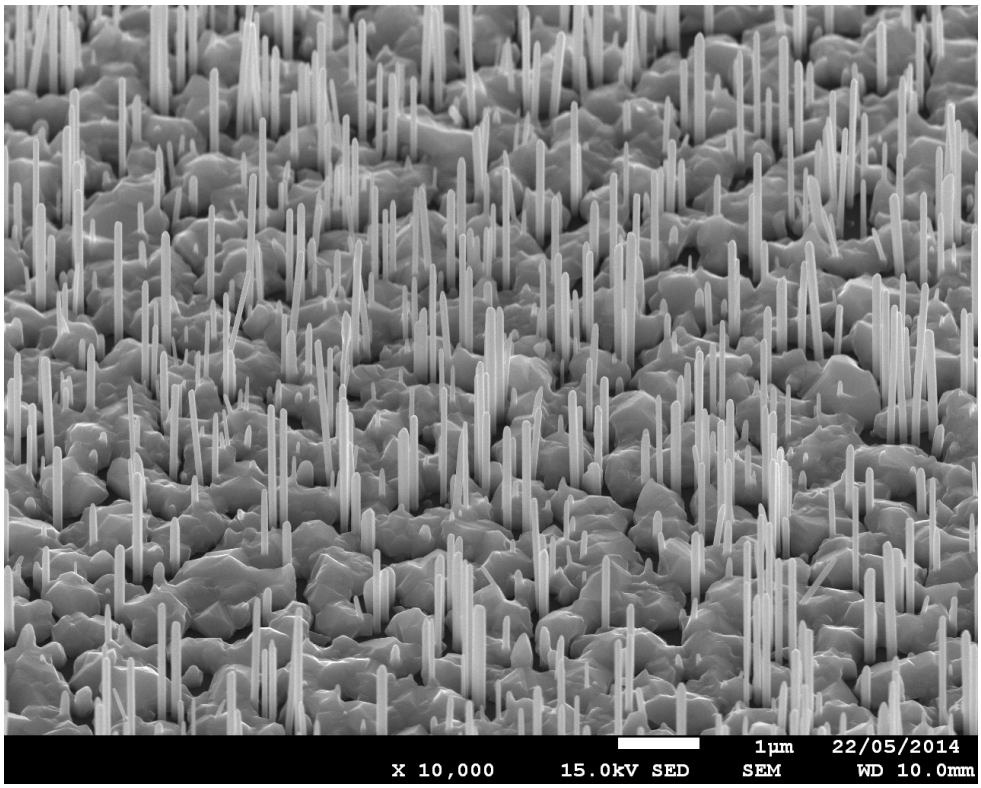

Figure 4.1: 45 °-tilted SEM images of sample A737 InAs NWs grown on N-type Si.

holder heated at appropriate temperature ($150 - 250\,^{\circ}$C) and for proper period of time ($1 - 2$ minutes), we believe discontinuous oxide layer reformed on the surface, resulting in a large amount of randomly distributed pinholes. These pinholes would help indium form properly sited In-droplets during the seeding process under pre-optimized conditions, hence promote the formation of growth of the NWs. With the favorable nucleation of In-droplets, the NWs were grown at pre-optimized conditions, *e.g.* growth temperature of 420−460 °C, and As-rich condition with As4 BEP of around $6 - 9 \times 10^{-6}$ mBar. The growth was terminated by closing both the shutters and valves of In & As simultaneously, and the temperature of substrate decreased immediately.

Fig. 4.1 is the SEM image of InAs NWs sample (A737) taken from the angle of 45 °. This sample was grown at the substrate temperature of 430 °C. Despite of the very few of NWs grown on InAs bumps, most of the InAs NWs are vertically and directly standing

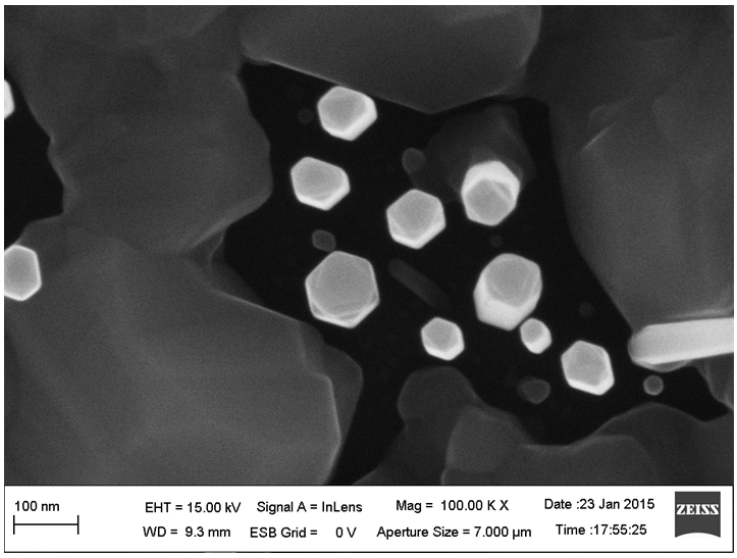

Figure 4.2: Top view SEM image of sample A821 InAs NWs.

on Si substrate. For InAs NWs grown directly on Si wafers, they all grow vertically and usually have longer length. For InAs NWs grown on InAs bumps, most of them are also perpendicular to the Si surface, with only a small amount are tilted. The reason for their tilting is that, when they start growing from InAs bumps, a different direction from the other NWs was selected depending on the specific site. And once they start to grow longer, the direction of growth will remain the same as the beginning. It is usually difficult to avoid bumps growth adjoint with NWs growth, and it is out of the topic of this thesis, hence we do not focus on how to avoid the bumps, instead we focus on the NWs growth.

These NWs on bumps are usually shorter than NWs grown directly on silicon for two reasons: first, NWs on Si substrate usually grow immediately at the beginning of the growth, in other words they have much longer time for growth. The NWs on the bumps are non-equilibrium-excited growth starting at the different time during the growth of bumps, indicating that their growth time is short and inconsistent, which explains why the lengths of these NWs vary greatly. Second, for these nanowires on bumps and those nanowires standing on silicon, the environment around the foot is quite different. As we know in chapter 3, the nanowires siting on the silicon wafer are usually standing in pin

holes among the secondary-formed silicon oxide film. The feet of NWs are surrounded by silicon dioxide, on which the indium atoms have a high mobility. In this environment, the indium atoms on the silicon wafer around the nanowires are easily to migrate to the NWs, to participate in the growth of nanowires. The bumps under the foot of NWs is the same substance InAs. these polycrystalline bumps keep adsorbing indium atoms falling on the surface and keep growing, which hinders the migration of indium atoms to nearby nanowires, and slows the growth of nanowires.

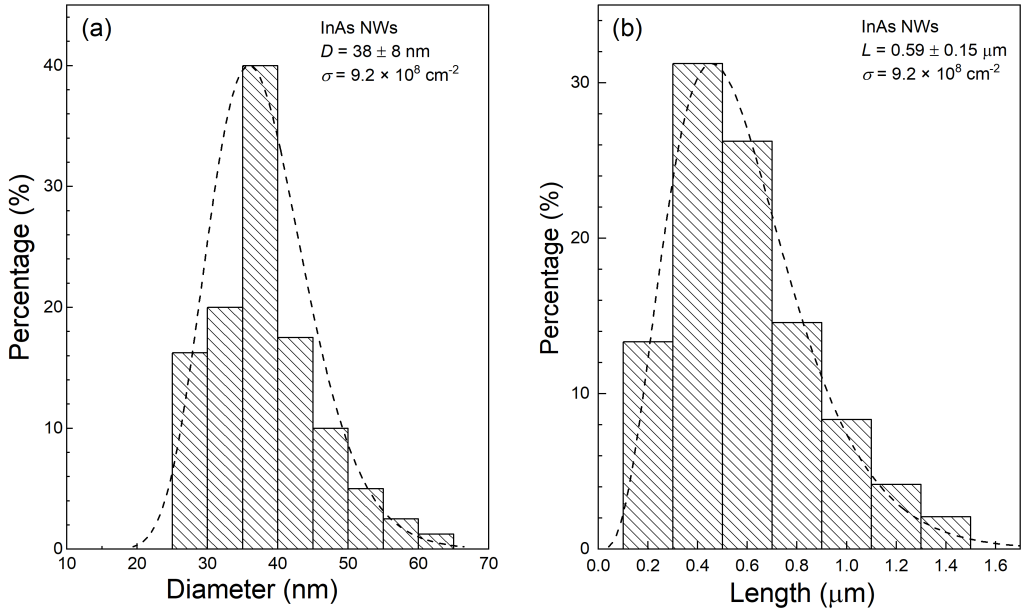

Figure 4.3: Morphology statistics for InAs NWs.

Morphology statistics have been done based on SEM images containing about 200 NWs, showing the NWs has quite uniform diameter but nonuniform length. The distribution of diameter of NWs was done in steps of 5 nm, and generally varies from 20 nm to 70 nm as shown in graph 4.3 (a). The distribution is quite concentrated but a bit asymmetric with a tail in the direction to large diameter. The average value is $38 \pm 8\ nm$ whose relative deviation is about 21% and the NWs with diameter of $35 - 40$ nm have the highest proportion of 40%. The diameter distribution mainly concentrates in the range of

$25 - 50$ nm, in which more than 80% of the NWs fall.

Meanwhile the length of the NWs is not as uniform as diameter. The distribution is more asymmetric than that of diameter with a tail in the direction to large diameter as shown in graph 4.3 (b). Their length varies from 0.1 µm to 1.5 µm with an average value of 0.59 ± 0.15 µm, whose relative deviation is larger than 25%. The NWs with length of $0.3 - 0.5$ µm and $0.5 - 0.7$ µm both have high proportion lager than 25%. The length distribution mainly concentrates in the range of $0.1 - 0.9$ µm, in which more than 80% of the NWs fall. The NWs has quasi-hexagonal cross sections as Fig. 4.2 shows. The NWs among bumps are vertically standing on Si substrate. Their diameter differs in a wide range from 20 nm to 90 nm. According to the calculation in Sec. 1.8.2, the energy increasing due to quantum confinement effect is approximately $0 - 22$ meV. Fig. 4.4 is the

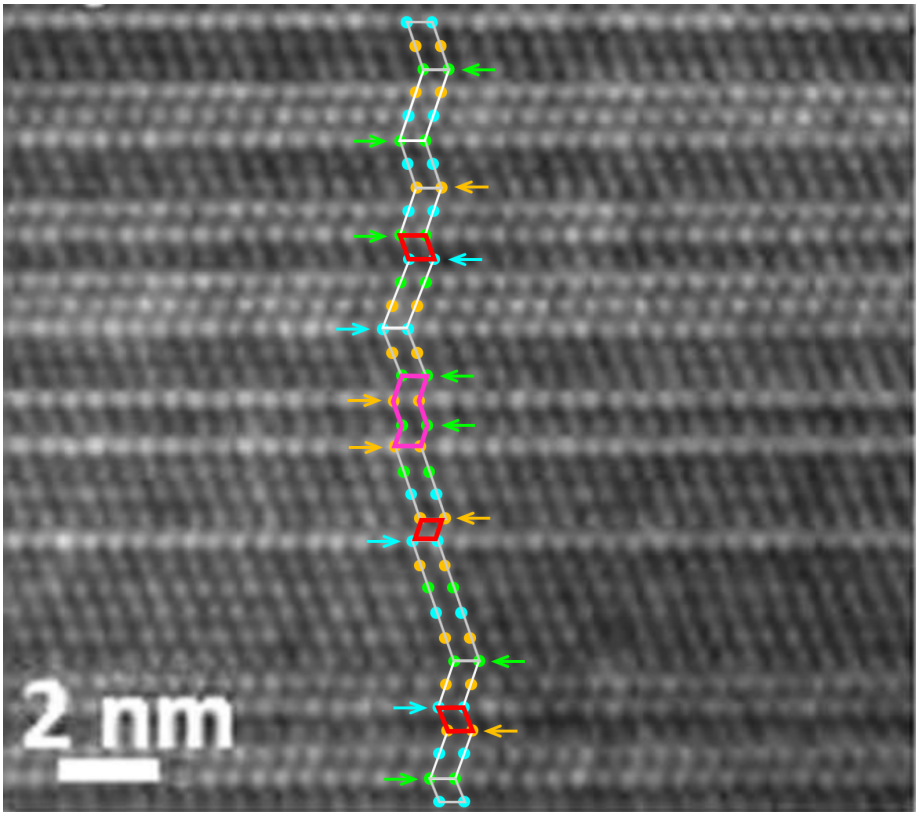

Figure 4.4: HRTEM image of sample A737 InAs NWs.

HRTEM image of sample A737 InAs NWs. It has a mixture of the ZB (quadrangle in white

lines) and WZ (polygon in magenta) phases, while ZB dominates associated with SFs and twinning planes. Type-II band alignment will form inside the NWs, which contributes to the luminenscence. As a result, this mixing phases will largely affect the optical properties of nanowires. Considering both ZB and WZ segments are very small in this TEM image, it is expected that the quantum confinement effect in this sample would be significant, *i.e.*, the emission from type-II alignment in this sample may be larger than normal type-II energy band alignment. The optical property of InAs NWs strongly depends on the

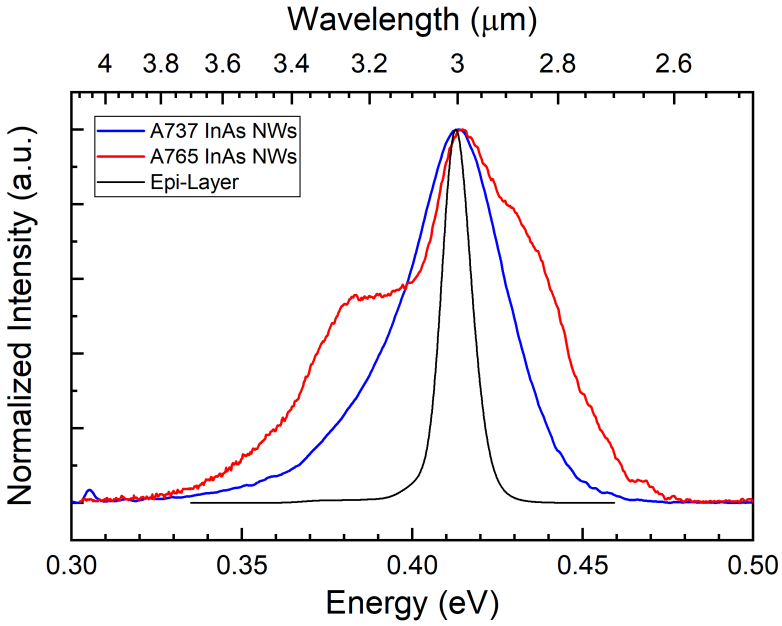

Figure 4.5: Photoluminescence of samples of InAs NWs and InAs epi-layer at low temperature.

crystal structures. Fig. 4.5 shows the photoluminescence spectra of three samples at 4.2 K: two samples of InAs NWs and one sample of InAs epi-layer. The optically high quality NWs shall give a narrow & symetric PL spectrum at low temperature. While different issues in NWs make the peak broad: radial confinement, non-uniformity of diameters, polycrystallinity, and type-II alignment between ZB and WZ phases. The epi-layer has narrowest peak at around 0.415 eV, in agreement with the value of ZB-InAs bulk materials. The main peaks of A765 and A737 also locate at around this value. The broader peaks

with shoulders imply the peculiarity and complexity of the NWs. Between A765 and A737, the former is more complicated. To reveal more information of optical property and crystal structures of sample A765 InAs NWs, power-dependent and temperature-dependent PL measurement has been done.

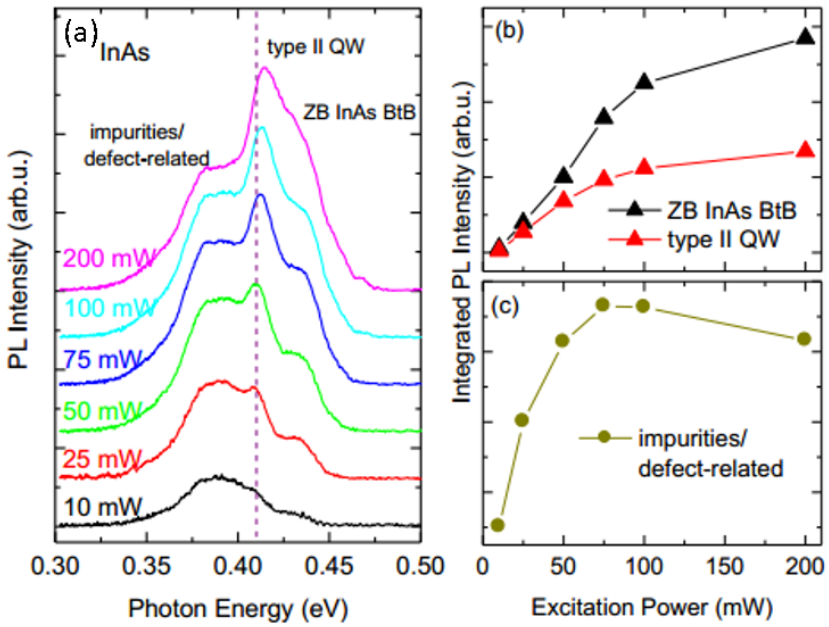

Figure 4.6: Power-dependent photoluminescence of sample A765 InAs NWs.

Fig. 4.6 (a) show the photoluminescence of sample A765 InAs NWs under various excitation power at 8 K. The peaks are not symetric and could be decomposed into 3 peaks. During the power-dependent measurement, the relative intensity of the middle peak increases the fastest. It locates at about 0.41 eV under low excitation power, while shifts to around 0.42 eV under high illumination, exhibiting a blueshift with increasing excitation power. Due to both the band filling effect associated with increase of excitation power and the band bending induced by the carriers accumulated at the interfaces of ZB-WZ phases, this blue-shift often occurs in type-II band alignment quantum well structures, suggestting the existence of type-II band alignment. Although the position of this middle peak is close to the energy of ZB InAs bulk materials, is is suggested emission from

type-II anlignment between ZB and WZ phases. It's worth mentioning that no shift is observed during the power sweeping measurement for the other two peaks. The left peak of lower energy dominates under low illumination but degenerates into a shoulder under high excitation power, which behaves like defects-/impurity-related emission. The right peak of higher energy increases fastest among the three peaks. It is likely that it could be from the BtB emission from ZB phases of InAs.

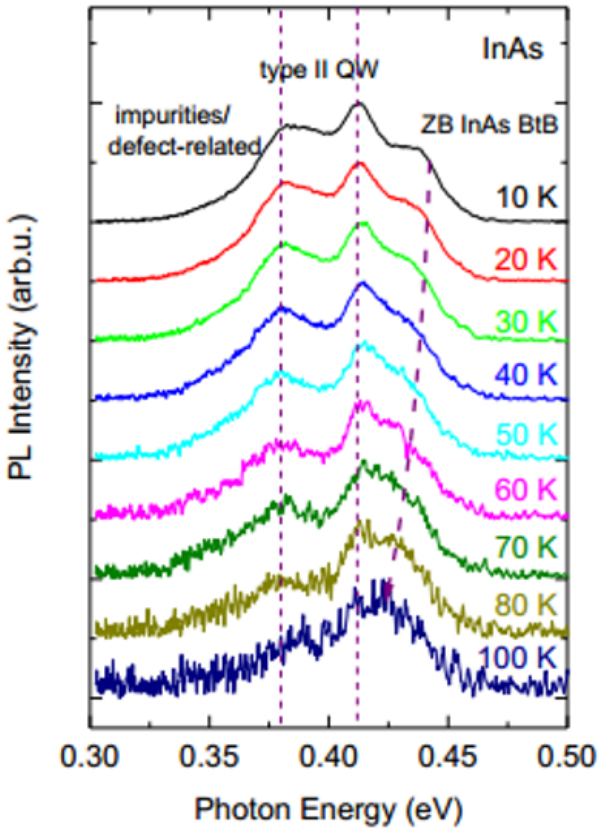

Figure 4.7: Temperature-dependent photoluminescence spectra of sample A765 InAs NWs.

To further confirm the assignments of all the three peaks, detailed analysis has been done. Fig. 4.6 (b) and (c) emerge the integrated intensity of all the three peaks. It is clearly shown in Fig. 4.6 (b) that, integrated intensity of middle peak (red line) and right peak (black line) has linear dependence against excitation power under low illumination, while under high illumination this linear relationship does not hold. The two-stage luminescence

accords with type-II QW and BtB emissions. However, as Fig. 4.6 (c) shows, the left peak at around 0.38 eV saturates and decreases under high excitation power, indicating impurity/defect-caused recombination processes would be involved.

Fig. 4.7 shows the luminescence spectra of sample A765 InAs NWs at different temperatures under a fixed excitation power of 200 mW. The left peak decreases rapidly as temperature increases, while the middle peak and the right peak decrease slowly. Besides, the left peak and the middle do not present obvious shift, which agrees with impurity/defect-related emission and type-II emission, respectively. On the contrary, the right peak reflects representative red-shift with increasing temperature, which can be ascribed to bandgap shrinkage, and it becomes the dominate among the three peaks at 100 K. From the above analysis based on power-sweeping and temperature-sweeping PL measurement, the assignments of all the 3 peaks have been fully confirmed.

4.2 The effects of substrate doping-type on the optical properties of InAs NWs

As mentioned in Sec. 1.4, the valence-band edge of the ZB InAs is 46 meV lower than that of the WZ InAs, while the conduction-band edge of the WZ InAs is 86 meV higher than that of the ZB InAs. As a result, typical PL peaks from type-II QWs has been observed in Sec. 4.1 as the WZ and ZB phases form type-II alignment. For studying optical properties and bandedge structure of InAs NWs, PL spectroscopy is an accessible and efficient routine. However, like the recent PL analyses focused on bandgap evolution and carrier recombination in InAs NWs conducted by other researchers [55], the achievable temperature for that PL measurements was limited below 120 K due to the primitive methods of measurement and the quality of InAs NWs. To reveal more mechanisms

of InAs NWs such as non-radiative recombination and carrier transfer, more advanced technique and InAs NWs samples with high quality would be used. From the above idea, modulated mid-infrared PL method based on a step-scan Fourier transform infrared (FTIR) spectrometer will be used for the high-quality InAs NWs grown on n- and p-type Si substrates in a wide temperature range of 8−290 K in this section.

As the InAs NWs are natually n-type, when InAs NWs are grown on p-type Si substrate, p-n heterojunctions are possiblly configured between the NWs and the substrate. Thsi can be potential used for optoelectronic device applications, such as photovoltaic photodetectors. The built-in electric field along the axial direction in the NWs or between the NWs and the substrate would play an important role in the recombination of photo-induced carriers.

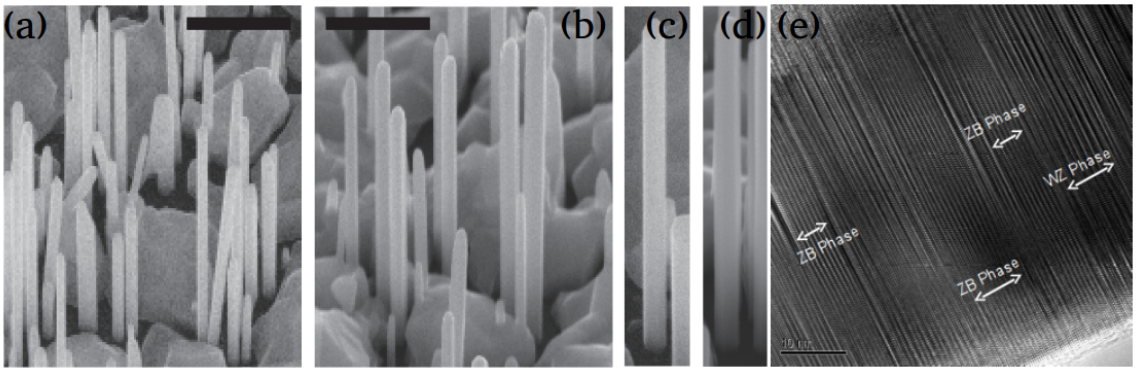

Figure 4.8: SEM images of sample-N (a) and sample-P (b) at a scale bar of 500 nm. Single NW manifests upright standing as in (c) and (d) for sample-N and sample-P. (e) TEM image of InAs NWs. The TEM scale bar is 10 nm.

To reveal the origins of the PL transitions, two high-quality InAs NWs samples (A737) were grown directly on n- and p-type bare Si substrates at the same time, which means their growth conditions are totally the same. In this section they are labeled as sample-N and sample-P for convenience and distinction. The local SEM images of the sample-N and sample-P are depicted in Fig. 4.8 (a) and (b), respectively. The average diameter and length of the NWs are about 80 nm and 1 µm, respectively. According to Sec. 1.8.2, the

radial quantum effect is negligible in this sample and the optical properties of the NWs are expected to be bulk-like rather than quantum-like. Most NWs are free standing directily on the Si substrate as represented in Fig. 4.8 (c) and (d). A representative TEM image of InAs NWs is shown in Fig. 4.8 (e), which exhibits mixture of ZB/WZ crystal structure along the growth direction.

To get insights into the mechanisms, temperature-dependent PL and power-dependent PL measurements were conducted in a step-scan FTIR spectrometer, and mechanical chopper was also used to improve the signal-to-noise ratio. The samples were mounted on a heat platform in a low-temperature environment cooled by liquid-helium, as a result, the temperature of the samples could be precisely controlled in the range of $8 - 290$ K by the heat platform for temperature-dependent measurement and the temperature of samples was fixed at 8 K during the power-dependent measurements. A 639-nm continuous-wave laser and proper filters were used for adjusting the power in the range of $10 - 320$ mW for power-dependent measurements, while the illuminating power was set at 100 mW for temperature-dependent measurements. The diameter of laser spot is about 200 µm, which is much larger than the vision field of SEM in Fig. 4.8 (a) and (b), so more than ten thousands of NWs would be involved in the laser spot with an area of $4000\ \mu m^{-2}$ during the PL measurements. Taken in this sense, the PL spectra should be regarded as a statistical integration of the thousands of NWs with unintentionally random surface condition and morphology. Bumps and residual clusters could be seen in Fig. 4.8, but no PL signal could be detected once the NWs were mechanically removed. So the PL data which were analyzed in this section are solely related to the InAs NWs.

Fig. 4.9 represents the infrared PL spectra of the sample-N and sample-P at temperatures range of $8 - 290$ K. All the curves were normalized at appropriate magnification for comparison. For sample-N and sample-P, the PL curves at $8 - 290$ K have several common features: Firstly, at 8K only one asymmetric PL peak appears at about 0.415 eV

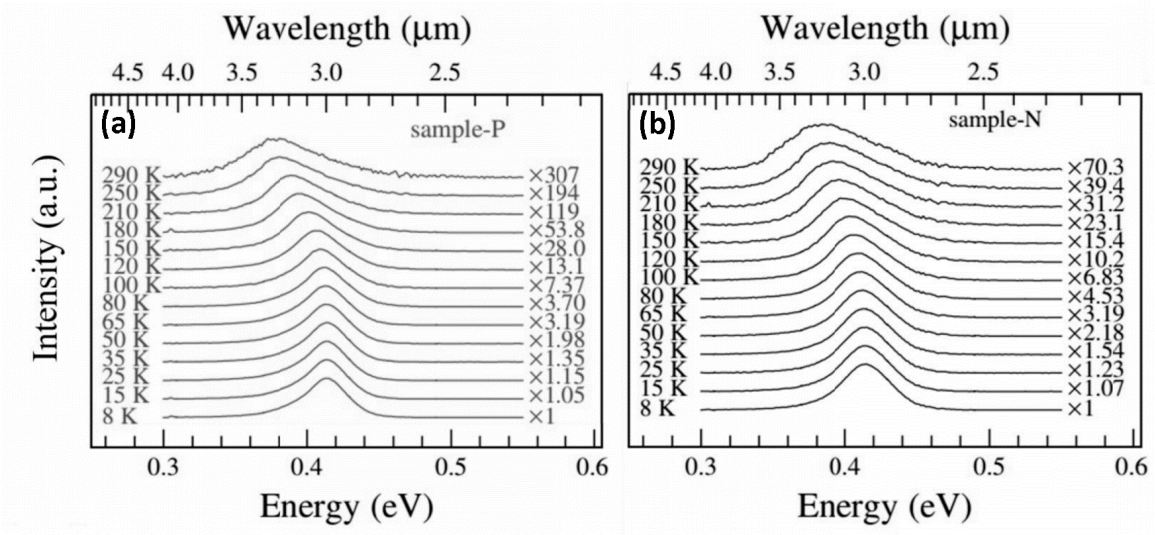

Figure 4.9: Temperature-dependent PL spectra of sample-N (a) and sample-P (b), magnified by particular factors for similar peak heights.

for both samples. This means that the bandgap transition of WZ InAs is frozen because it should be around 0.45 eV. As the temperature increases, the PL peak is monotonously red-shifted, which is consistent with the negative temperature coefficient of the bandgap of bulk InAs. The same as the redshift is that the PL intensity gets weakened, and moreover at 290 K for sample-N and sample-P, it reduces to around 1/70 and 1/300 of the intensity at 8 K, respectively, as evidenced by the magnification.

For the quantitative analysis of temperature effects, each PL spectrum is linearly fitted by a typical Lorentz-Gaussian composite function, thereby quantitatively deriving the energy, linearity and intensity of the PL features. Representative fit is shown in in Fig. 4.10 (a) for the two temperatures of 8 K and 290 K. At 8K, a single Lorentz-Gaussian composite function is insufficient, but requires a dominate feature (DF) of 0.415 eV and an additional low energy feature (LEF) of approximately 0.401 eV to reproduce the PL line shape well. At 290 K, the fit shows a DF of about 0.380 eV and a high energy feature (HEF) of about 0.425 eV. The HEF is shown in logarithmic scale by plotting the PL spectrum in Fig. 4.10 (b), which is indeed beyond the high-energy exponential tail

introduced by the Fermi-edge distribution of carriers. The survival of DF and HEF at 290K indicates that these two features are BtB transitions, since the temperature is so high that the impurity-related transitions in InAs are all suppressed. The energy evolution

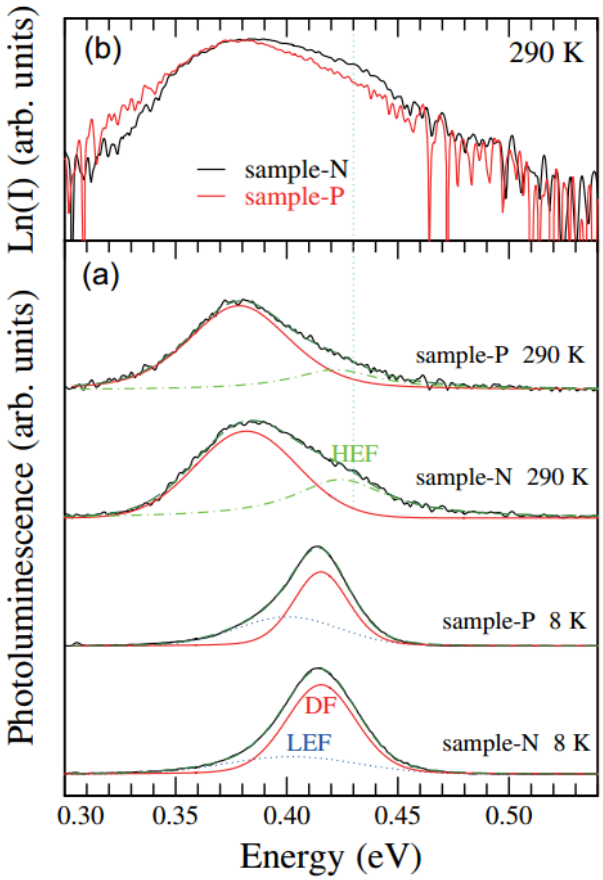

Figure 4.10: Curve fittings of PL spectra for sample-N and sample-P at 8 and 290 K. (b)PL spectra of the two samples at 290 K plotted in logarithmic scale.

with temperature is depicted in Fig. 4.11 (a) for each PL feature of sample-N and sample-P. Although the DF remains within the entire temperature range and monotonically red-shifts with temperature, its energy-temperature relationship can well explained as the bandgap shrink behaviour of semiconductor as shown by the red line in Fig. 4.11 (a):

$$E(T) = E_0 - S\langle\Theta\rangle \left[\coth\left(\frac{\langle\Theta\rangle}{2T}\right) - 1\right] \tag{4.1}$$

where E_0 is the bandgap energy at 0 K, S is the coupling coefficient, and $\langle\Theta\rangle$ is the average phonon temperature. For sample-N and sample-P, the inferred value of E_0, S , and $\langle\Theta\rangle$ are 0.414 and 0.416 eV, 0.08 and 0.10 meV/K, and 178 and 220 K, respectively. It is very clear that the DF energy varies linearly with temperatures in the range of $65 - 290$ K, and the slopes are -0.135 meV/K and -0.179 meV/K, respectively for sample-N and sample-P. At the same time, the peak positions of LEF are not sensitive to temperature at all for both sample-N and sample-P. Since LEF appears on the low energy side and is quenched at temperatures above 100K, it is likely to correspond to impurity-related transitions like donors. For HEF, the slope in the plot of the energy versus temperature is about -0.056 meV/K and -0.084 meV/K, respectively for sample-N and sample-P. The rapid redshift of DF and HEF reflects the high sensitivity to temperature, indicating the nature of the transition relevant to conduction band. In addition, when we compare the the redshift with temperature of the DF and HEF, the difference between them may suggests that DF and HEF correspond to different conduction bands.

The PL intensities of the two samples are very close to each other at 8K, as shown in Fig. 4.9, while they differ greatly at high temperature. However, they are not considered as a criterion for the optical quality of the sample because the intensity may be affected by the positioning of the samples within the laser spot and/or the density of local NWs. In contrast, the integral intensity of PL with temperature evolution is more reliable and is able to reflect directly the state of non-radiative recombination and carrier transition.

For the PL features of the two samples, the integrated intensities against temperature are plotted in Fig. 4.11 (b). As the temperature increases, DF and LEF monotonically weaken, which can be explained by the quenching model involving multiple non-radiative processes:

$$I(T) = \frac{I_0}{1 + \sum C_i \exp(-E_i/k_{\mathrm{B}}T)} \tag{4.2}$$

Where C_i and E_i represent the non-radiation coefficient and the quenching activation

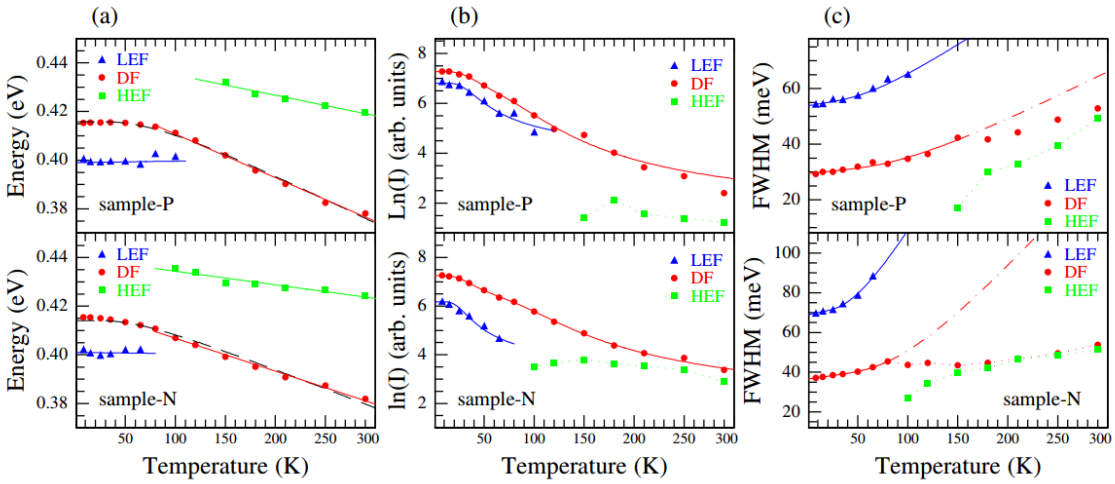

Figure 4.11: (a) Energy, (b) integral intensity, and (c) FWHM versus temperature for DF, LEF and HEF PL components of sample-N and sample-P.

energy of the i^{th} non-radiative channel, and I_0 is the derived integral intensity at 0 K. It is worth noting that although the LEF works well with a single non-radiative channel, the DF is well fitted only when the second channel is introduced. The fitting parameters are listed in Table 4.1. For either LEF or DF components, the quenching activation energy of the first channel is about 9 meV for sample-N and 11 meV for sample-P, respectively. This implies that this channel is associated with non-radiative dislocations and/or Auger recombinations.

The activation energy of the second quenching channel of DF is approximate 46 meV, which is very close to the energy deviation of 0.045 eV between HEF and DF at 290K. This indicates that the second channel is a thermal-induced carrier transfer from the DF to the HEF related energy level. This carrier transfer is supported by the HEF integrated intensity, which is first enhanced and then attenuated, exhibiting competition between injection of thermal-induced carriers and non-radiative recombination.

The thermal-induced carrier transition in sample-N and sample-P can be verified by the evolution of FWHM with temperature, as shown in Fig. 4.11 (c). In general, FWHM (Γ) widens with increasing temperature due to carrier-phonon scattering and can

be described with

$$\Gamma(T) = \Gamma_0 + \gamma T + \frac{2b}{\exp(\varepsilon_{LO}/k_{\mathrm{B}}T) - 1} \tag{4.3}$$

where ε_{LO} is the longitudinal optical (LO) phonon energy, k_{B} is the Boltzmann constant, and γ is the carrier-acoustic phonon interaction coefficient and b is carrier-LO phonon interaction coefficient, respectively.

This is actually the real case of the FWHM for LEF and DF at low temperatures, as shown by the solid line and dash-dots in Fig. 4.11 (c). The derived values of $\Gamma_0, \varepsilon_{LO}, \gamma$ and b are listed in Table 4.1. The ε_{LO} of LEF is much smaller than the LO phonon energy of InAs, which is 29 meV for both two samples. This may indicate that the LEF-related carriers locating in this region, *e.g.* around the impurities, have very different elastic coefficients and/or effective atomic mass compared to those of InAs NW. This is additional support to the conclusion that the LEF is impurity-related transition in the PL energy analysis described above. On the other hand, for both two samples, the ε_{LO} of DF at low temperature is very close to the LO phonon energy of InAs, which indicates that DF comes from BtB radiative recombination. It is easy to see in Fig. 4.11 that HEF occurs at temperatures beyond 100 K, the FWHM of DF is significantly different from the widening described with Equation 5.3, and the broadening of HEF can neither be described with Equation 5.3. This failure of the Equation 5.3 implies a deficiency of the two-level assumptions on which the equation is based, and the thermal-induced transfer of carriers between DF and HEF has to be considered.

To further understand the mechanism of transition, the excitation power-dependent PL spectrum was plotted for the two samples at 8K as shown in Fig. 4.12 (a). Referring to the analysis on temperature-dependent PL measurements shown in 4.11 (a), a similar curve fitting analysis is performed and the energy against excitation power is plotted in Fig. 4.12 (b) for both the LEF and DF PL components.

The DF blueshifts monotonously with excitation power for both samples, meanwhile

Table 4.1: $C_i, E_i, \Gamma_0, b, \varepsilon_{LO}$ and γ derived from the evolution of integral intensity and FWHM with temperature for the DF and LEF of sample-N and sample-P.

		Sample-N		Sample-P	
		LEF	DF	LEF	DF
I	C_1	16.6	5.8	17.1	9.3
	E_1 (meV)	8.9	8.5	11.5	11.0
	C_2	–	255	–	377
	E_2 (meV)	–	46.8	–	45.3
Γ	Γ_0 (meV)	69.0	36.6	53.8	29.4
	γ (meV/K)	0.10	0.07	0.06	0.04
	b	61.3	84.3	19.9	24.2
	ϵ_{LO} (meV)	13.6	27.6	18.4	27.8

the LEF first moves to higher energy quickly under low illumination but slows down significantly under higher illumination. According to our knowledge, this non-monotonic evolution is usually correlated to impurity-related transitions [56]. The blueshift of the DF is attributed to the band bending effect during type-II transition, which can be well described with the equation for the band bending effect considering the spatially separated carriers:

$$E(P) = E_0 + CP^{1/3} \tag{4.4}$$

where E_0 is the PL energy without band bending effect, P is the excitation power and C is a coefficient. The derived E_0 and C are 0.406 eV and 0.407 eV, and 1.98 meV/mW$^{1/3}$ and 1.74 meV/mW$^{1/3}$, for sample-N and sample-P respectively.

According to the mentioned experimental results including Fig. 4.12 and the coexistence of ZB/WZ phases in NWs as shown by the TEM image of Fig. 4.4 in this section, the mechanisms of the DF- and HEF-related PL transitions are illustrated by sketching a type-II band structure in Fig. 4.12 (c): DF is derived from the radiation recombination of photo-generated electrons in ZB phases and holes in the adjacent WZ phase, while HEF is

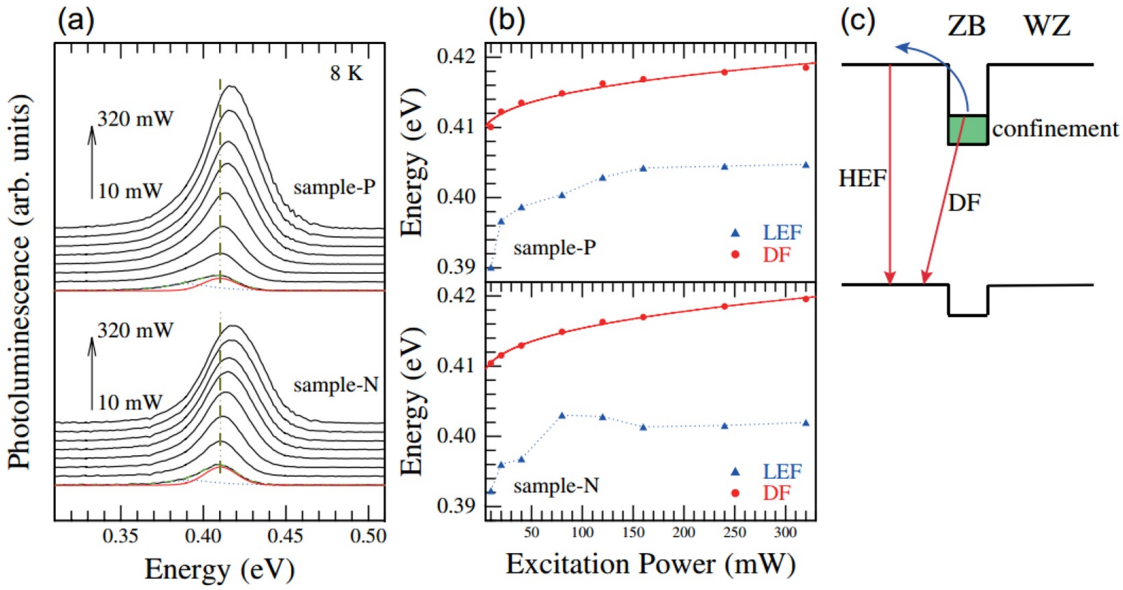

Figure 4.12: Excitation power-dependent PL spectra of sample-N and sample-P at 8 K. (b)Energy vs excitation power for DF and LEF PL components. (c) Schematic of the DF- and HEF- transitions along the NWs' axial direction, red arrows for radiative recombination and blue arrow for thermal-induced electron transition.

due to BtB transitions in the WZ phases. Since electrons are thermally stimulated from the conduction band of ZB phases to the conduction band of the adjacent WZ phases, HEF is activated at high temperature.

It is worth noting here that our experimental result is very consistent with the theoretical band structure of ZB/WZ InAs previously proposed by Murayama *et al*. Once the theoretical band offset is further considered as the conduction band and the valence band edge of WZ phase are 86 meV and 46 meV higher than that of ZB phase, respectively, the quantitative description can be derived from the type of experiment type-II model: (i) The confinement energy of electrons is about 44 meV, while the confinement of heavy hole is ignored due to the large effective mass; and (ii) The effective length of the ZB segment is approximately 6 nm, which is very close to the length represented in the TEM image of Fig. 4.4, which in turn indicates the rationality of the type-II band structure.

The bandgap of WZ phase is about 0.425 eV at 290 K, which is 68 meV higher than

0.357 eV, the value of ZB phase. The energy difference between WZ phase and ZB phase is slightly larger than the theoretical value of $40 - 64$ meV, which may be because the theoretical value is calculated by deriving from 0 K. As illustrated in Fig. 4.11 (a), the red shift of DF is significantly faster than the red shift of HEF as temperature increases. This should be considered as a result of the relaxation of the band bending effect. Due to the non-radiative recombination and the thermal stimulation to the conduction band of WZ phase, the photo-generated electrons in ZB phase are significantly reduced at higher temperature, thus the band bending effect is remarkablly reduced, and as a manifestation in PL performance, the energy of type-II transition decreases rapidly compared to the energy of BtB transition.

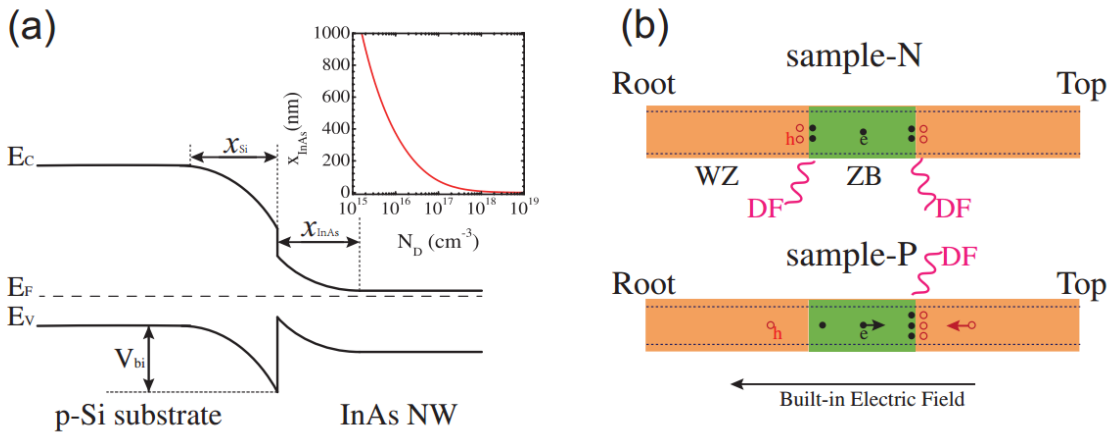

Figure 4.13: (a) Band alignment of sample-P, inset for the length of SCR vs electron concentration in InAs NWs. (b) Schematic of carrier migration in sample-N and sample-P, with built-in electric field marked in sample-P.

Based on the proven PL features, especially with the comparative temperature-dependent PL analysis for sample-N and sample-P, it is feasible and estimable to explore how the doping types of the substrates affect the behaviour of the photo-induced carriers. Since InAs NWs are essentially of n-type, the main difference between the two samples is that the NWs-substrate will form p-n heterojunctions in sample-P as shown in the Fig. 4.13 (a). Therefore, photo-induced carriers in the space charge region (SCR) are

affected by the built-in electric field. The SRC length x in the InAs-NW side is described as:

$$x = \sqrt{\frac{2\epsilon V}{e} \frac{N_D}{N_D \left(N_D + N_A\right)}} \tag{4.5}$$

where ϵ is the dielectric coefficient of InAs, N_D and N_A are the concentrations for electrons and holes in InAs NWs and Si substrate, respectively. V is the built-in potential and $V \geq 0.8\,\mathrm{V}$ for InAs NWs on p-type Si substrate.

The electron concentration in InAs NWs is non-uniform. The concentration of the inner NWs would be at the level of $10^{15} - 10^{16}$ cm^{-3}, which is close to that of bulk InAs, while the concentration at the NWs surface is about 10^{18} cm^{-3}. The inserted graph in Fig. 4.13 (a) represents the relationship between the estimated SCR length x (in the NW side) and the electron concentration, while the hole concentration in the p-type substrate is 5×10^{16} cm^{-3}. The x would be 1000—400 nm for $N_D = 10^{15} - 10^{16}$ cm^{-3}, whereas is negligible for $N_D = 10^{18}$ cm^{-3}, which suggests that the built-in electric field significantly affects the carriers at the NW surface.

In sample-N, the photo-induced carriers distribute around the ZB-on-WZ and WZ-on-ZB interfaces and produce the DF PL component with equal probability. In contrast, a built-in electric field forms in sample-P with the direction pointing from the top to the root of the NW. The photo-induced electrons in the ZB- and holes in the WZ-InAs migrate under the electric field and assemble around the WZ-on-ZB interface, leading to the DF be mainly produced therein as schematically shown in Fig. 4.13 (b). The temperature dependence of the DF can hence serve as a probe for the ZB-/WZ-InAs interfaces: while the DF of sampleN is due to the average of the ZB-on-WZ and WZ-on-ZB interfaces, that of sample-P is dominated by the WZ-on-ZB interface effects.

As shown in Table 4.1, the C_1 of DF in sample-P is larger than the value of sample-N, indicating that the optical quality of the WZ-on-ZB interfaces is lower.

The small difference in E_1 between the two samples means that the non-radiative recombination is asymmetric for both the ZB-on-WZ and WZ-on-ZB interfaces.

Asymmetry at heterostructure interfaces was previously observed in non-common-atomic structures such as InAs/GaSb superlattice, It is different here that the interface in NWs is formed with the same atoms but different crystal phases, which is reversal to the case in InAs/GaSb structures.

On the other hand, the difference in C_2 of DF implies that the possibility of thermal electron transfer between ZB phases and WZ phases is different. Such asymmetry in the optical properties of ZB/WZ-phases interface provides new approach towards understanding nanoscale semiconductors.

The optical asymmetry of the ZB-on-WZ and WZ-on-ZB interfaces is also affected by the considerable different carrier-phonon interactions between the two samples. It is known that b is positively correlated with the Fröhilich coupling constant $C_F \propto \sqrt{\varepsilon_{LO}\left(\epsilon_\infty^{-1} - \epsilon_0^{-1}\right)}$. The remarkable difference of b between sample-N and sample-P may indicate a change in the dielectric coefficient ε variation around the ZB-on-WZ and WZ-on-ZB interfaces as ε_{LO} is almost the same for both samples. LEF also exhibits significant differences in carrier-phonon interactions and may suggest LEF-related impurities at the interface.

4.3 Sb-modulated InAs NWs

In the last section, InAs NWs with high-quality grown on N- and P-type Si was discussed detailedly modulated mid-infrared PL method based on a step-scan FTIR spectrometer in a wide temperature range up to 290 K. For the application as advanced photonic devices, the binary of InAs is unable to cover the entire mid-infrared range. For instance, $InAs_{1-x}Sb_x$, known as the III-V semiconductor of smallest bandbap energy, has wide application in photonics, due to its advantages such as tunable direct bandgap rang-

ing from 0.350 to 0.145 eV, small effective mass (0.023 m_e), very high electron mobility ($\sim$ 30000 $cm^2V^{-1}s^{-1}$ at 300 K), a large Bohr radius ($\sim$ 34 nm) [57] and easily forming of superlattice. Consequently, InAsSb alloys became an ideal candidate for high performance optoelectronics operating in MWIR and LWIR spectral range ($2-8$ µm) [58], as well as high-speed electronic devices. Amongst these device applications, utilising InAsSb as infrared photodetectors have obtained considerable attention in the past few years to replace HgCdTe based detectors which suffer from toxicity issues [59]. But it is not easy to realize the epitaxial growth of InAsb NWs with high Sb content due to the strong surfactant effect. And realizing high-performance conventional thin-film InAsSb devices still remains as a big challenge due to the large lattice mismatch between the available substrates and the InAsSb epilayer, which creates dislocations subsequently severely, degrades the devices performance. From this perspective, 1-D InAsSb NWs have been proposed to be a promising architecture to overcome the restrains of the lattice-match. Due to the small foot area, NWs are capable to readily release the strain resulting in dislocation free materials. This feature also enables epitaxial growth on inexpensive substrates such as Si substrate which advances in photodetectors arrays integrating with CMOS. To use the advantages of InAsSb NWs, the study of Sb incorporation would be first done in this section. And the effect of Sb on the structural phases and emission energy would be investigated as follow-up. For simplicity, InAsSb would be used as the alternative for $InAs_{1-x}Sb_x$ in this section, and sometimes $InAs_{1-x}Sb_x$ would occur just to emphasize the Sb composition.

4.3.1 Sb Incorporation in InAsSb NWs

During the formation of InAsSb alloys, Sb is an additional element involved in the reaction with In, comparing to the formation of InAs binary NWs. In the growth of InAs in the As-rich condition, part of the As combines with In generating InAs, and most of the other As exists to maintain the non-equilibrium state. Similarly, Sb combines with In forming InSb when typical material of InSb is grown in MBE. When both As and Sb

exist, In will be taken from As and shared with Sb. At this point, As and Sb maintain competition. Therefore, when the flux of In is fixed, the Sb content in terms of x in InAsSb alloy is supposed to be dual function of As and Sb as:

$$x = f(F_{\mathrm{As}}, F_{\mathrm{Sb}})\,, \tag{4.6}$$

where F_{As} and F_{Sb} are the flux of the As and Sb, respectively.

Considering the difference in the binding ability of indium to arsenic and antimony, when some fixed As and Sb flux is used, the change of In will also cause the change of value of x.

Thus, the above Equation 4.6 could be modified as:

$$x = f(F_{\mathrm{In}}, F_{\mathrm{As}}, F_{\mathrm{Sb}})\,. \tag{4.7}$$

Therefore, it is also necessary to consider the flux of In relative to the whole V-group flux

$$F_{\mathrm{V}} = F_{\mathrm{As}} + F_{\mathrm{Sb}}\,, \tag{4.8}$$

and V/III flux ratio

$$FR_{\mathrm{V/III}} = \frac{F_{\mathrm{III}}}{F_{\mathrm{V}}} = \frac{F_{\mathrm{In}}}{F_{\mathrm{As}} + F_{\mathrm{Sb}}}\,. \tag{4.9}$$

In the real growth of InAsSb, it is easier to measure the total flux of both As and Sb, and the flux of Sb is generally more concerned and recorded by the growers, so the Sb fractional flux is essential and should be defined as

$$FF_{\mathrm{Sb}} = \frac{F_{\mathrm{Sb}}}{F_{\mathrm{Sb}} + F_{\mathrm{As}}}\,. \tag{4.10}$$

Mathematically, among the many factors F_{As}, F_{Sb}, $F(V)$ and $FR_{\mathrm{V/III}}$, the choice/group

of F_{Sb} and $FR_{\mathrm{V/III}}$ is complete. In this sense, the equation could be written as

$$x = f(F_{\mathrm{In}}, F_{\mathrm{Sb}}, FR_{\mathrm{V/III}}). \tag{4.11}$$

The physical significance of the above equation could be understood as the following 3 points:

the composition of Sb is affected by the flux of In, when the flux of Sb and As is fixed;

the composition of Sb is affected by the flux ratio of V/III group , when the flux of Sb and Sb fractional flux is fixed;

the composition of Sb is affected by the Sb fractional flux, when the flux of In and the flux ratio of V/III group is fixed.

which are equal to:

the composition of Sb is affected by the flux of In, when the flux of Sb and As is fixed;

the composition of Sb is affected by the flux of Sb, when the flux of In and As is fixed;

the composition of Sb is affected by the flux of As, when the flux of In and Sb is fixed;

Nevertheless the former saying is measurable more experimentally convenient.

And as a brief summary, Sb flux is an important factor affecting the Sb composition of Sb in the ternary alloy of $InAs_{1-x}Sb_x$ NWs. By tuning the Sb flux, $InAs_{1-x}Sb_x$ NWs with different composition of Sb are expected to be achieved via MBE. But Sb flux is not the only factor we concern. This technique of tuning the Sb flux should be combined with a proper V/III flux ratio to achieve high Sb composition. In another word, the composition of Sb may be affected by at least two of the factors when In flux is fixed: V/III flux ratio and Sb flux. So the first part of this section would be focused on studying the Sb incorporation by growing a series of samples at different V/III flux ratio and Sb flux. By this way $InAs_{1-x}Sb_x$ NWs with different content of Sb element will be discussed. The growth condition of InAsAb NWs is similar to the growth of InAs NWs previously established in Sec. 4.1 via droplet-assisted technique. The only difference is that the

shutters of As and Sb were opened simultaneously instead of only openning the shutter of As to achieve InAsSb ternary alloy.

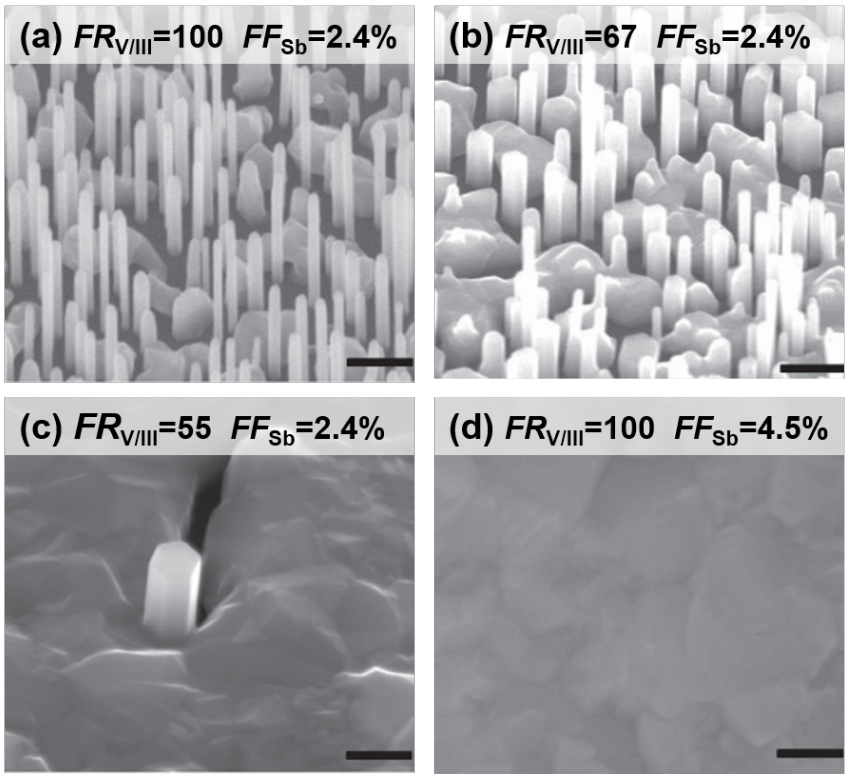

Figure 4.14: SEM images tilted 45°of InAsSb NWs grown under different V/III ratio and Sb fractional flux.

The geometry of the resulting InAsSb NWs was investigated by SEM as Fig. 4.14 shows. InAsSb NWs were obtained at Sb fractional flux of 2.4% with different V/III flux ratios such as 100, 67, and 55, respectively shown in Fig. 4.14 (a), (b), and (c). Firstly, Sb fractional flux was fixed at 2.4%. The InAsSb NWs grown at the V/III flux ratio of 100 in Fig. 4.14 (a) are uniform and smooth, similar to Fig. 4.1. While the V/III flux ratio was reduced to 67, shown in Fig. 4.14 (b), the InAsSb NWs grown not as long as the NWs grown at the V/III flux ratio of 100 as the Fig. 4.14 (a) shows, and the diameter increase obviously. But the areal density doesn't change significantly. When the V/III flux ratio was further reduced to 55, both the lengh and areal density of InAsSb NWs drops dramaticly, as shown in Fig. 4.14 (c), meanwhile the diameter increases further. It can be

seen from the above three SEM images from experimental data of these three continuity InAsSb NWs can be achieved under the Sb fractional flux of 2.4%. Higher V/III flux ratio favors the growth of InAsSb NWs at fixed Sb fractional flux. As the V/III flux ratio decreases with the fixed Sb fractional flux of 2.4%, the geometry InAsSb NWs changes: the length and areal density decreases but the diameter increases. However, when the Sb fractional flux was increased to, even a higher V/III flux ratio of 100 can not result any NWs but film growth as shown in Fig. 4.14 (d).

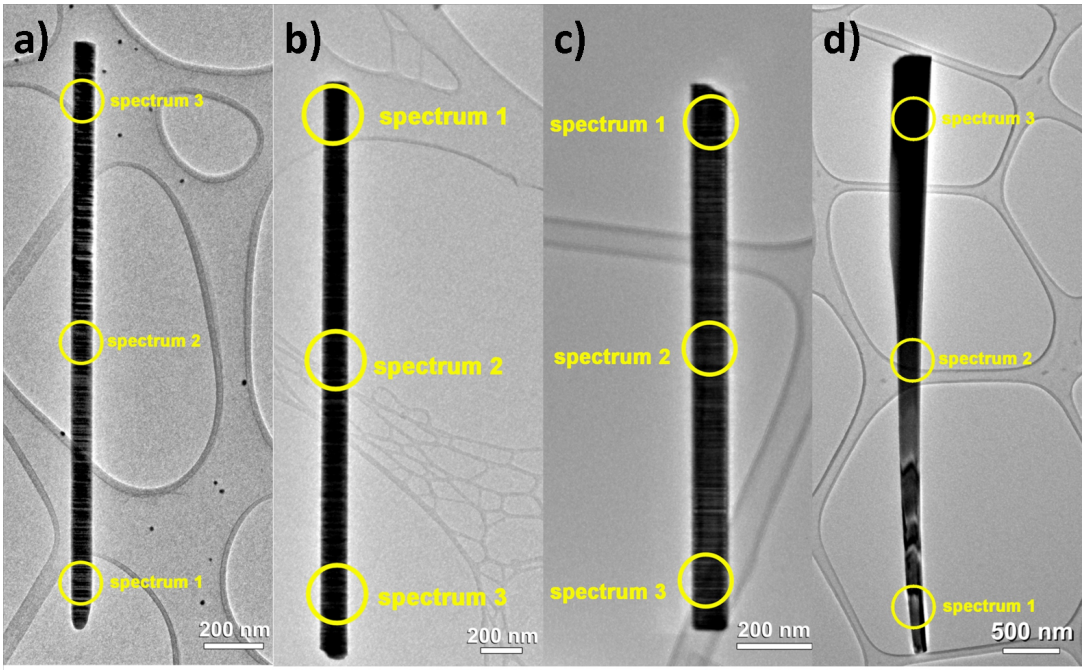

$InAs_{1-x}Sb_x$

Spectrum	1-x (%)	x(%)
1	98	2
2	97	3
3	98	2

$InAs_{1-x}Sb_x$

Spectrum	1-x (%)	x(%)
1	89	11
2	89	11
3	88	12

$InAs_{1-x}Sb_x$

Spectrum	1-x (%)	x(%)
1	83	17
2	84	16
3	85	15

$InAs_{1-x}Sb_x$

Spectrum	1-x (%)	x(%)
1	81	19
2	82	18
3	83	17

Figure 4.15: EDX point analysis for individual NWs on four samples giving an average Sb content of (a) 3%, (b) 11%, (c) 16% and (d) 18%, with the content at different positions along the individual NWs.

To determing the Sb composition and fluctuation of InAsAb NWs grown under different conditions, EDX measurements was carried out with an Oxford Instrument X-MAX 80, which is integrated in the TEM system. NWs were scraped from the substrates mechanically using clean tweezers and then deposited gentelly on holey carbon grids for TEM

measurements in a JEOL-JEM 2100 microscope working at 200 kV. In order to reliably determine the Sb composition and reveal the relationship between Sb composition and growth condition, EDX point analysis was conducted on each sample at different locations along individual NWs. Four samples were chosen from the samples we grew at different condition. Fig. 4.15 shows typical TEM / EDX analysis data for each individual InAsSb NWs samples, with Sb content at three different locations shown in the inset table. The average Sb content of the four NWs is 3%, 11%, 16% and 19%, respectively, while small fluctuation in the Sb content exists along the growth direction of the NWs. Based on the further EDX measurements at more points along the growth direction of each individual NW, the fluctuation of Sb composition is able to be determined. Fig. 4.16 shows the relationship of Sb composition on Sb fractional flux and V/III flux ratio. As the FF_{Sb} increases, the amount of Sb incorporation increases monotonically, as shown in Fig. 4.16 (a). This phenomenon is easy to understand. Under the fixed V/III flux ratio, a higher FF_{Sb} helps In combine with more Sb and reduce the incorporation of As in the competition with it, thus forms a higher Sb composition. This can also be understood as a higher FF_{Sb} contributes to Sb replacing As. At the same time it should be noted that Fig. 4.14 (d) indicates under our early growth conditions, any FF_{Sb} greater than 2.4% will result in difficulty in the growth of InAsSb NWs. According to this experimental phenomenon, it is likely not possible to increase the Sb composition by increasing FF_{Sb} too high. In Fig. 4.16 (b), the reduction of the V/III flux ratio from 100 and 67 to 55 results in an Sb content increasing of from 10% and 16% to 19%, respectively. This implies a reduced V/III flux ratio favours the growth of InAsSb NWs and enhances the Sb incorporation. It should be noted here that the reduction of the V/III flux ratio was realized by increasing the growth rate, *i.e.*, the flux of In. It is shown that a faster growth rate increases the Sb incorporation, and it is believed that this is related to the reduction of the Sb surfactant effect.

Jumping out of the specific analysis of Sb content, the successful growth of InAsSb

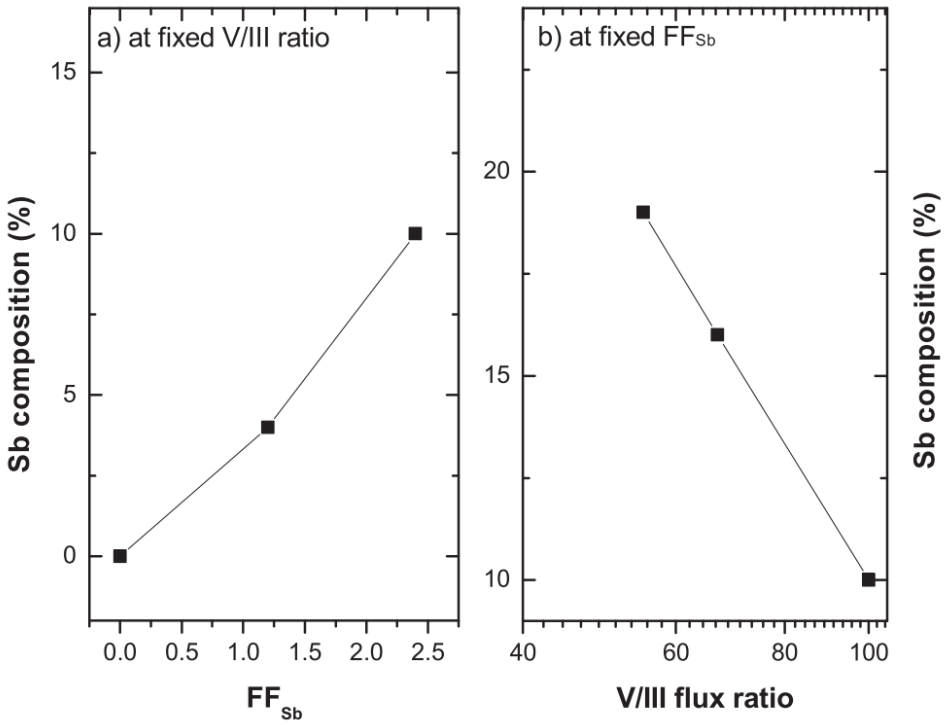

Figure 4.16: (a) The Sb composition as a function of FF_{Sb} under a fixed V/III flux ratio of 100, and (b) the Sb composition as a function of V/III flux ratio under a fixed FF_{Sb} of 2.4%.

NWs significantly depends on V/III flux ratio and growth rate. Therefore, special attention must be paid to the carefully-tuning of the above two factors in order to maintain the NW growth. In addition, the higher Sb incorporation helps to generate shorter and thicker InAsSb NWs and causes a significant drop in areal density: when the Sb content increases from 16% to 19%, the areal density drops from $5 \times 10^9\,\mathrm{cm}^{-2}$ to $3 \times 10^7\,\mathrm{cm}^{-2}$, which agrees with previous reports [60]. It is also noticed that the length of the NW taken by the TEM measurement is much longer than the length as-grown InAsSb NWs in the SEM images. This should be related to the method we used to catch the NWs for TEM measurements. During a copper grid was used to gently scribe the surface of the samples, longer NWs are much eaisier to be collected among all the NWs standing on Si substrate, which results the longer length than the average length carried out from the as-grown samples.

4.3.2 Phase transition in InAsSb NWs modulated by Sb

It is well known that the optical properties of NWs depend greatly on the crystal quality of the nanowires, especially the crystal phase represented by the amount of pure crystalline phases and stacking faults. It is also easy to understand that the growth techniques (such as the droplet-assisted growth technology used in this work) and the growth process determine the crystalline quality of the NWs. Based on the above two considerations, it is necessary to study the crystal quality of nanowires: on the one hand, it can directly reflect and evaluate how good the growth of NWs is, and on the other hand, it can be used as an important reference to explain the optical properties of NWs.

In addition to being a technical means of studying the composition of NWs, HRTEM is a natural measurement technique used in this section to study the crystal quality of NWs. As an effective means, fast Fourier electron diffraction patterns have also been taken to evaluate the crystaline quality of NWs.

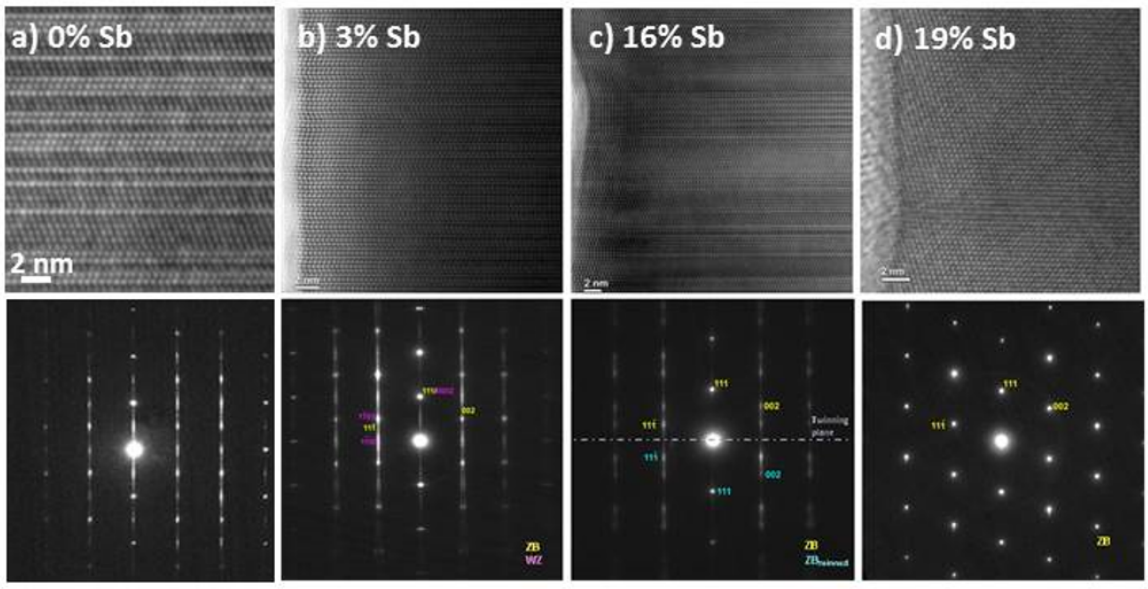

Figure 4.17: High-resolution TEM images of the InAs NWs(a) and InAsSb NWs with an Sb content of (b) 3%, (c) 16%, and (d) 19%.

Fig. 4.17 contains typical HRTEM images of a series of InAsSb nanowires with differ-

ent Sb contents. It can be seen that all NWs with an Sb content of less than 16% exhibit a mixture of ZB and WZ segments. Thanks to the high definition of the captured images, size of segments for each phase can be carefully counted and analyzed. The results show that the average length of the different phases in each sample strongly depends on the amount of Sb incorporated, as shown in Fig. 4.19: as the Sb incorporation increases, the size of the ZB and WZ segments generally increases, but the size of WZ segments in the InAsSb NWs with high Sb composition (such as 16% and 19%) start to decrease. As a reference, the ZB and WZ segments in InAs nanowires are approximately equal in size, which means the phases are grown randomly and unmodulated. When there is a small amount of Sb doped to form low Sb content (2% to 10%) of InAsSb NWs, the size of WZ segments is slightly larger than ZB; however, for samples with higher Sb content (such as 16% and 19%), the situation is reversed: the size of the ZB segments is larger than that of the WZ segments. More importantly and interestingly, the NWs containing 19% Sb exhibited an extreme case, showing a quasi-pure ZB crystaline phase as shown in Fig. 4.17 (d). The corresponding Fast Fourier electron diffraction pattern also reflects this significant change, as shown in the bottom panel of Fig. 4.17. In Fig. 4.17, the growth directions of the ZB and WZ phases are represented by <111> ZB (yellow and turquoise) and <0002> WZ (magenta) points, respectively. Along this growth direction, there are some streaks that pass through the above-mentioned spots, which indicates that the structure of the NWs is not pure, but there are stacking faults, which are usually located at the interface of ZB/WZ phases. In the bottom panel of Fig. 4.17, as the composition of Sb gradually increases, the number of stripes gradually becomes lighter and the brightness gradually reduces. Especially for InAsSb NWs containing 19% Sb, almost only the spots remain in the diffraction pattern, and these spots are the most bright in the several graphs shown in the bottom panel of Fig. 4.17. This reflects that the NWs in this sample have almost pure WZ phase and are of high purity.

As Dheeraj *et al.* reported that the presence of Sb favours the formation of the ZB

phase in GaAsSb NWs [61], the following facts have been confirmed by our previous publication [62]: the crystal structure of InAsSb NWs with increasing Sb incorporation initially evolved from mixture of WZ and ZB to a crystal structure dominated by WZ, and when the Sb content is higher than 10%, it is changed to dominate by the ZB phase, which would be shown in Fig. 4.19 in later. Fig. 4.17 does not contain data with Sb content around 10%, but the these data with more in-depth discussion will be shown below.

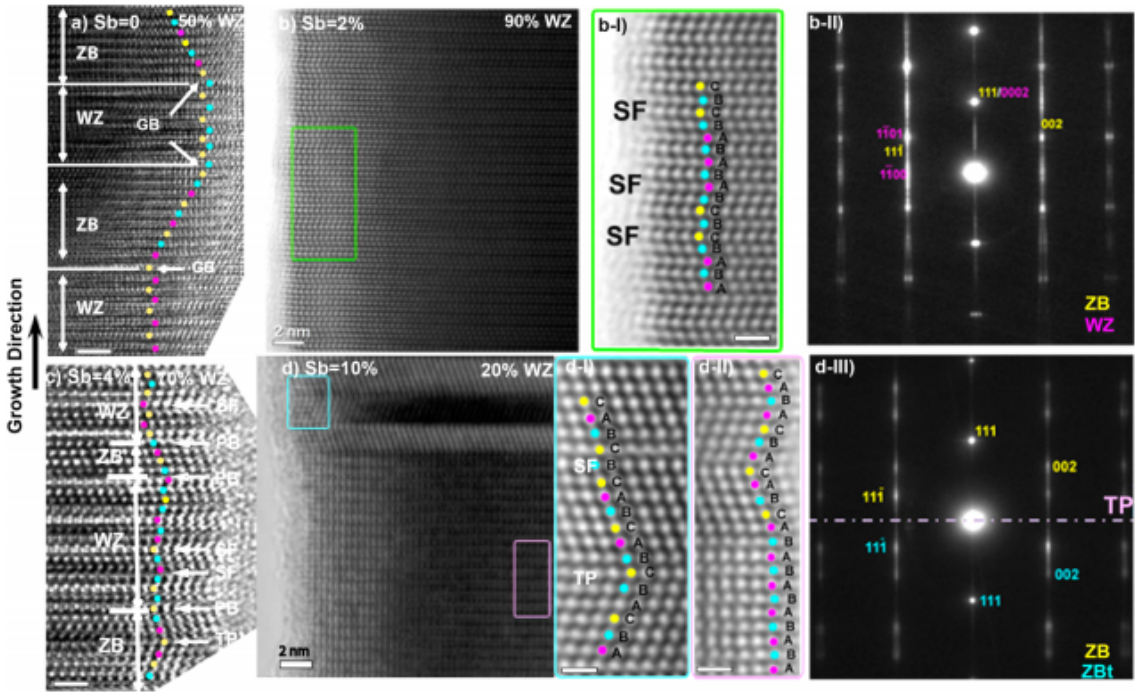

Figure 4.18: HRTEM images of 4 samples of InAsSb NWs with Sb content of (a) 0%, (b) 2%, (c) 4%, and (d) 10%, respectively. Magnified HRTEM image (b-I) of the highlighted region of sample (b), with the corresponding FFT pattern (b-II); Magnified HRTEM images (d-I) (d-II) of the highlighted regions of sample (d), with the corresponding FFT pattern (d-III). ZB and WZ structures and SFs TPs are also shown in these magnified images marked with yellow / turquoise / magenta points. The scale bar is 1 nm.

To better quantify the distribution of polymorphs and crystalline defects in NWs, HRTEM was used again focusing on the InAsSb samples with Sb composition in the range from 0% to 10% as Fig. 4.18 shows. Silimar to Fig. 4.17, these InAsSb NWs crystallize in the mixed phases of WZ and ZB, and exhibit a mixture of phases with planar defects. Here

three categories of defects were classified: SFs, TPs, and poly-type boundaries (PBs). In order to estimate the percentage of WZ phases in the NWs, we used the metrics proposed by Caroff *et al*. [63]. In this method, the segments consisting of more than four stacking sequence consequences should be treated as a particular crystalline phase. The PBs are the planes between ZB and WZ phases whose density implies the size of segment of the phases. We did not count the density of PBs in our defect density analysis. PBs locate on the planes between the ZB and WZ phases, and the density reflects the size of the phase segmentation for ZB and/or WZ phases. For simplicity, we did not calculate the density of PB in the defect density analysis below.

The left part of Fig. 4.18 shows the HRTEM images of the samples of reference InAs NWs Fig. 4.18 (a) and InAsSb NWs with Sb composition of 2%, 4%, and 10% in Fig. 4.18 (b)-(d). The highlighted green region in the sample (b) is shown in Fig. 4.18 (b-I) as a magnified HRTEM image. Its corresponding FFT pattern is shown in Fig. 4.18 (b-II). Similarly, the highlighted turquoise & magenta regions in the sample (d) are shown in Fig. 4.18 (d-I) and (d-II). Its corresponding FFT pattern is shown in Fig. 4.18 (d-III). ZB and WZ structures and SFs & TPs are also shown in these magnified images marked with yellow / turquoise / magenta points. In Fig. 4.18 (a), the reference InAs NWs exhibit a mixed ZB/WZ crystalline structure (50% WZ) along with defects of PBs and low density of SFs and TPs, comparing with the InAsSb samples in Fig. 4.18 (b-I) (c) (d-I) and (d-II), which agrees with Fig. 4.17 (a). This phenomenon is very common in self-catalyzed InAs NW, phases grown randomly and unmodulated. And it is normally attributed to the type of materials and the effects of lateral surfaces on the total free energy during the self-catalyzed epitaxy [64].

On the one hand, this is related to the type of materials. When we look at bulk III-V materials, III-nitride materials usually have the high ionicity, so WZ phases appear preferentially in those materials, while ZB phases tend to exist in other III-V materials. Unfavorable consequences appear when ionicity is at some suitable value, often leading to

a strong tendency to form SFs, TPs and polymorphism, which affects most of other III-V NWs materials including InAs, InP, GaAs and GaP. On the other hand, in addition to the type of material, this is also determined by the stacking order of atoms in the WZ and ZB crystalline phases. The WZ phases have lower surface energy than the ZB phases of the same material, because the difference in the order of atom stacking between the two phases results in a smaller third-nearest-neighbor atomic spacing of the WZ phase. In structures with a high surface-to-volume ratio (such as NWs with small diameters), this effect is more pronounced, resulting in a more stable WZ phase. Another natural inference is that the probability of occurrence of polymorphs in III-V NWs is usually related to the diameter of NW. The smaller diameter contributes to the formation of the WZ crystal phase because the smaller diameter helps to increase the relative contribution of the lateral surfaces to the total free energy during the growth of NWs. Based on the above two points, this natural is generally independent of the synthesis methods and is difficult to avoid completely.

Addition of Sb with content of 2% and 4% results in WZ predominant phases as shown in Fig. 4.18 (b)&(c), while further increase of Sb content (10%) leads to ZB predominant structure as shown in Fig. 4.18 (d).

The InAsSb NWs sample with Sb content of 2% in Fig. 4.18 (b) shows the WZ dominant crystal structure (up to 90%). Different from the dominated ZB phases in InAs NWs, this significant crystal changes to WZ phases are attributed to the small incorporation of Sb, which is a phenomenon reported for the first time by us. For a closer look at the stacking of atoms, a magnified image of HRTEM for the WZ phase section is exhibted in Fig. 4.18 (b-I). In this image, stacking corresponding to the WZ structures (...ABAB ... and ... CBCB ...) and intrinsic SFs (ABABCBCBC) is clearly displayed respectively. The quasi-pure WZ structure of NWs is evidenced by the corresponding FFT electron diffraction pattern, as shown in Fig. 4.18 (b-II). The spots of <111> ZB (yellow) and <0002> WZ (turquoise) indicate the growth directions of the ZB and WZ phases, respectively. It clearly shows that the WZ reflection is more intense than the ZB

reflection, further supporting the dominated structure of the WZ phases. The streaks passing through the spots along the growth direction indicate the presence of stacking faults in the structure, locating on the <111> ZB / <0002> WZ interfaces.

The InAsSb NWs sample with a higher Sb composition of 4% in Fig. 4.18 (c) still shows a quasi-pure WZ structure (about 70%) but slightly lower than the sample of $InAs_{0.98}Sb_{0.02}$. This observation contradicts previous reports on catalyst-free $InAs_{1-x}Sb_x$/InAs NWs [65], which observed a phase transition from WZ to ZB at a Sb incorporation of 3.9%. Considering the differences in supersaturation related to the pre-positioning of indium (In) in our growth technique against the catalyst-free growth techniques, the difference between these two results can be understood. Based on the regulation of the diameter of the NWs as explained above, the direct deposition of In on the Si substrate before the growth of NWs leads to the difference in contact angle and diameter of NWs, which are considered to be the two essential determinants of the NWs crystalline phases in the relevant reports [66, 67].

In addition, slight changes in growth conditions may result in different crystaline phases, so it has become a common means to tune crystal phase transitions by adjusting growth parameters. For the sample of InAsSb NWs, when the Sb composition was further increased to 10% in Fig. 4.18 (d), unexpectedly, we observed that ZB became the dominated phase, only accompanied by a small amount of WZ (about 20%). This means that the phase transition of WZ $\rightarrow$ ZB occurs at the Sb incorporation level of around 10%. Fig. 4.18 (d-I) is an magnified view of the turquoise region in the NW, clearly showing that the ZB(....ABCABC ....) stack contains both TPs (... CBA C ABC ....) and SFs (... ACBCBAC ....). At the same time, a region corresponding to the WZ phases was also observed in the sample, as shown in Fig. 4.18 (d-II). This structure is confirmed by the FFT pattern recorded from the NWs, as shown in Fig. 4.18 (d-III). The spots in the diffraction pattern indicate that the ZB phase dominates, accompanied by the presence of TPs. As previously mentioned, the streaks indicate the presence of SFs, which is less

pronounced than that of $InAs_{0.98}Sb_{0.02}$ NWs in Fig. 4.18 (b-II), indicating a lower density of SFs in this sample.

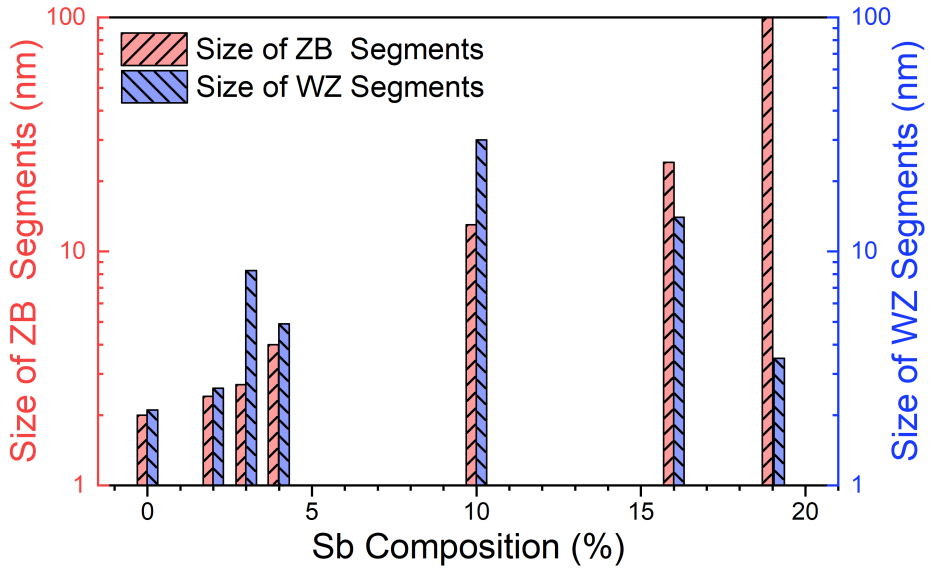

Figure 4.19: Average size of ZB and WZ segments in the InAsSb NWs as a function of Sb composition.

To clearly and directly summarize the effect of Sb incorporation on crystal structure changes in NWs, we analyzed the TEM images of multiple NWs and multiple fragments in each NW sample shown in both Fig. 4.17 and Fig. 4.18, trying to determine the percentage of crystalline phases in different samples and the percentage of related different defects, especially the distribution of SFs and TPs in NWs. The relationship between the percentage of the WZ crystalline phase and the Sb content is plotted in Fig. 4.20 (a). It clearly shows that with a small amount of Sb incorporation (up to 4%), polycrystalline mixed InAs NWs is effectively tuned to WZ-dominated $InAs_{1-x}Sb_x$ NWs; while further increase in Sb leads to dominance of ZB phases. The average fragment size of each phase of the samples in Fig. 4.17 and Fig. 4.18 was also statistically analyzed, showing a strong dependency on incorporation of Sb as shown in Fig. 4.19. As the amount of Sb incorporation increases, the average size of the ZB and WZ segments generally increases in the range of 0% to 10%; while in the range of 10% to 19%, the trendency of average segment

size of the ZB and WZ phases deviates. For InAs NWs, the ZB and WZ segments are approximately equal in size. For InAsSb NW with a small amount of Sb ($< 10\%$), the WZ segment size is larger than the ZB size; while for samples with higher Sb content ($> 10\%$), the segment size of ZB phases is much larger than that of WZ phases. More importantly, the sample of $InAs_{81}Sb_{19}$ exhibts pure ZB phase.

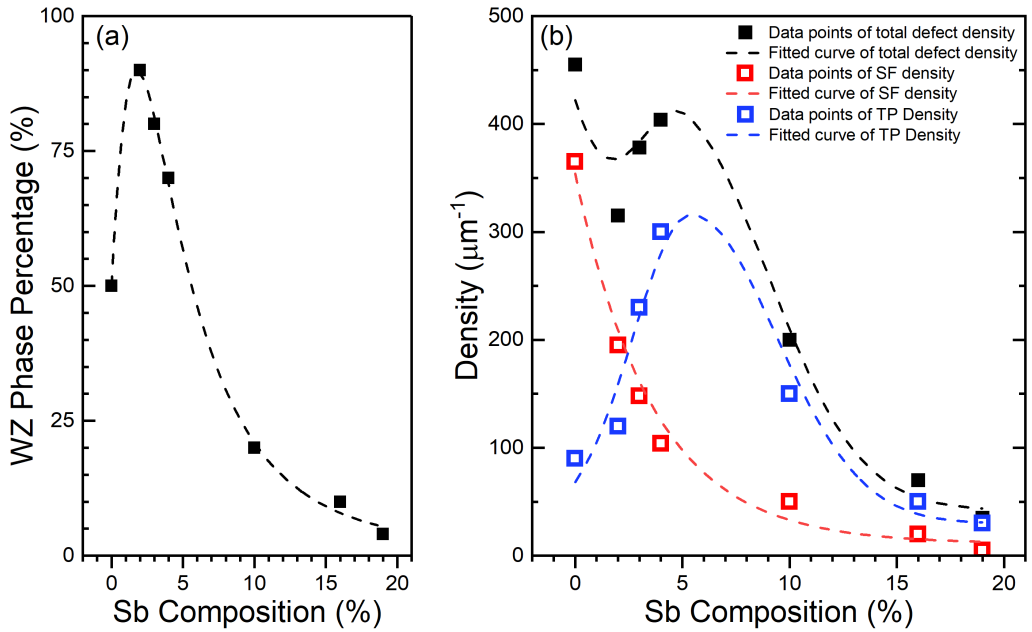

Figure 4.20: Wurtzite phase percentage and total defect density (a), stacking fault (SF) and twin plane (TP) density (b) in InAsSb NWs as a function of antimony composition.

In summary, Sb incorporation provides an effective way to modulate the crystalline phases of $InAs_{1-x}Sb_x$ NWs. The increase in Sb incorporation results in a transition from polymodal mixture $\rightarrow$ WZ $\rightarrow$ ZB, and proper incorporation of Sb can reduce the density of SFs, which is consistent with the observations reported by J. Marion *et al.* [68]. This reduce of SFs is believed to improve the optical properties of the NWs.

4.3.3 Optical properties of InAsSb NWs modulated by Sb

As the Sb incorporation increases, it is expected that the optical properties of InAsSb NW will undergo interesting changes. This change may come from two aspects: One is

that the composition change of Sb in the InAsSb alloy will significantly tune its bandgap, and the second is that the abundant phase transition modulated by the incorporation of Sb will diversify the carrier recombination. A diode laser with wavelength of 980 nm was used as the excitation source, and the areal power density of the excitation light is about 20 Wcm^{-2} (the laser power is 200 mW, and the laser spot was about 1 mm^2). The emitted light was collected and dispersed by a monochromator, then passed a lock-in amplifier and was detected by a HgCdTe photodetector operating cryogenically. In addition, infrared modulation PL method based on step-scan FTIR is used for more detailed measurements such as temperature-dependent and power-dependent scanning [69, 70].

Similar to Sec. 4.1, the PL spectrum of the grown sample was taken at low temperature (10 K) shown in Fig. 4.21. The typical PL spectra of InAs NWs and $InAs_{0.96}Sb_{0.04}$ NWs are shown in Fig. 4.21, respectively. Similar to Fig. 4.6 (a) and Fig. 4.7, InAs NWs have multi-peak emission Fig. 4.21 (a). The decomposition shows that the three emissions locate at 0.389, 0.415 and 0.434eV, respectively. The highest energy emission is associated with the interband between ZB InAs BtB transitions, while the lowest emission is related to impurities and/or defects [71], and the central emission located at 0.415 eV is attributed to the presence of the WZ / ZB mixed phases. The InAs mixed with WZ and ZB phases forms a type-II QWs, in which electrons are confined in the QWs of the ZB segments and the holes are located in the WZ region [72]. The optically excited electrons fall from the bottom of the conduction band of the WZ region to the bottom of the conduction band of the adjacent ZB phases, and the holes float from the top of the valence band of ZB phases to the top of the valence band of the adjacent WZ phases. The electrons confined at bottom of the conduction band of the ZB QWs and the holes at the top of the valence band of the adjacent WZ phases are then combined to emit photons (type-II QW-related emission) [73]. A corresponding radiation mechanism is already shown schematically in Fig. 4.12 (c). The emission energy from this type-II QW transition (0.415 eV) is very consistent with previous reports on polycrystalline InAs NWs [73].

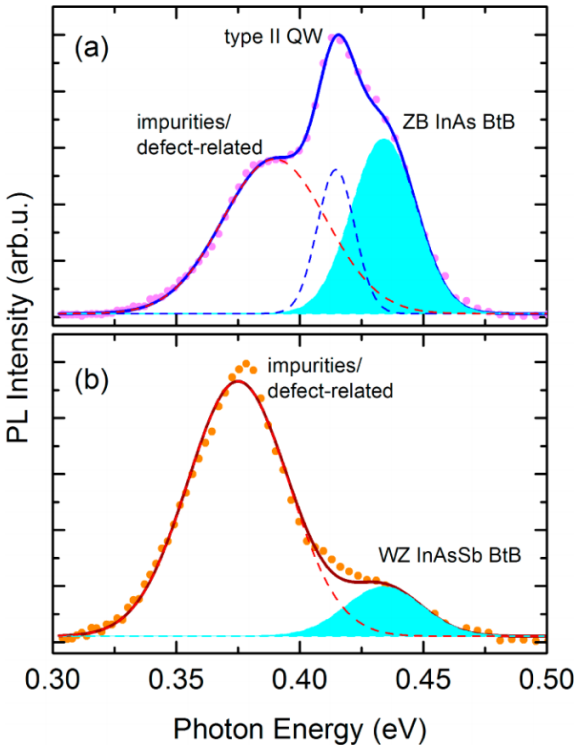

Figure 4.21: PL spectra of (a)InAs and (b)$InAs_{0.96}Sb_{0.04}$ NWs at 10 K.

For the $InAs_{0.96}Sb_{0.04}$ NWs sample, the PL spectrum shows only two emission peaks locating at 0.437 eV and 0.375 eV as shown in Fig. 4.21 (b), corresponding to BtB transitions and impurities and/or defects in the WZ phase InAsSb, respectively. It is worth noting that, unlike Fig. 4.21 (a), no emission associated with type-II QW transitions has been observed in this sample, which is in good agreement with the crystal structure exhibited by the HRTEM study: the crystal structure of NWs evolved from a highly polymorphic crystal in InAs NWs to a quasi-pure WZ phase crystal in $InAs_{0.96}Sb_{0.04}$ NWs sample. This optical result is further evidence for the mixed phase InAs NWs transform into quasi-pure WZ phases in $InAs_{0.96}Sb_{0.04}$ NWs due to Sb incorporation. Although InAs(Sb) clusters were present on the Si surface, the PL emissions detected on the as-grown samples were considered to be derived from the NWs samples. This is confirmed by the vanish of PL emission when the NWs are removed. After the NWs were removed, only clusters were present on the Si substrates. These clusters were grown after the seeding of droplets due

to antiphase domains and large lattice mismatch, and thus their crystal quality was very poor, just resulting in no observable emission from these clusters.

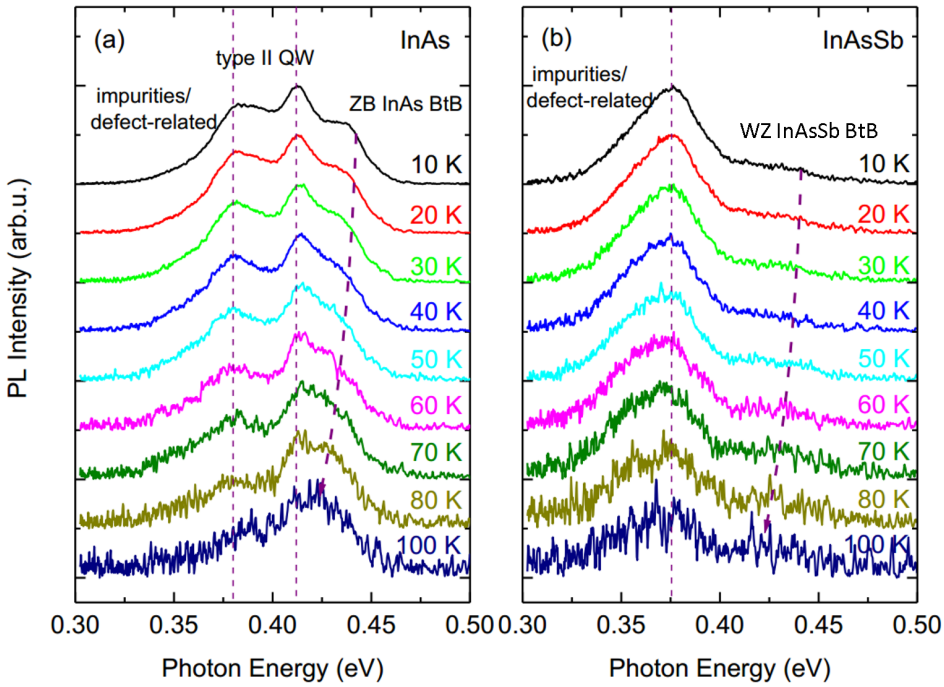

Figure 4.22: Temperature-dependent PL measurement of InAs NWs (a) and InAsSb NWs (b) under laser power of 200 mW.

Power-sweeping and temperature-sweeping PL measurements were also performed on the two samples to further verify the origin of the emission peaks. Through these detailed PL measurements, the source of the peak can be fully confirmed. It is worth noting that the BtB emission of InAs NWs at 0.427 eV is slightly higher than the bandgap of ZB InAs (0.415 eV). This larger energy may be related to the band filling effect and size quantum confinement in NWs. Sun *et al*. reported the blueshift of the InAs bandgap due to the size-dependent quantum confinement effect in NWs with small diameters ($10-20$ nm) [71]. Although our InAs NW has a large average diameter (about 50 nm), in the view of the uneven distribution of their diameters, NWs with diameters less than 25 nm exist in large quantities, and it is they that cause significant size-related quantum confinement effect and result in a blue-shifted and a bit broad emission peak.

Unexpectedly, the BtB emissions of WZ $InAs_{0.96}Sb_{0.04}$ NWs are centered around the energy of 0.437 eV, which is close to the BtB emissions of ZB InAs NWs. This result contradicts the forecast of lower bandgap energy assosiated with Sb incorporation, but it is also not incomprehensible. Instead, this can be explained by the difference in bandgap energy of the different phases. It is reported that WZ phase InAs NW has a larger bandgap energy than ZB InAs by in recent research, with a theoretical value of $40 - 66$ meV, experimental observations with value of 0.46 eV confirmed this by the way. For the low Sb component ($< 5\%$) in $InAs_{1-x}Sb_x$ alloy, we can consider the bandgap energy difference between the WZ/ZB phases is independent of the Sb content, then the bandgap energy of the WZ $InAs_{1-x}Sb_x$ can be derived from the the bandgap energy of ZB $InAs_{1-x}Sb_x$ ($x < 5\%$). When the Sb is 4%, if the bending effect of 0.67eV (shrinkage is 0.035 eV) is used, the bandgap energy of ZB $InAs_{0.96}Sb_{0.04}$ alloy is 0.375 eV. From this view, it can be estimated that the bandgap energy of WZ $InAs_{0.96}Sb_{0.04}$ is about $0.415 - 0.441$ eV, and it is very important that this forecast is consistent with the calculated energy value from our PL spectrum.

From the above discussion, we can confirm that the emission at 0.437 eV is from the BtB transition of WZ $InAs_{0.96}Sb_{0.04}$ in spite of quantum confinement effects. Due to the large diameter (109 nm) of these NWs, according to the results of Sec. 1.8.2.2 and 1.8.2.3, we believe that the quantum confinement effect in these NWs is so weak compared to that of InAs NWs that it should be negligible, because $InAs_{1-x}Sb_x$ NWs with small diameters barely exist when Sb is incorporated. Another point to be mentioned is that the emissions associated with impurities and/or defects are strong in both samples, which may be related to the presence of high-density TPs and/or SFs, which is not beyond the previous HRTEM and FFT results in Sec. 4.3.2.

In order to clarify the regulation of Sb incorporation on the optical properties of $InAs_{1-x}Sb_x$ NWs, we performed PL measurements at 10 K on five as-grown samples with different Sb content up to 19%. The stacked curves in Fig. 4.23 reflects the evolution of PL

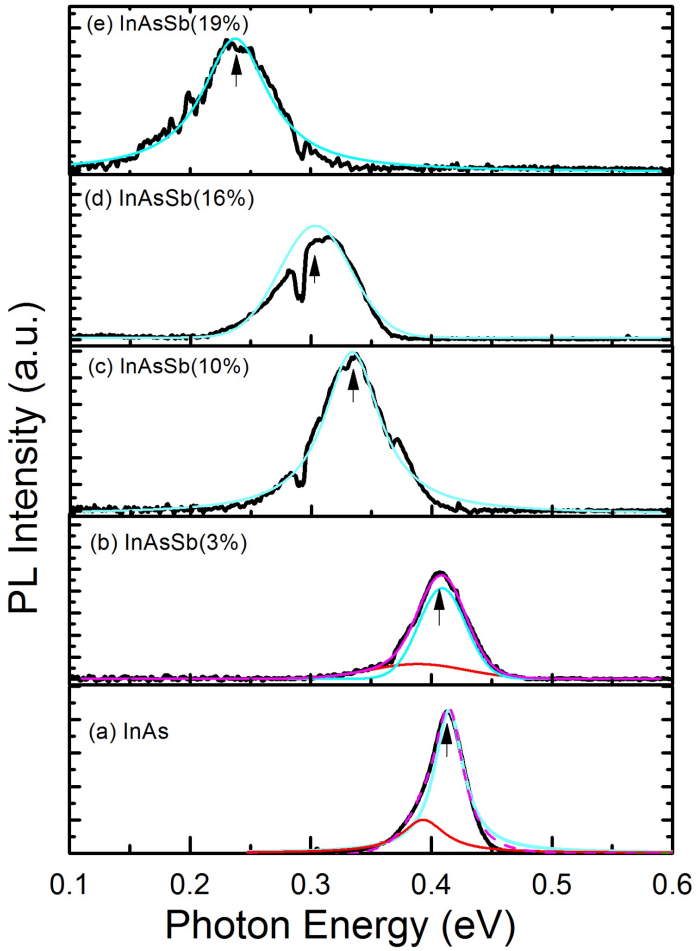

Figure 4.23: The evolution of 10 K PL of InAs NWs(a) and InAsSb NWs with an Sb composition of (b) 3%, (c) 10%, (d) 16% and (e) 19%. The peaks in colours show the decomposed emissions.

spectra of $InAs_{1-x}Sb_x$ NWs as the Sb component increases at 10 K. Raw data is plotted in black lines. Due to atmospheric absorption, there is a distinct absorption at around 0.28 eV, and the signal close to this position is also suppressed to some extent. Therefore, the black raw data are appropriately modified. In Fig. 4.23 (a) and (b), the black curves are corrected to the magenta curve and is decomposed into turquoise and red peaks, while in Fig. 4.23 (c) (d) and (e), the black curves are corrected to the magenta curves. With the gradual increase of the Sb component, the following three obvious changes are revealed in the PL spectra: firstly, the peak position is gradually shifted to lower energy; secondly, the

peak width gradually increases; thirdly, the emission evolves from multimodal emission to unimodal emission.

For each sample with Sb content of no less than 10%, only one single peak is visible. As evidenced by previous analysis in this section, these emissions are derived from the BtB transition of InAsSb. For the other samples of non-high Sb composition (InAs NWs and $InAs_{0.97}Sb_{0.03}$ NWs), their main peaks assosiated with BtB transition are both accompanied by a lower energy and lower intensity of the emission peak. Due to the mixture of WZ/ZB phases in the $InAs_{1-x}Sb_x$ NWs, various transition mechanisms coexist, for example, impurity-related transitions or defect-related transitions, the type-II transition caused by the mixed WZ/ZB phases, and the BtB transition from the ZB $InAs_{1-x}Sb_x$. All these origins of the emmision from InAs NWs have already been identified, so it is acceptable to assign the high-energy emission and low-energy emission from the BtB transition and type-II transition, respectively. In another words, the defect- and/or impurity-related emission is too weak to see, which is considered to be correlated to the improved crystalline quality. This is also supported by the observation of PL emission from the InAs NWs at room temperature as shown in Fig. 4.24.

The energy of the BtB emission peak, E_{p}, reflects the bandgap energy E_{g} of InAsSb NWs, and the general relationship they follow can be writen as:

$$E_{\mathrm{g}} = E_{\mathrm{p}} - \frac{1}{2}k_{\mathrm{B}}T \tag{4.12}$$

where k_{B} is the Boltzmann constant, T is the temperature. It should be emphasized again that the peak energy of the sample is lower than the apparent peak centered at 0.321 eV because the absorption range of CO_2 in the atmosphere is $0.282 - 0.296$ eV. Considering this absorption, the black raw data curves in Fig. 4.23 have been properly corrected, for example, the estimated value of the peak energy of $InAs_{0.84}Sb_{0.16}$ NWs is 0.304 eV. Every corrected peak position is marked with an up arrow in Fig. 4.23.

Table 4.2: The EDX-determined Sb content and the corresponding theoretical bandgap energy for a series of InAsSb NWs with the photoluminescence BtB related emission peak energy(measured at 10 K) and the FWHM.

Measured	Results-from-photoluminescence			Theoretical
Sb content	Peak energy	FWHM	Reference	E_g
(atm.%)	(eV)	(meV)	/Souce	(eV)
0	0.427	30.0	Our work	0.417
2	0.406	45.5	Ref [69]	0.400
3	0.405	47.4	Our work	0.394
4	0.375	48.8	Ref [74]	0.384
11	0.345	66.6	Ref [74]	0.339
16	0.304	66.8	Our work	0.297
19	0.242	71.8	Our work	0.279

For all $InAs_{1-x}Sb_x$ NWs samples with different Sb components, their BtB-related energy (both the experimental values derived from PL measurements and theoritical value) and the peak shape are summarized in Table 4.2. The bandgap energy of the $InAs_{1-x}Sb_x$ alloy as a function of Sb can be expressed as a function of the component x of Sb:

$$E_g = xE_{InSb} + (1-x)E_{InAs} - Cx(1-x) \tag{4.13}$$

where x is the Sb composition, E_{InSb} and E_{InAs} are the bandgaps for InSb and InAs at 10 K, respectively, while C is the bowing parameter. In Fig. 4.23, the BtB-related emission show strong red-shifts as the composition of Sb increases, which is attributed to the bandgap shrinkage in the presence of Sb. This observable bandgap shrinkage is consistent with Equation 4.13. Here a bowing parameter of 0.67 eV is used, which is within the acceptable range of $0.66 - 0.682$ eV. As shown in Table 4.2, for $InAs_{0.81}Sb_{0.19}$ NWs, the bandgap energy derived from PL is slightly lower than the theoretical value. We

correlate this difference with the wider Sb fluctuations in NWs. When the Sb incorporation is high, the non-uniformity of the Sb distribution becomes apparent. This Sb fluctuation can constitute a slight type-II alignment, which in turn causes the type-II energy of the NWs to be lower than that of the corresponding bulk material.

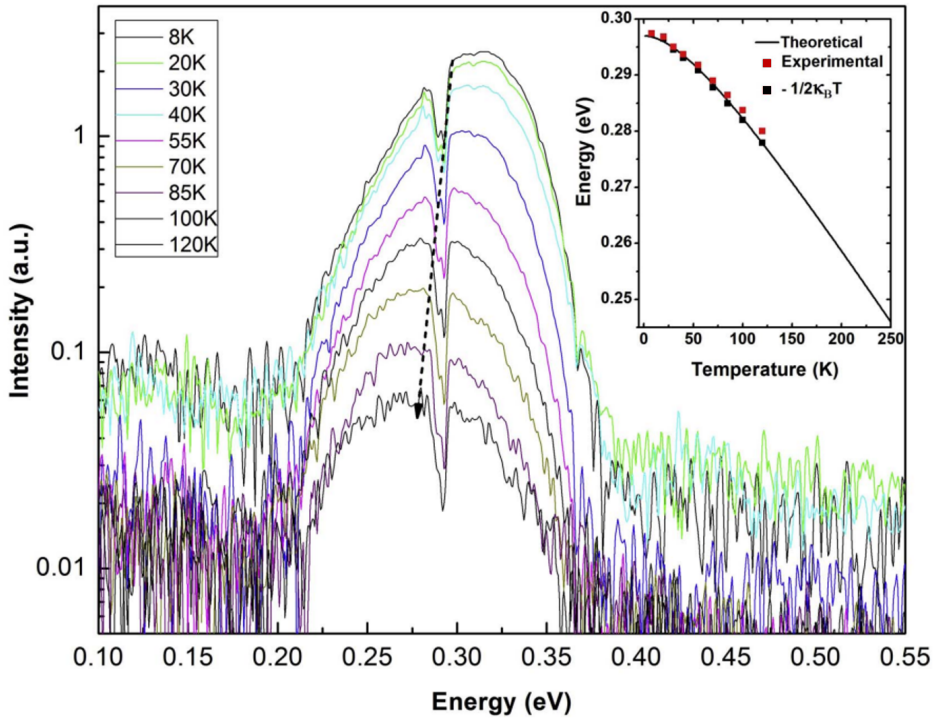

Figure 4.24: The photoluminescence of $InAs_{0.84}Sb_{0.16}$ measured at various temperatures. The inset is the peak energy E_p, the energy of $E_g - k_B T/2$ and the theoretical bandgap energy.

In the view that the high component Sb incorporation leads to the deviation of the emission energy of InAsSb NWs, temperature-sweeping PL has also been conducted for sample $InAs_{0.84}Sb_{0.16}$ NWs to further evaluate the optical properties of InAsSb NWs with high Sb content. Fig. 4.24 shows the PL spectra measured at different temperatures. The emission still exists when the temperature is up to 120 K. Not surprisingly, the emission peak shows a significant red-shift as temperature increases.

The peak energy E_p at different temperatures is depicted and shown in the inset, along

with the corrected energy using $-k_{\mathrm{B}}\ T/2$. The theoretical bandgap energy is defined as:

$$E_{\mathrm{g}}(T) = E_{\mathrm{g0}} - \frac{\alpha T^2}{\beta + T} \tag{4.14}$$

where E_{g0} is the bandgap energy at 0 K, and α and β are empirically determined parameters which is considered to have linear dependence on x. Once we use 0.297 eV as E_{g0} for $InAs_{0.84}Sb_{0.16}$ and the experimentally determined values of α and β for InAs and InSb, it can be found that the theoretical bandgap of $InAs_{0.84}Sb_{0.16}$ follows Eq. 4.12.

In summary, by carefully tuning $FR_{\mathrm{V/III}}$ and F_{Sb}, InAsSb NWs with different Sb content have been obtained. The crystalline phases and luminescence properties are clearly revealed as a function of Sb incorporation via detailed measurements and analysis (including TEM, temperature-sweeping PL, power-sweeping PL) on a series of InAsSb samples. The crystalline phases and luminescence properties are mutually reinforcing and support each other. InAsSb NWs with Sb incorporation of up to 19% have been obtained by suppressing the Sb surfactant effect, and the emission wavelength is successfully extended to 5.1 µm covering the entire MWIR band. This study opens the way to fabricate next-generation devices using InAsSb NWs , such as highly sensitive silicon-based room-temperature infrared photodetectors operating in MWIR and LWIR, by combining the advantages of III-V semiconductors.

4.4 InAs-AlSb core-shell NWs

In the previous section, InAsSb NWs have been realized via MBE showing excellent optical emission covering the range of $0.25 - 0.415$ eV. There are very few reports of core-shell NWs involving InAs which is one of the most important narrow bandgap optoelectronic materials. InAs has a very high mobility (8×10^5 $\mathrm{cm^2V^{-1}s^{-1}}$ at 4.2 K),

its combination with III-antimonides gives a small lattice mismatch (about 0.66% for InAs/GaSb and 1.18% for InAs/AlSb) with a large conduction-band offset ($\sim$ 1.12 eV for InAs/GaSb and $\sim$ 1.35 eV for InAs/AlSb), which produces excellent electron confinement. Together with its type-II bandgap alignment, InAs/antimonide heterostructures are thus promising candidates for high-speed and high-performance electronic/optoelectronics devices operating in the mid wavelength infrared spectral range [65]. In this section, we report the realization of InAs-AlSb core-shell NWs grown on Si (111) substrate by MBE and their device application in photodetection as mentioned in the publication [30]. The resulting InAs-AlSb core-shell NWs are dislocation-free and have superior PL properties as compared to simple InAs NWs. This phototransistor based on individual InAs-AlSb core-shell NW is promissing for significantly improved infrared photodetection by dramatically reducing dark current and enhancing anomalous photocurrent.

The core-shell NWs materials were grown on Si (111) by droplet assisted MBE. InAs NWs growth at preoptimized growth conditions, *e.g.*, at a growth temperature in the range of $420 - 470$ °C, $F_{\mathrm{V/III}}$ of $30 - 100$, and an InAs nominal growth rate of 0.1 µmh^{-1}. The InAs NWs growth lasted for 2 h and was followed by 1-h deposition of AlSb shells at reduced growth temperature and a low growth rate.

NW growth is clearly visible in the SEM images as illustrated in Fig. 4.25 (a) (b) for the top and 30°-tilted view, respectively. It can be seen that the NWs exhibit a uniform diameter along their entire length. The density of the NWs is $13.3 \pm 1 \times 10^8 \mathrm{cm}^{-2}$. Analysis over the whole sample gave an average NW length of 2.1 ± 1 µm and an average diameter of 48 ± 11 nm as shown in Fig. 4.25 (c) (d). The SEM images also reveal many ($\sim$ 80%) bent and some ($\sim$ 20%) straight NWs. This is very different from bare InAs NWs and InAsSb NWs which are 100% vertically oriented (see Fig. 4.1 and Fig. 4.8). The bent NWs have no preferential direction so it cannot be related to shadowing effect in NW growth. We believe this high percentage of bent NWs is caused by an asymmetric stress on the NWs induced by a nonuniform thickness of the AlSb shell layer around the InAs core.

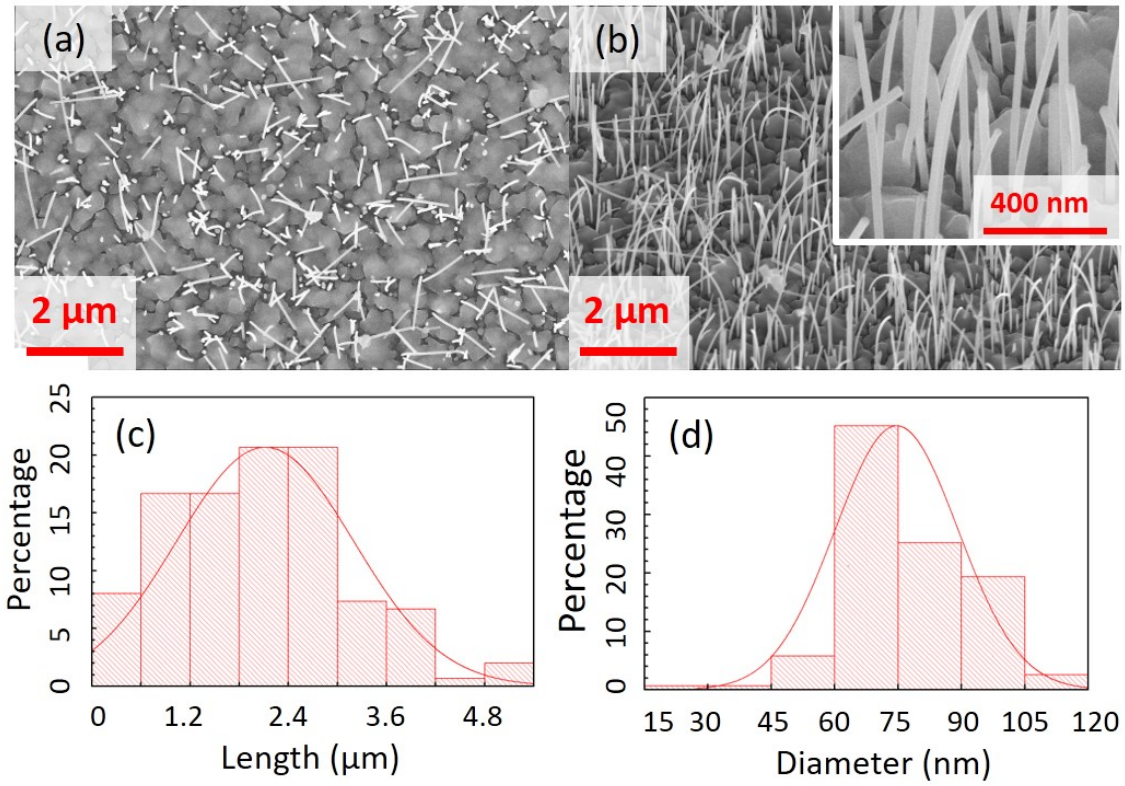

Figure 4.25: SEM images for the InAs-AlSb core-shell NWs specified from (a) top view, and (b) tilted view, showing majority of the NWs bend. The statistical diagrams on (a) length and (b) diameter for the NWs.

The realization of the core-shell NW heterostructure was further confirmed by TEM and EDX analysis. Fig. 4.26 (a) & (b) show low-resolution TEM images of a typically bent and straight NW, respectively. Both NWs have an diameter of about $30-40$ nm. The vertically oriented NWs have a uniform shell thickness (< 10 nm) as shown in Fig. 4.26 (2b-I). Conversely, the bent NW an asymmetric shell (Fig. 4.26 (2a-I)), *i.e.*, the AlSb shell thickness is uneven around the InAs core. This asymmetric shell thickness exerts a nonuniform stress on the core. In this InAs-AlSb core-shell structure, the core is in tensile strain of $\sim 1.2\%$ with respect to the AlSb shell. Although this strain is small, a nonuniform stress on an NW is still capable to bend the NW due to the large NW length and the thin diameter. Detailed structural information of the core-shell NWs was obtained using annular dark field (ADF) and bright field (BF) STEM. Fig. 4.26 (2c) shows a <110>

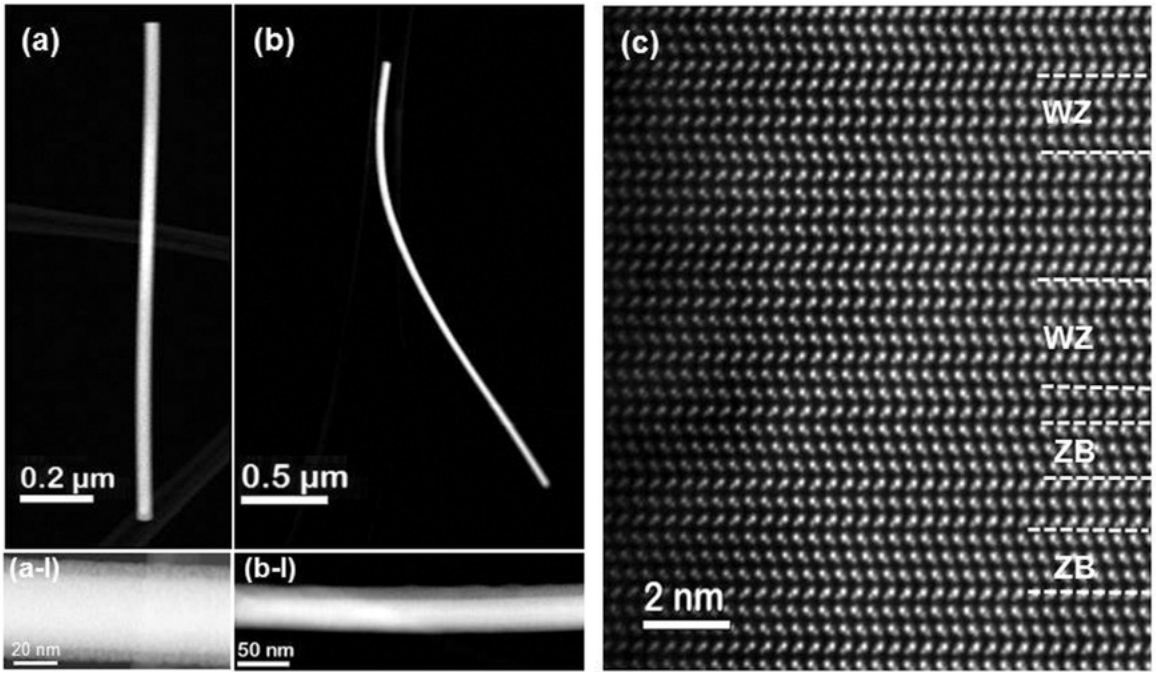

Figure 4.26: TEM images for the InAs-AlSb core-shell NWs specified as (a) Low-magnification ADF-STEM images from a straight NW, and (b) a bent NW. (a-I) is a higher magnification STEM image of the straight NW showing core-shell structure with uniform shell thickness. (b-I) shows a bent NW with an asymmetric AlSb shell. (c) High magnification annular dark-field image of the shell/core interface showing a mixture of WZ and ZB phases.

zone axis ADF-STEM image of the shell/core interface. The growth direction is vertical. Alternating WZ and ZB phases are clearly visible. The fraction of WZ phase was found to be $\sim 50\%$, calculated by analyzing multiple NWs (following the metrics proposed by Caroff *et al.*, that a segment must contain at least three or four monolayers of a given stacking sequence to be considered as a specific crystal phase for ZB or WZ, respectively). Many rotational TPs were also observed. These observations are typical for InAs NWs. Thus, electron microscopy analysis demonstrates high quality InAs-AlSb core-shell NWs accommodating strain without generation of dislocations. It should be noted that the lack of interfacial misfit dislocations along the InAs/AlSb interface has also been observed in other epitaxial NW systems.

The core-shell structure in the NW is further confirmed by elemental analysis. An EDX composition profile across a straight NW, along a line perpendicular to the growth

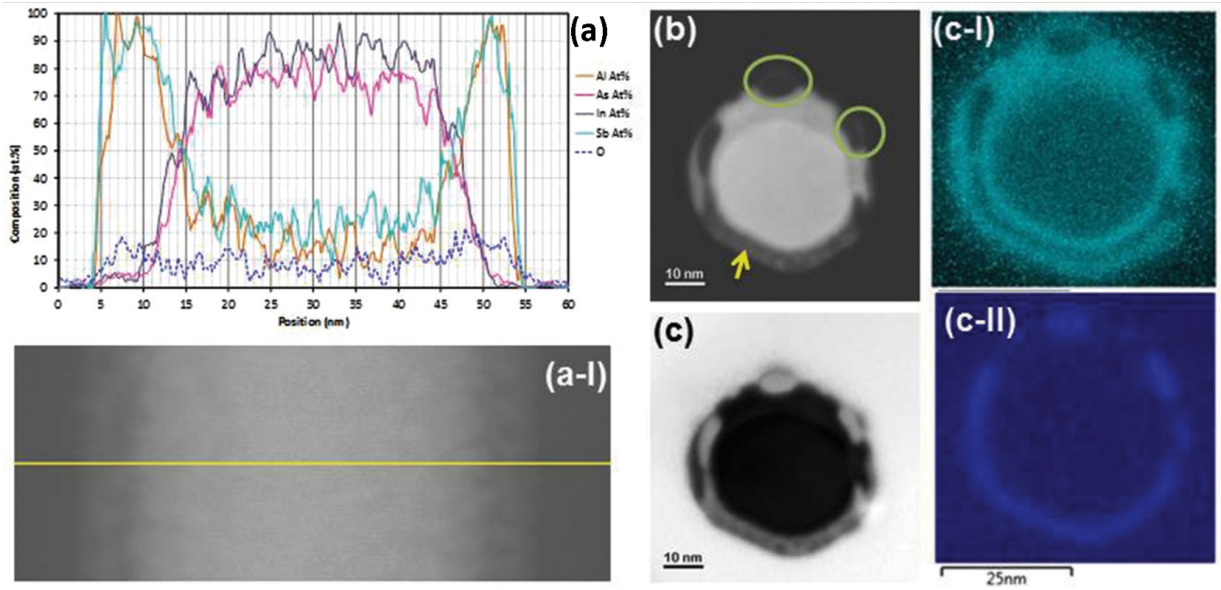

Figure 4.27: EDX analysis for the InAs-AlSb core-shell NWs. (a) The composition profile of In, As, Al, Sb, and O element profile across a quasi-straight core-shell NW, (a-I) shows the measurement path across the NW. (b) Top view ADF TEM image and (c) BF TEM image of a quasi-straight core-shell NW. The green ellipses in (b) indicate the areas are rich in Al and O; the yellow arrow indicates the area consists of a region rich in Al and O between two Sb rich bands. (c-I) and (c-II) for the Sb and O distribution profile across a core-shell NW.

direction, is shown in Fig. 4.27 (a). A core-shell structure is clearly visible in the line plot of composition (normalized to 100 atm.%). Fig. 4.27 (b) & (c) show the top view ADF and BF TEM images of a quasi-straight NW, respectively. The core-shell NW contains with six <110> facets, which is quite different with InAs/GaSb case that multiple side facets dominate during the growth process. It should be noted that oxygen is observed in the shell layer. The dark/bright contrast in the ADF and BF images implies the compositional changes in the shell of the NW due to the oxidation of AlSb shell layer. These oxygen rich regions are very likely due to the high affinity of AlSb for oxygen that makes it highly susceptible to oxidation. It is worth noting that the oxidation of the shell layer is not uniform. Two types of oxidization areas can be observed. (i) Vertexes of the hexagonal prism rich in Al and O, indicated by the green ellipses in Fig. 4.27 (b); (ii) Al and O rich region between two rich Sb bands, indicated by the yellow arrow in Fig. 4.27 (b). Fig. 4.27 (c-I) & (c-II) correspond to Sb and O elemental map distributions, respectively.

The O rich region around the vertexes are clearly observed Fig. 4.27 (c-I), and the O rich band sandwiched between two thin Sb rich bands Fig. 4.27 (c-II). The vertexes region has large area exposed to oxygen, it is understandable it is more readily to be oxidized; however, the reason for the formation of the Al and O rich band in the shell layer is unclear. It should be noted that this oxidation in the AlSb shell layer might contribute to the bending of the NWs. However, as the bending is generally observed in the NWs with nonuniform shell thickness; we believe the major cause for the bending is the stress induced by the nonuniform coating of the shell layer.

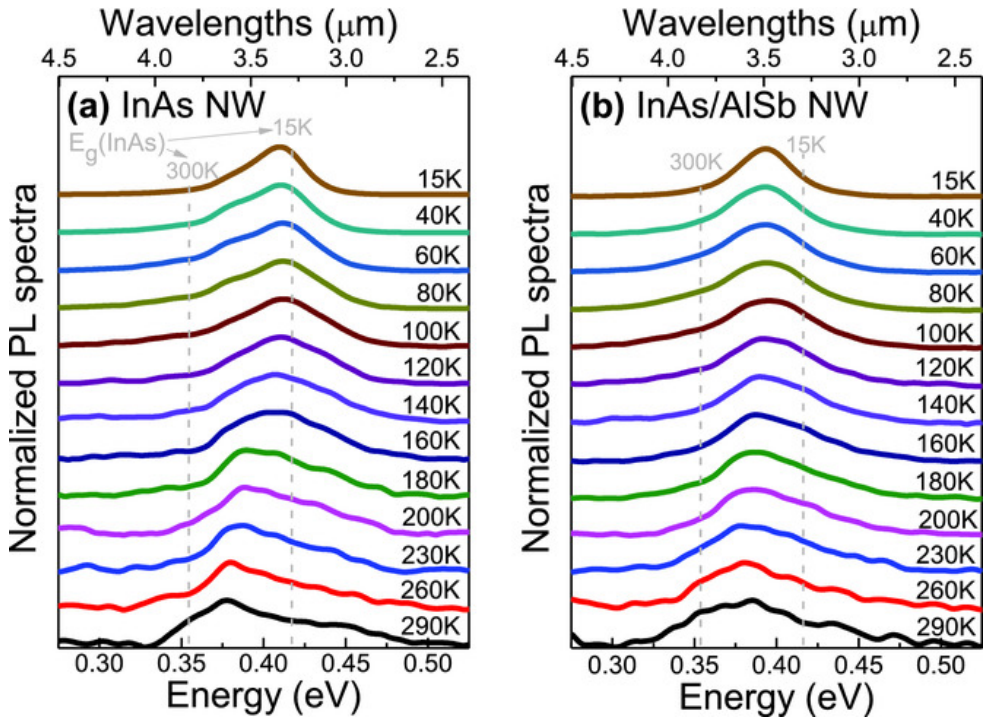

Figure 4.28: Normalized PL spectra for InAs (a) and InAs-AlSb (b) NWs obtained at different temperatures. The excitation power was 10 mW and the diameter of laser spot was 1 mm. Vertical dashed gray lines are located at energies corresponding to InAs bandgap at 15 K and 300 K.

It is well accepted that NWs surface states play a key role in their optical and electrical properties due to the large surface-to-volume ratio. Consequently, surface passivation is generally required to improve the performance of nanowire-based devices. Amongst various surface passivation approaches, the core-shell nanostructures have appeared to be the

most efficient due to the availability of perfect interface, efficient quantum confinement, and free contamination. In order to elucidate the optical properties of these core-shell NW ensembles, PL measurements were performed on the samples of InAs NWs and InAs-AlSb core-shell NWs at various temperatures and excitation powers, and on different positions of the samples. Temperature-dependent PL spectra of InAs NWs and InAs-AlSb core-shell NWs are shown in Fig. 4.28 (a)&(b), respectively. At 15 K both samples demonstrate a very strong PL signal; however, the peak energy is below the free exciton transition energy in bulk InAs at low temperatures ($\sim$ 0.415eV). The InAs NWs show an asymmetric PL band with a dominant peak centered at (0.410eV) and an extra peak at the low energy side ($\sim$ 0.380eV), while the InAs-AlSb NWs exhibit a quite symmetric PL band with a peak position at (0.391eV). We believe the dominant emission originates from BtB transition while the redshift is related to the band bending in the core InAs. With increase of temperature, the emission peak is redshifted due to bandgap shrinkage. More importantly, the PL emission persists up to room temperature. In order to evaluate the emission efficiency, we directly compare the PL spectra at four selected temperatures for the two samples as depicted in Fig. 4.29 (a)-(d). It shows that the PL intensity is slightly stronger for InAs NWs at 15 K, while the emission of InAs-AlSb core-shell NWs is getting stronger with further increase in temperature. This behaviour is further illustrated in Fig. 4.29 (e) which gives a direct comparison of the integrated intensity of PL signal for the two samples in the whole temperature range. It should be noted that assessing optical quality through this direct comparison of PL intensity for NWs could be controversial due to several factors such as different density and/or different absorption coefficients of different NWs.

Consequently, we introduce internal quantum efficiency (IQE) to evaluate the emission efficiency in NWs. We define IQE as the ratio of PL intensity obtained at a given temperature to the integrated PL intensity at 15 K which the IQE is assumed to be 100%. In general a nonradiative recombination can be present for the two samples even at 15 K,

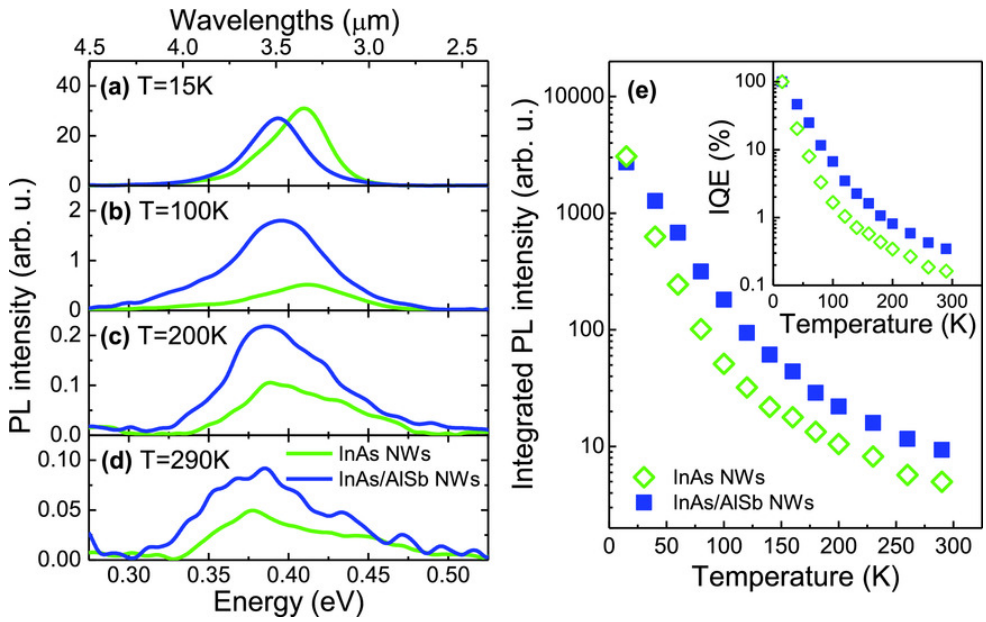

Figure 4.29: Normalized PL spectra for (a) InAs and (b) InAs-AlSb NWs obtained at different temperatures. The excitation power was 10 mW and the diameter of laser spot was ∼ 1mm. Vertical dashed gray lines are located at energies corresponding to InAs bandgap at 15 K and 300 K.

but its contribution to the recombination process is rather small and comparable at this temperature since the absolute PL intensities are very similar at 15 K. Therefore the IQE defined in this way is an appropriate parameter for comparison of the optical quality of the studied NWs and this parameter is better for the analysis than the absolute PL intensity even if the IQE is not exactly 100% at 15 K.

As depicted in the inset in Fig. 4.29 (e), the IQE of the InAs-AlSb core-shell NWs is about two times stronger than that of InAs NWs at room temperature. This implies that the AlSb shell layer enhances the PL emission, which is attributed to surface passivation and quantum confinement induced by the AlSb shell layer. A similar behaviour was observed for the measurements performed at other different positions on each sample. It should be noted that, up to date, room temperature PL from InAs NWs has not been widely reported due to the two major issues related to stacking defects in NWs and the surface states of NWs as well as the possible electric field built between NWs and silicon

substrate. The observation of room temperature PL from InAs and InAs-AlSb core-shell NWs indicates that the mechanism of thermal quenching of PL in our NWs has been significantly suppressed. The large diameters of InAs NWs and optimized growth conditions improved the crystalline quality of the InAs NWs. Furthermore, the use of AlSb shell provides efficient surface passivation and quantum confinement which both improve the emission efficiency.

It should be noted that blueshift of peak energy induced by size-related quantum confinement (see Sec. 1.8.2) is not observed in these NWs. This is due to the much larger diameter ($\sim$ 75 nm) of our NWs compared with the diameter of NWs ($<$ 25 nm) which gives significant blueshift. On the contrary, these InAs NWs demonstrate PL emission with a lower energy than that of InAs. Although type-II bandgap alignment induced by mixture phases in InAs NWs could result in PL emission at lower energy, we have also demonstrated that the NWs obtained at optimal growth conditions possess a high quality with small phase segments hence the type-II alignment effect is negligible. This in turn leads to BtB transition PL emission. At the conditions used for our PL measurement, we assume that the dominant emission is related to BtB emission for both InAs NWs and InAs-AlSb core-shell NWs in the whole temperature range, and the redshift of the peak energy is most likely associated with the band bending in the InAs NWs and additional effect of band alignment for InAs-AlSb core-shell NWs.

The as-grown InAs is n-type due to native defects/impurities so the Fermi level inside InAs locates close to the conduction band and there is strong Fermi level pinning effect at InAs surface above the conduction band leading to a surface electron accumulation layer. The Fermi level position at AlSb surface has not been explored but it is rather expected that the Fermi level at AlSb surface is pinned in the middle of bandgap for a stabilization energy, *e.g.*, located at $\sim$ 0.8eV below the conduction band (for InAs the Fermi level stabilization energy is located at $\sim$ 0.2eV above the conduction band). The band bending in InAs and InAs-AlSb NW is sketched in Fig. 4.30, with a type-II

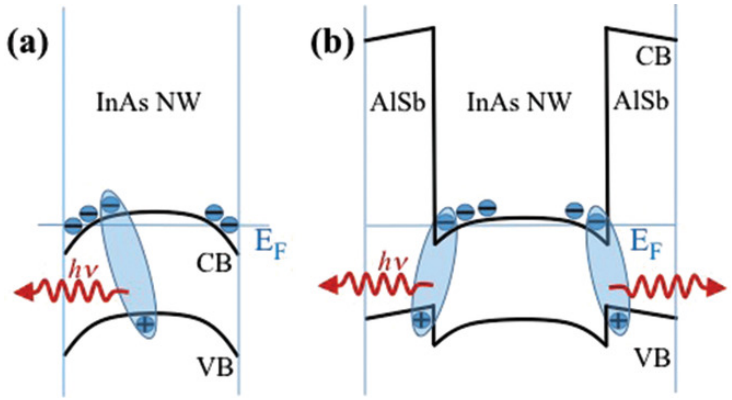

Figure 4.30: Sketch of band bending in InAs a) and InAs-AlSb b) NWs. N-type character of InAs material is assumed.

bandgap alignment for InAs-AlSb interface and a valence band offset of 0.18 eV. It can be seen that for InAs NWs, the holes are depleted from the surface by a potential barrier. Due to the large band bending, the energy of BtB recombination in such NWs can be smaller than InAs bandgap (*e.g.*, Stark effect). For the sample of InAs-AlSb core-shell NWs, there is a type-II band alignment, which separates the holes and electrons, *e.g.*, the holes trapped in the AlSb region while the electrons remain in the InAs core region. This separation results in a reduced transition energy. Such band bending and type-II alignment can also affect emission efficiency. For InAs NWs the photoexcited electron–hole pair can recombine radiatively since the photoexcited hole is separated from the surface and n-type carriers (electrons) could occupy surface states to suppress nonradiative recombination via surface states. For InAs-AlSb NWs the photoexcited electron–hole pair are effectively separated, *e.g.*, holes trapped in the AlSb region while the electrons remain in the InAs core region. The insertion of shell layer will suppress the effect of surface states on the radiative recombination, consequently leads to a more efficient radiative emission. In addition, this carrier separation would increase the free-path of the photo-generated carriers in the NW under external bias, as a result, would favor device applications of InAs-AlSb core-shell NWs in terms of photoconductive photodetectors and photovoltaic devices. It is worth noting that the oxidation of the AlSb might have contribution to

the enhanced PL emission due to its wide bandgap energy which helps to remain the photo-generated electrons in the core region.

4.5 InAs-InGaAs core-shell NWs

InAs stem was firstly grown on Si substrate via previous droplet-assisted MBE technique for 1 hour. The temperature of substrate was set at 445 °C The nominal growth rate of In was 0.1 ML/s, which BEP was measured as 7.2×10^{-7} mBar, while the BEP of As_4 was set at around 3×10^{-5} mBar, which gave a V/III ratio of 42. For the InGaAs shell, the temperature of substrate remained at 445 °C. Ga, In and As were opened simultaneously for the growth of InGaAs shell. The nominal growth rate of In was reduced to 0.05 ML/s, and the nominal rate of Ga was set at 0.1 ML/s for the entire stage of shell growth. The total V/III ratio increased to 61, while the ratio of As_4/Ga and As_4/In were 176 and 83, respectively.

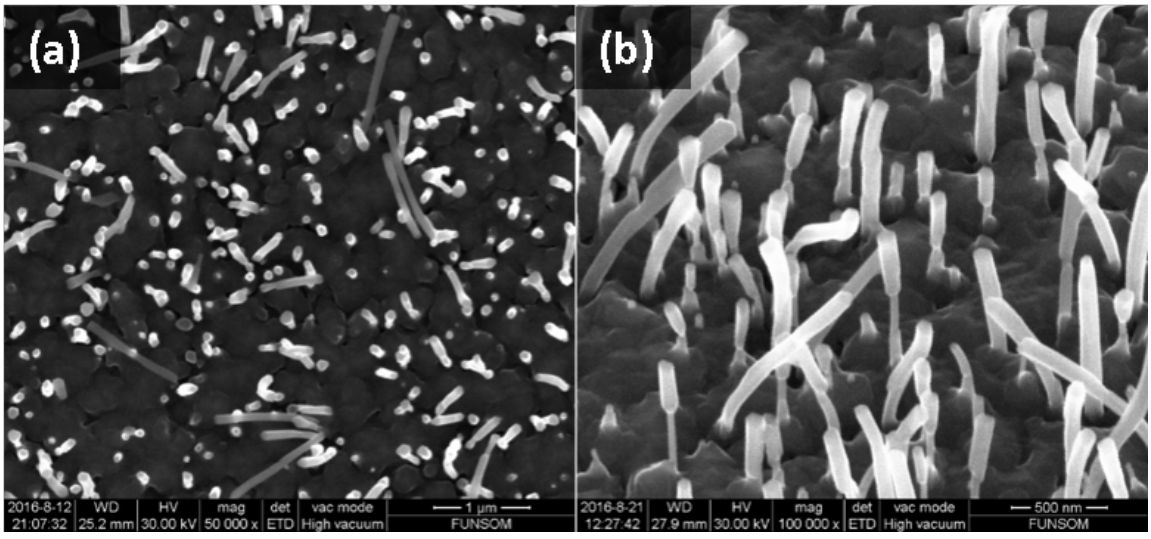

Figure 4.31: SEM images for sample A932 InAs-InGaAs core-shell NWs.

SEM images were taken as Fig. 4.31 from both top view Fig. 4.31 (a) and 30°-tilted view Fig. 4.31 (b) for the samples, and basic statistics have been done based on the two

SEM images. The NWs distributes randomly on the substrate with a density of 9.2×10^8 cm^{-2}. Only less than half of them are standing straight, meanwhile more than half of them bend in varying degrees. In the image of tilted sample, the core-shell NWs exhibit as different structures: (a) most of them are core-shell structures entirely coated with InGaAs alloy, (b) some of them are dumbbell-like structure partially coated with InGaAs alloy, and (c) very less part of them have structure with top-side coating.

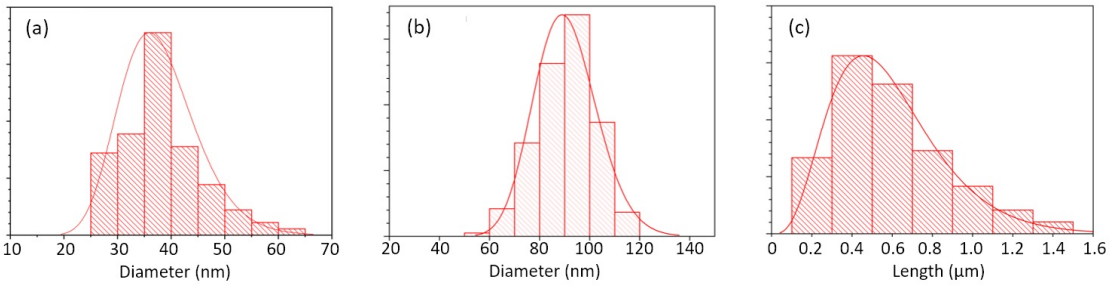

Figure 4.32: Morphology statistics for sample A932 InAs-InGaAs core-shell NWs.

Statistics have been done based on the above SEM images. The core NWs has relative uniform diameter varying from 26 nm to 63 nm, with an average value of 38 ± 8 nm. The distribution is quite concentrated but a bit asymmetric as shown in Fig. 4.32 (a). According to our conclusion for pure InAs NWs presented in Sec. 4.1, the Sb-free core growth should result in a uniform diameter and relative symmetric distribution, meanwhile a small tail would exist in the direction to large diameters. The shell diameter is intensively increased comparing to the core NWs, varying from 55 to 115 nm with a mean value of 91 ± 12 nm. The relative standard deviation (RSD) falls from 21% (8÷38) of pure core NWs to 13% (12÷91) of shell NWs. The histogram of Fig. 4.32 (b) has a more symmetric and concentrated distribution which shows this intuitively. After the shell growth, the NWs has large vary length from 0.1 μm to 1.5 μm with a average length of 0.58 ± 0.15μm. The histogram of Fig. 4.32 (c) presents a very asymmetric distribution with a long tail in the direction to large lengths, and its RSD reaches 0.15÷0.59=25%. The nonuniformity of the length might be due to both the core growth and the shell growth. To reveal the

detailed structure of the NWs, HRTEM has been done on the core-shell structures.

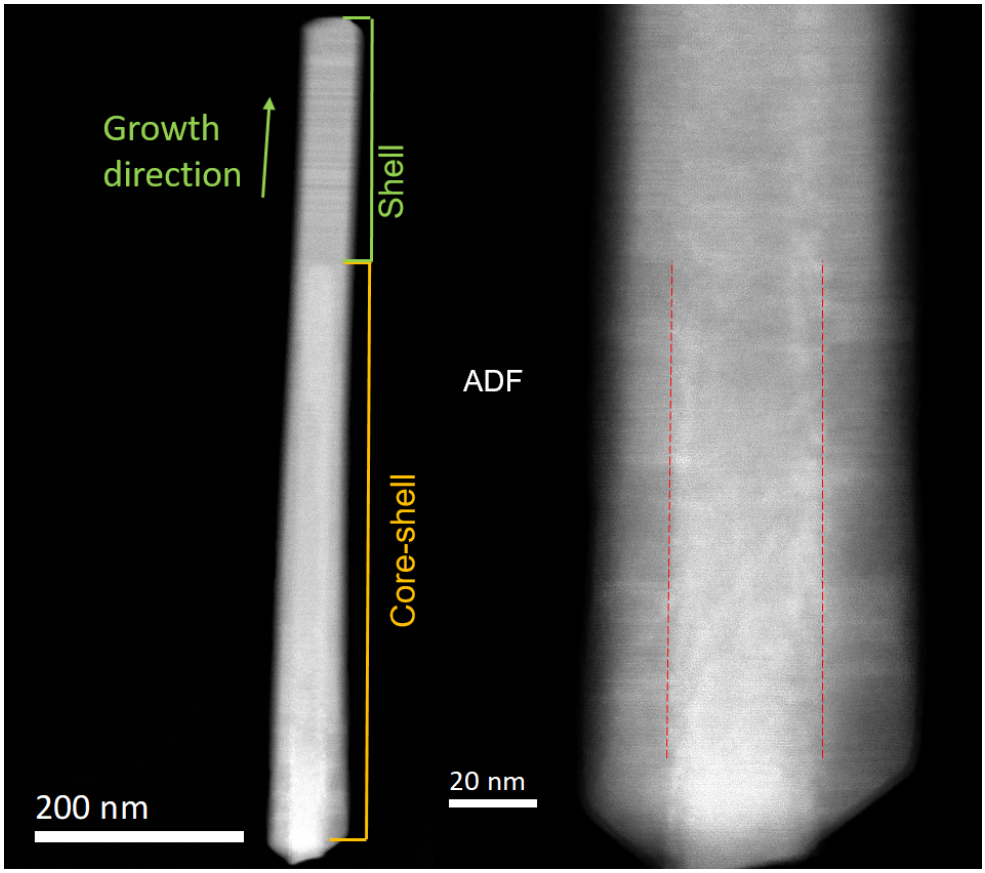

Figure 4.33: Annular dark field TEM images of a InAs-InGaAs core-shell NW.

Annular dark field TEM images of a InAs-InGaAs core-shell nanowire was shown in Fig. 4.33 (A932-TEM-1). The contrast in Fig. 4.33 (a) indicates that approximately 30% of the nanowire length in the top region is just shell, which is also confirmed by EDX images. Additionally the bright contrast at the core-shell interface parallel to the red dashed lines indicates the formation of misfit dislocations, which will also be demonstrated in subsequent TEM images. The core NW has very uniform and thin diameter of 33.2 ± 0.6 nm along the growth direction. According to the calculation in Sec. 1.8.2, such thin diameter would cause significant quantum confinement effects.

The InGaAs shell has preferential growth in the bottom region than the top region, whose thickness are 14 nm and 23 nm (18 nm in average), respectively. So the NW of

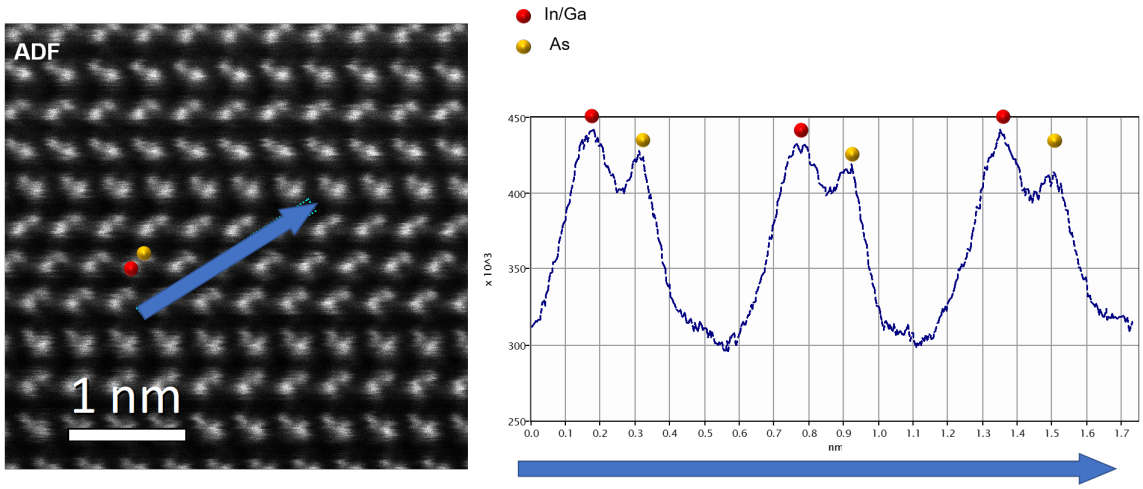

Figure 4.34: ADF-HRTEM images of the axial shell part of the individual InAs-InGaAs core-shell NW.

core-shell has a diameter of 78 ± 4 nm at bottom region which reduces to 61 ± 4 nm at the top of core-shell part. This difference indicates that the shell growth represents a preference in the bottom region than the top region. The possible reason might be related to the atomic migration.

The top part, which is InGaAs alloy, has a quite uniform diameter of 58 ± 4 nm. Similar to the 1-D growth of GaAs NWs in VLS mode, the 1-D growth of InGaAs also results in very uniform diameter. Two kind of mechanisms exist in one NW at the same time during the growth of InGaAs alloy: the 2-D growth for radial shell and the 1-D growth for the top axial part. The different growth mechanisms result in very large difference in their growth rate: the top axial shell has length of 256 nm, whose growth rate is 14 times of the growth rate of the radial shell, assuming that the top part and the shell start growing at the same time.

Intensity profiles along the dumbbells in the growth direction were taken in HRADF images. The profile shape indicates that the NWs growth along the [111]B direction. As can be measured in Fig. 4.34 (b), the lattice constant for this part is approximate 0.595 nm, which is close to the lattice constant of InAs (0.6058 nm) and much larger than the lattice constant of GaAs (0.565 nm). From this lattice constant, we estimated the top part of

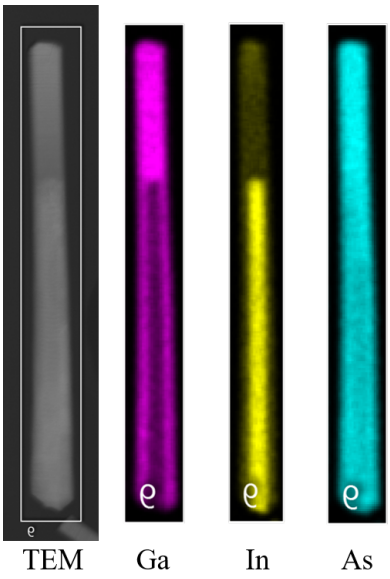

Figure 4.35: EDX mapping images of an individual InAs-InGaAs core-shell NW.

InGaAs has a Ga component of 24.5%. In other words, the top InGaAs is In-rich, which is opposite to the bottom InGaAs shell.

To confirm the hetero-structure and the distribution of elements, compositional analysis was carried out on this individual NW using EDX maps in STEM shown in Fig. 4.35. As can be observed, the InGaAs shell continues after covering the whole InAs NW, forming the top shell InGaAs alloy part. As distributes uniformly along the whole NW. Ga exists in both the radial shell alloy and axial shell alloy, and the intensity has no big difference in spite of the thickness of the two shell parts. The core has very bright yellow colour indicating the In component although it was rapped with the alloy shell, while both the radial shell alloy and axial shell alloy contain fewer In composition in comparison with the core part. Furthermore, the brightness of yellow is much lower than azaleine in shell alloy, indicating that In may have much lower incorporation than Ga under this growth condition, in spite of the different nominal growth rate of In and Ga.

To investigate quantitatively the composition of In and Ga in the shell, line-scanning EDX was used at the core-shell section of this individual NW as shown in Fig. 4.36. This

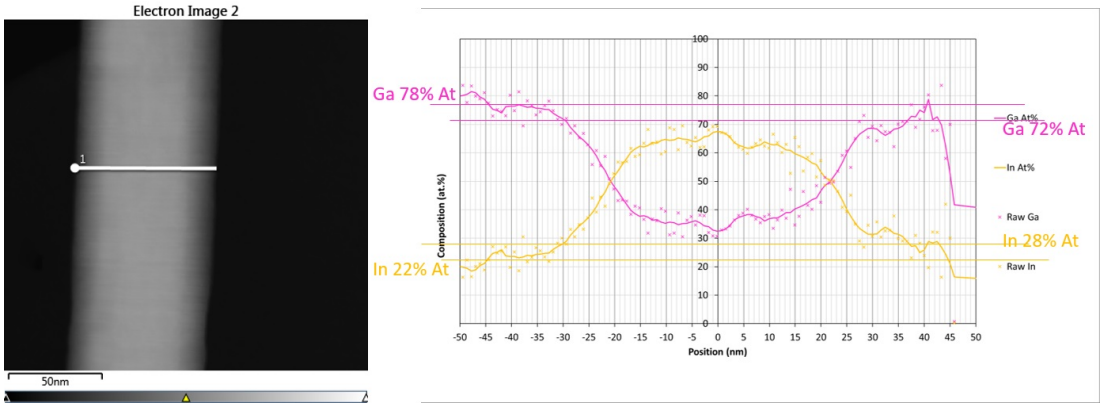

Figure 4.36: Line-scanning EDX images of an individual InAs-InGaAs core-shell NW.

EDX measurement was conducted perpendicular to growth direction in the core-shell section. The profile also confirmed the presence of a core-shell structure. The thickness of the shell is around 20 nm. Considering the thickness of shell is only about $14 - 23$ nm, the EDX data on both sides represented the composition of only the shell part. The composition of In and Ga could be obtained as around 25% and 75%, respectively, whose ratio is approximate 1:3. The nominal growth rate of In and Ga was set at 0.05 ML/s and 0.10 ML/s, respectively, and their ratio is around 1:2. The difference between the two ratios confirms that In have lower incorporation than Ga under this growth condition

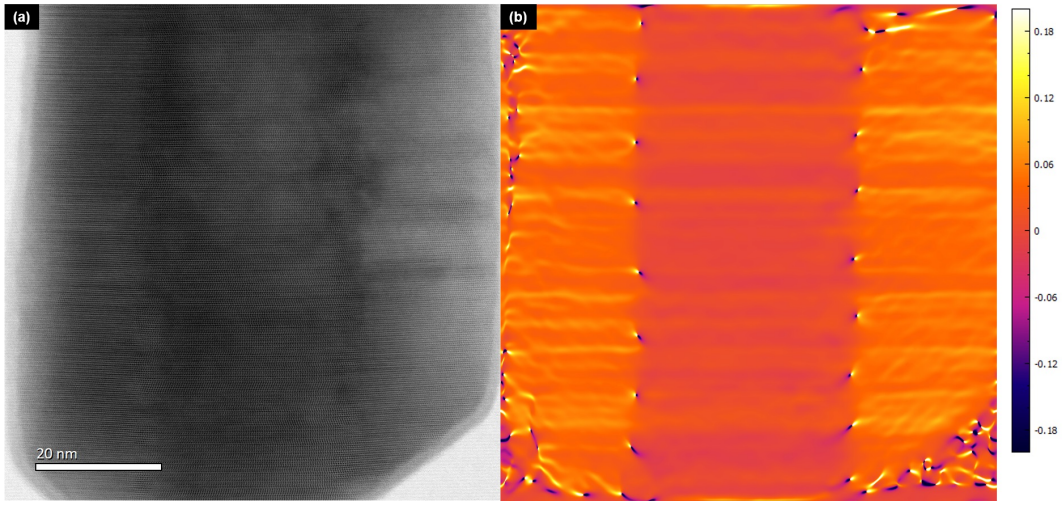

Figure 4.37: ADF-HRTEM image and analysis of the core-shell interface of the individual InAs-InGaAs core-shell NW.

during the shell growth.

Fig. 4.37 is the annular dark field image of the InAs-InGaAs hetoro-structure containing dislocations in the region of interface caused by the lattice mismatch of $\sim 7\%$ between InAs and GaAs. The ADF image has also been analyzed using the geometric phase algorithm, which reveals the strain in the areas corresponding to the misfit dislocations.

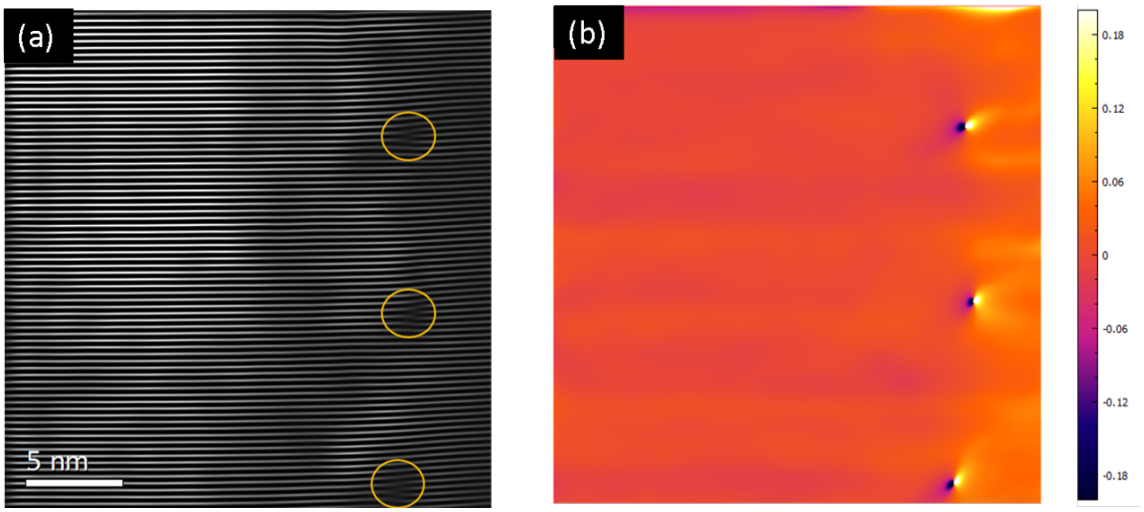

Figure 4.38: ADF-HRTEM image and analysis of the right side core-shell interface of the individual InAs-InGaAs core-shell NW.

Focusing on the right side interface, the ADF image and related analysis has been done in Fig. 4.37. The inverse fourier transform using the <111> planes parallel to the growth surface points clearly the extra planes at the InAs-InGaAs interface. Corresponding to the analysis of the ADF image using the geometric phase algorithm, Fig. 4.38 (c) and d reveals the strain in the areas corresponding to the misfit dislocations.

Photoluminescence was done at defferent temperature and under varying laser exciting power. Fig. 4.39 shows the PL spectra of InAs-InGaAs core-shell NWs, pure InAs NWs, and InAs epi-layer grown in our system. All of them have a small peak at about 0.375 eV, which is identified impurity-related peak. The epi-layer has narrow and nearly symmetric PL profile with a peak centre at around 0.41278 eV, indicating high crystaline quality. The pure InAs NWs has much broad and multi peaks with a main peak setting

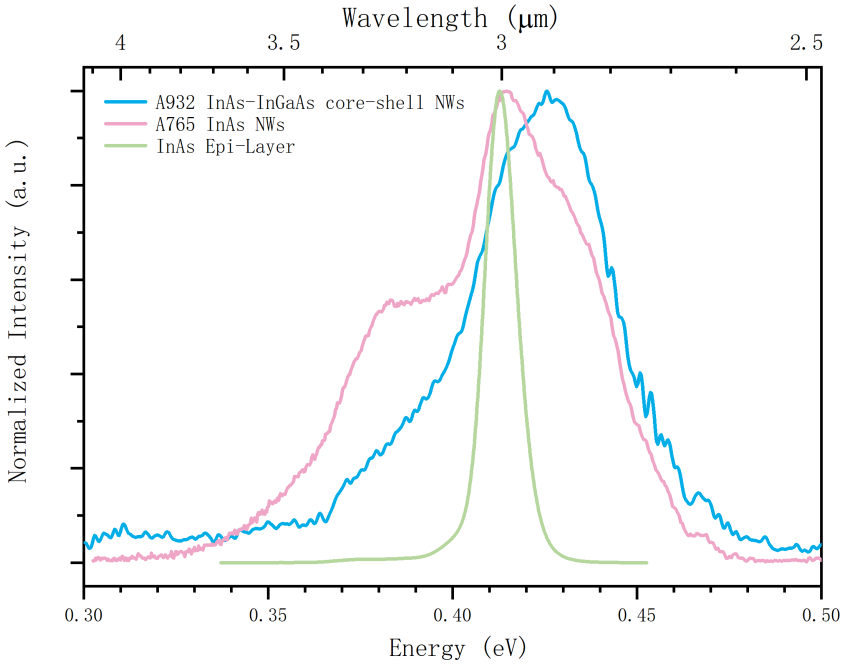

Figure 4.39: Photoluminescence spectra of InAs-InGaAs core-shell NWs with references of pure InAs NWs and InAs epi-layer.

at 0.415 eV. The spectrum of InAs-InGaAs core-shell NWs has a main peak with higher energy at 0.426 eV. Morever one shoulder at 0.435 eV and the impurity-related peak are suppressed comparing to the pure InAs NWs. To investigate the physical mechanism, the spectra are decomposed into two peaks: low energy feature (LEF) and high energy feature (HEF). LEF is the peak from impurity. It's also worth noting that there might be considerable atmosphere-related absorbtion in the region of $0.413 - 0.43$ eV in our measurement.

Fig. 4.39 illustrates representative PL spectra in an temperature range of 5–80 K. Fig. 4.39 (a) shows the decomposed peaks named as LEF and HEF. As expected, the LEF doesn't change peak position with temperature. Features of all peaks are summarized in Fig. 4.39 (b)-(d). As the green curve shows in Fig. 4.39 (b), the HEF energy of 0.425 eV is higher than ZB InAs, indicating it is from WZ BtB transition. It is expected to fall as temperature increases following Vashnis' equation. But the HEF doesn't show a clear

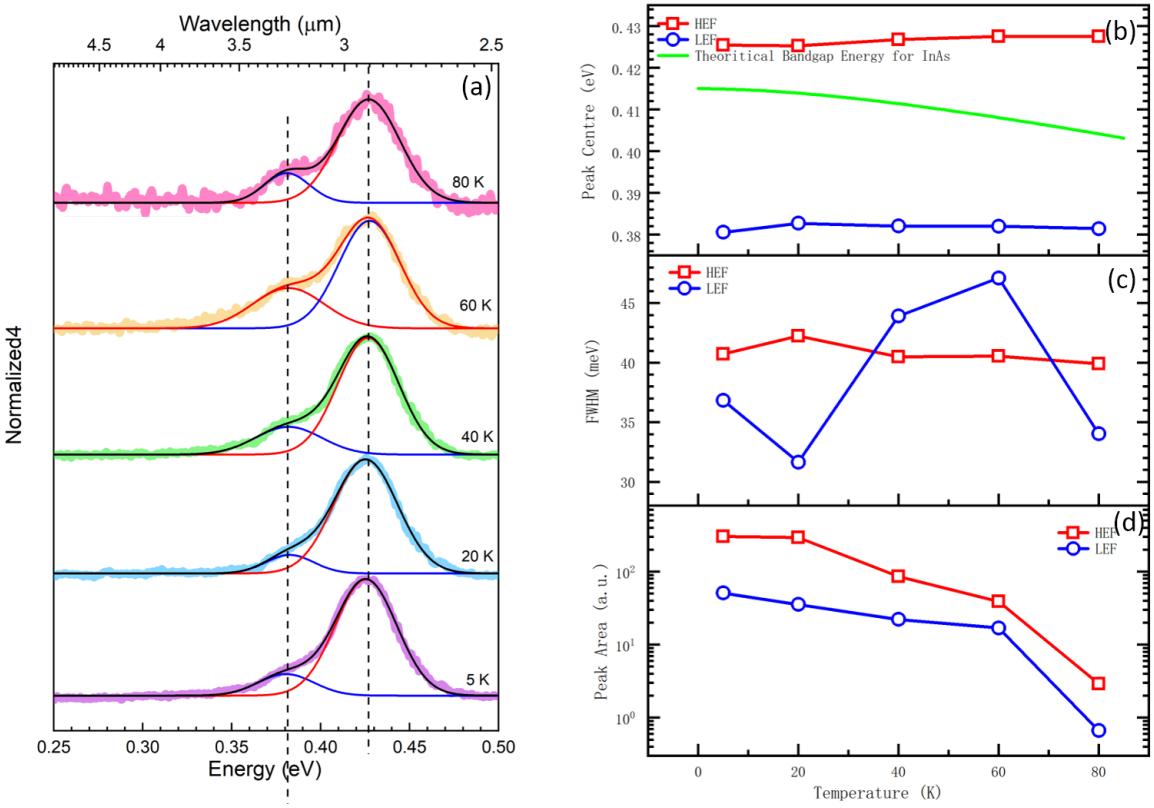

Figure 4.40: Photoluminescence spectra of InAs-InGaAs core-shell NWs at different temperature.

decrease as temperature rises. We regard this unconventional performance as related to the band filling of the carriers. Actually both the FWHM and peak position for HEF are very stable in this temperature range. It is easy to understand that peak areas for both LEF and HEF decerase quickly as temperature increases shown in Fig. 4.39 (d).

Fig. 4.40 was plotted to reveal the power dependence of the PL spectra. Fig. 4.40 (a) illustrates representative PL spectra in an excitation power range of 2–32 mW for InAs-InGaAs NWs. The HEF energy of 0.425 eV is higher than ZB InAs, indicating it is from WZ BtB shows blueshift as laser power increases, while LEF remains stable. Noting that the FWHM of HEF in Fig. 4.40 (c) has also rised, we preliminarily attribute this blue shift to the band filling induced by photo-induced carriers. The LEF also has a large peak width under higher excitation power, which means additional carrier generated under

higher excitation power would also contribute to the impurity energy levels.

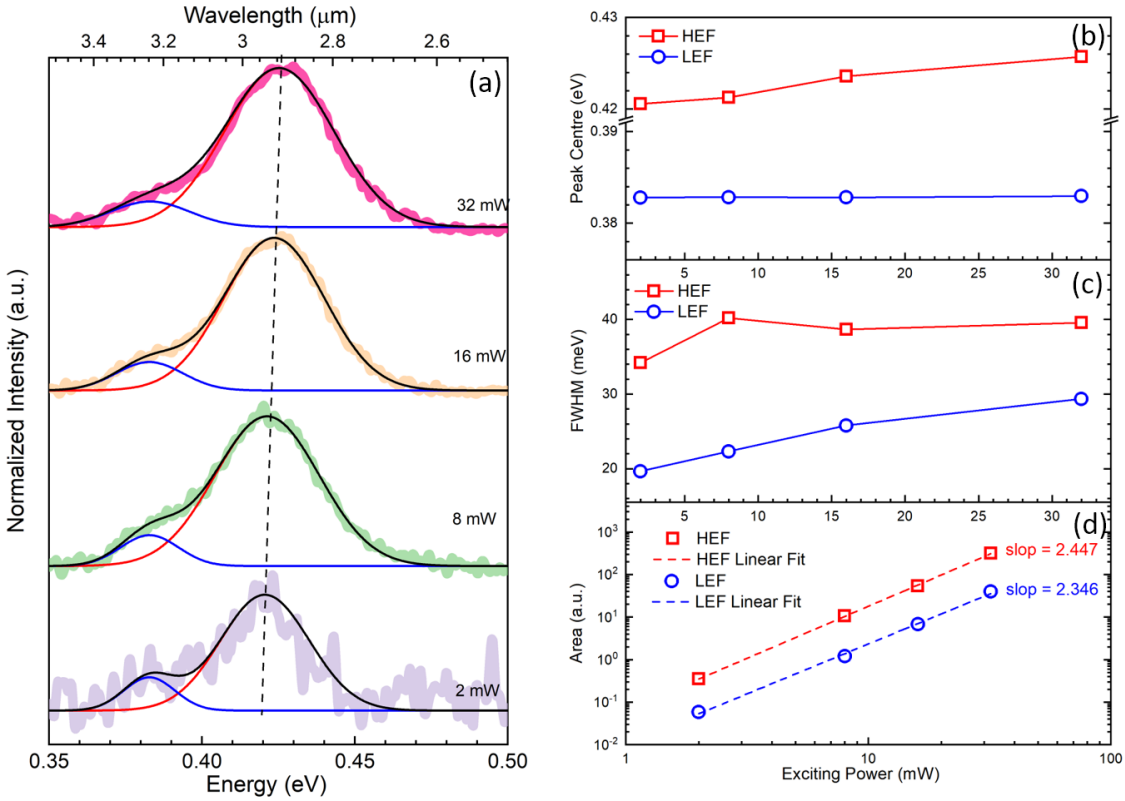

Figure 4.41: Photoluminescence spectra of InAs-InGaAs core-shell NWs under different excition power.

The integral intensities are depicted in Fig. 4.40 (d) against excitation power, and the relationship can be approximated by

$$I \propto P^{\alpha} \tag{4.15}$$

where I and P are the integral intensity and excitation power. α depends on the recombination of photo-induced carriers. It is clear that Eq. 4.15 describes the experimental evolution very well for both HEF and LEF as shown in Fig. 4.41. The intensity of HEF is one order of magnitude higher than LEF with a larger value of α, which means HEF domains the peak and has higher efficiency of luminescence.

In this section, the InAs-InGaAs core-shell structure has been successfully prepared through a two-step growth method, although the morphology of the core-shell nanowires obtained under this growth condition is relatively variable. TEM intuitively confirms the existence of the core-shell structure and provided strain information of the element distribution information at the core-shell interface. Photoluminescence spectroscopy shows that this structure has a higher emission energy than pure InAs nanowires, mainly showing two emission peaks. Through peak splitting analysis, we found that the emission wavelength remains stable in both variable temperature and variable power measurements, and the high-energy main peak (HEF) has higher luminescence efficiency.

Chapter 5

GaAs nanowire based quantum hybrid structures

The morphology of the NWs gradually evolves from a radial heterostructure to an axial heterostructure with the incorporation of Sb and the help of appropriate growth temperature, as discussed in Sec. 4.5, and we believe that a pure axial heterostructure will be formed under suitable conditions. In the 1-D growth mode, GaAs follows the VLS mode, meaning that the GaAs crystal forms at the interface of GaAs/Ga, so that the top Ga droplets will play a role in regulating growth providing a means of regulation for the growth of axial heterojunctions. In this chapter, we will study Sb-containing heterojunctions based on GaAs NWs. First, GaSb disk was grown over the GaAs stem, and then GaAs NWs was grown to form a disk sandwiched in GaAs NW. Finally, multiple disk heterostructures embedded in GaAs NW was achieved.

5.1 Growth and basic characterization of GaAs NWs

GaAs NWs were successfully grown on <111>Si via VLS mode mentioned in Chapter 3 [75]. The GaAs NWs in Fig. 5.1 are longer than 8 µm, thus few of the NWs in the image are slightly tilted, and individual NWs sway under the impact of the electron beam during taking the image, forming a blurred image. As a result of VLS mode growth, a Ga

droplet remains on top of each NW.

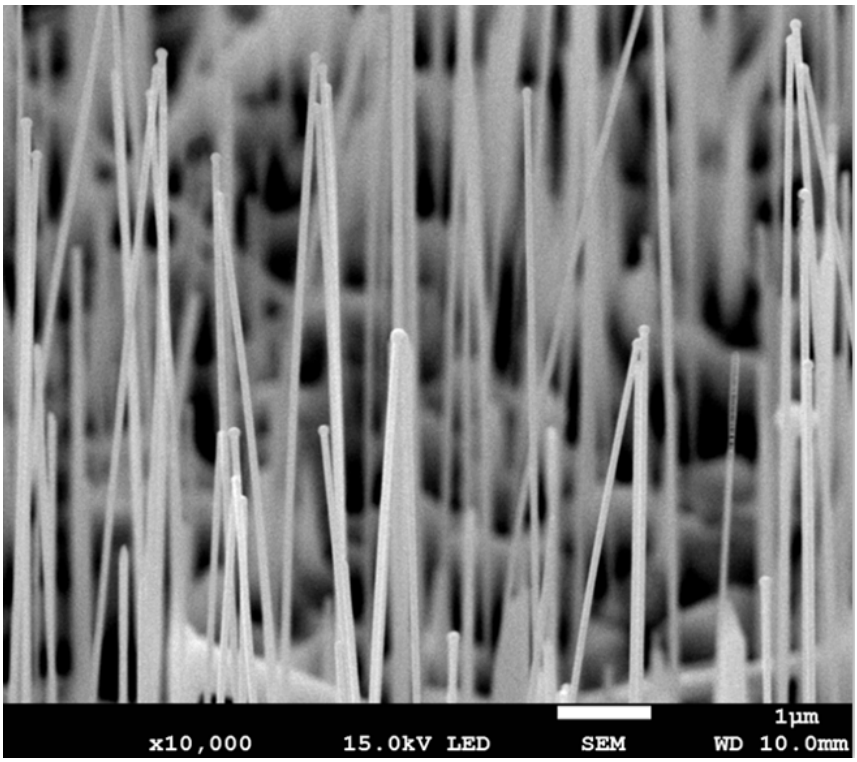

Figure 5.1: SEM image of long GaAs NWs grown in our lab.

Due to the surfactant effect, WZ and ZB phases often coexist during the growth of GaAs NWs, resulting type-II alignment between them. The energy for type-II at 4K is about 1.43 eV. Fig. 5.2 shows the power-dependent PL results of our GaAs NWs at 4.2 K. The spectrum under low excitation power exhibits a very tiny peak around 807 nm. Considering the bandgap (1.514 eV, 820 nm) of WZ GaAs at low temperature this small peak near 809 nm is from the transition of electrons in the WZ phases. As the excitation power increases, this peak vanishes, but a slightly lower energy peak gradually becomes apparent, centring near 821 nm, and there is no significant shift ovserved with the excitation power. According to the bandgap (1.514 eV, 820 nm) of the ZB phase bulk GaAs at low temperature, this small peak near 821 nm represents the transition of the electrons in the ZB phase. The peak of ZB GaAs NWs is about 21.5 meV lower than that of WZ GaAs NWs, which agrees with the result of previous report [76].

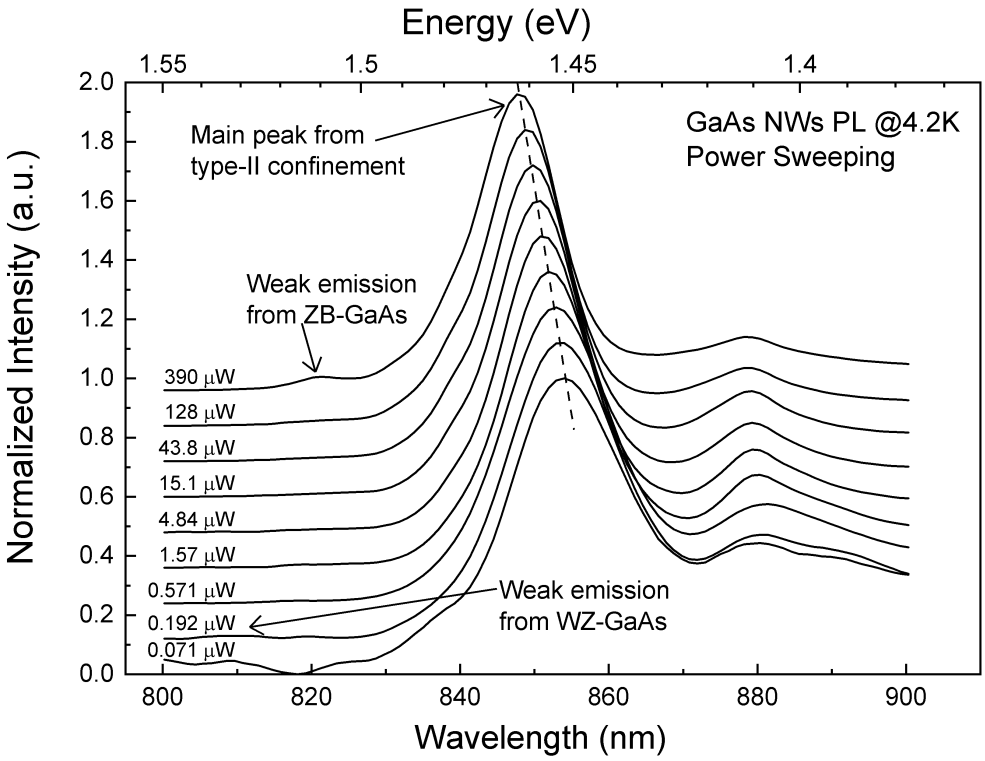

Figure 5.2: Power dependent PL spectra of GaAs NWs.

In the direction to lower energy than these two small peaks, a main peak exists, whose peak position shows a clear blue shift with the increase of the excitation power. The centre locates between $848-854$ nm (corresponding to $1.452-1.462$ eV), which is a very obvious characteristic of type-II QWs. It is worth noting that this result is 9 meV higher than the value of the bulk material type-II QWs, which is similar to the type-II case observed in InAs NWs and we believe this is a common phenomenon in the NWs grown in our system. Further more, our values are consistent with the reports of a few years ago [77]. The intensity of PL spectrum with the lowest excitation energy (0.07 μW) in Fig. 5.2 is much higher than the reported curve, thus we believe that PL line can still be collected though lower excitation power is used, and the corresponding peak energy may be further shifted toward 1.43 eV.

Fig. 5.3 confirms this inference. In Fig. 5.3, the peak position (both energy in triangle

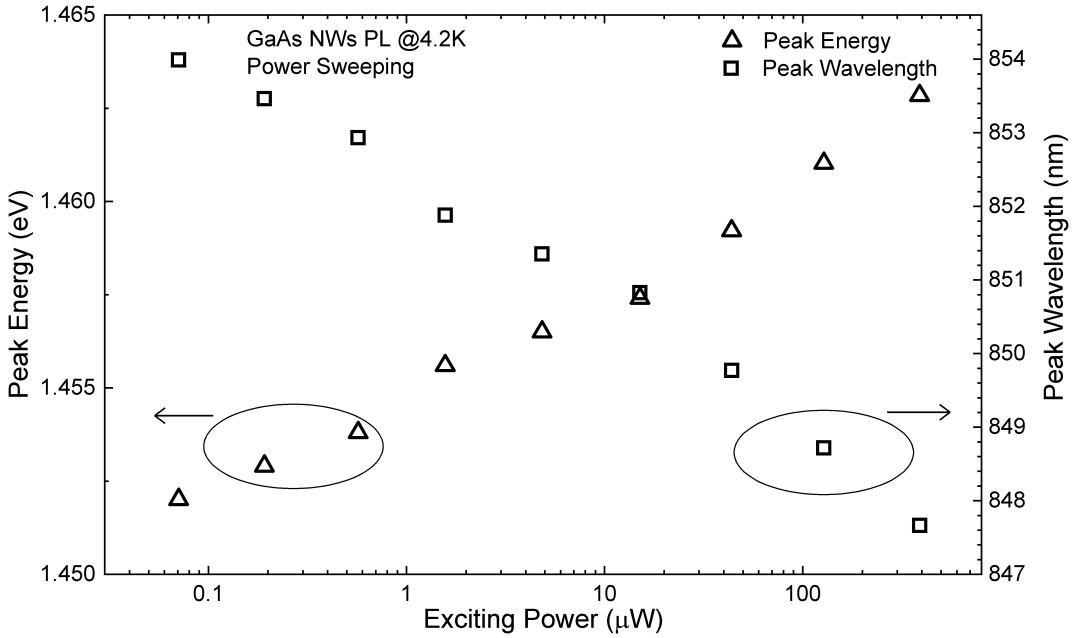

Figure 5.3: Peak position evolution as a function of exciting power.

and wavelength in square) is plotted as a function of exciting power. The peak position does not show any satuation in the range of $0.07 - 400$ μW, which covers near 4 orders of exciting power. We believe that the peak position will saturates around 1.43 eV under extreme low exciting power and saturates around 1.547 eV under extreme high exciting power in spite of band filling effect.

To further investigate and confirm the source of the PL data, the temperature-dependent PL was processed at an excitation power of 270 μW. Fig. 5.4 shows a typical temperature-changing PL feature. The PL spectrum shows one gradual peak in the range of $800 - 900$ nm. At low temperatures, the peak position appears near 1.51 eV. As the temperature increases, the peaks gradually red shift and widen, showing the characteristic of a typical BtB transition of ZB GaAs.

The peak position is summarized in Fig. 5.5. The triangle shows the peak energy points from the measured spectrum, and the thick black line represents the fitting plot using the function:

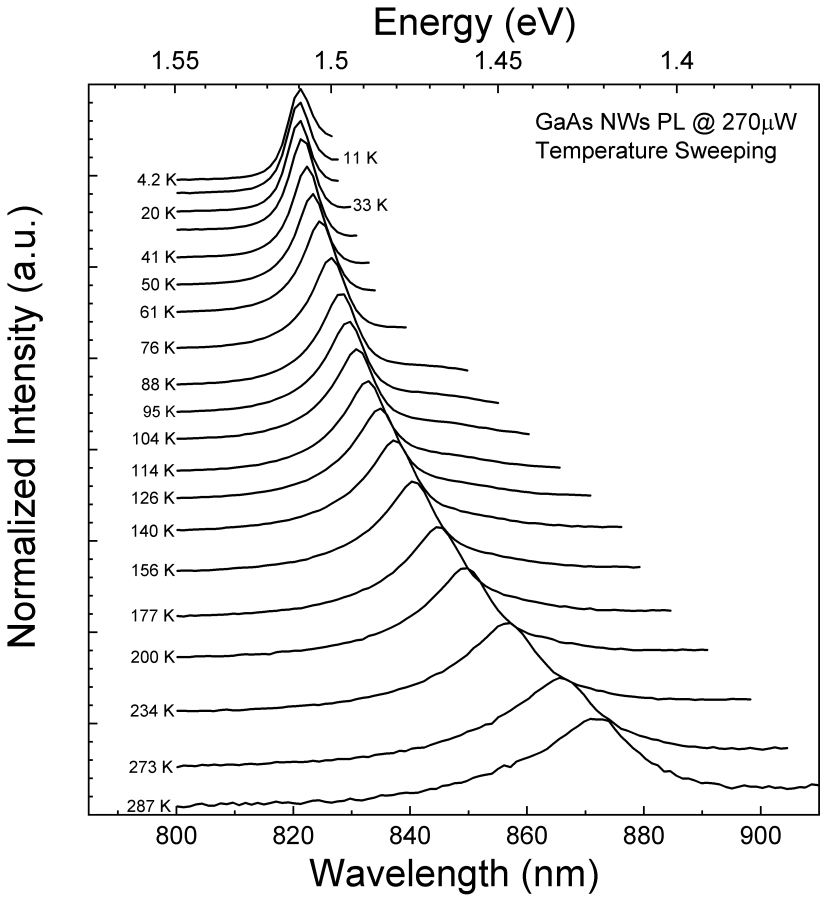

Figure 5.4: Temperature dependent PL spectra of GaAs NWs.

$$E_g(T) = E_g(0) - \frac{a\times10^{-4}T^2}{T+b} + c\times10^{-4}T \tag{5.1}$$

where $E_g(0)$ is the bandgap energy of GaAs NWs at 0 K, while a, b, c are constants with value of 5.36, 118.7 and 8.69, respectively. This function is a bit more complicated than Varshni's Eq. 1.18. In the equation, $E_g(0) = 1.519$, $a = 5.405$, $b = 204$, and $c = 0$. The item of $c\times10^{-4}T$ in our fitting prevents the energy fall too fast. The corresponding points of peak wavelength is also shown in Fig. 5.5 in square, the dash line represents its trends.

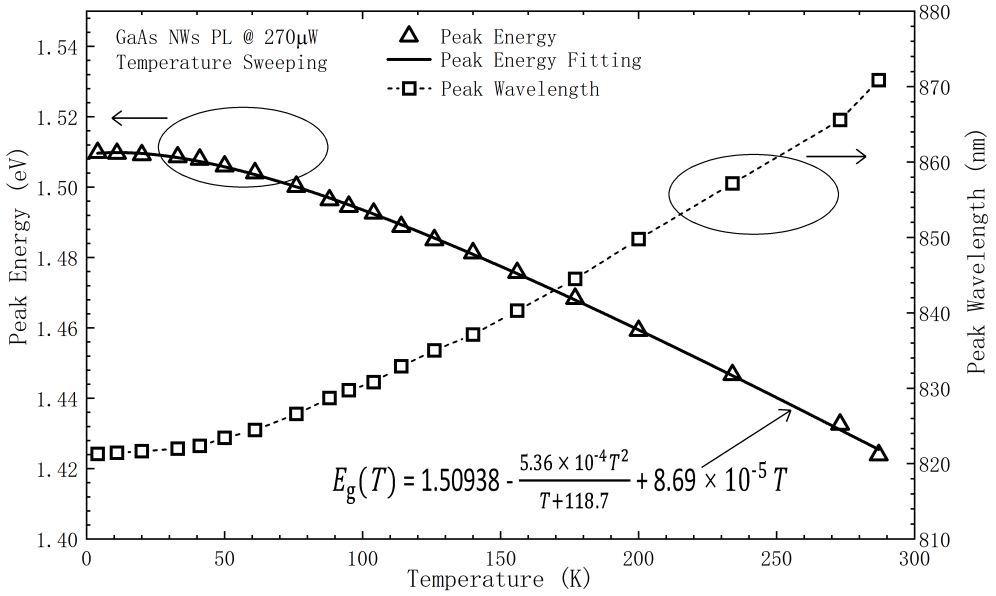

Figure 5.5: Peak position evolution as a function of temperature.

5.2 GaAs+GaSb axial nanowires

Thanks to the bandgap engineering, GaAsSb NWs have the ability to cover the telecom wavelength. But the growth of Sb-contained GaAs NWs still remain a challenge. The diameter of NWs usually increase significantly, and the droplets are much easier to fall down from the tip of NW, since the additional Sb would decrease the surface energy to the amplitude of one order, which means a much smaller contact angle for the droplets. So the growth parameter must be tuned deliberately for this series of materials.

Fig. 5.6 (a) shows the designed structure of sample A944 GaAs+GaSb axial heterostructure. After the growth of GaAs stem for 38 minutes, Ga As flux were set to zero immediately. Then the substrate temperature was reduced from 580 °C to 558 °C and the Ga & Sb shutters were kept opening to grow GaSb disks onto the top of GaAs stems for 1 hour. After the 1 hour's growth of GaSb stem, Ga Sb shutters were shut down and the temperature of substrate was reduced to terminate the growth. Fig. 5.6 (b) shows the SEM image of the as-grown GaAs+GaSb NWs. In this sample, most of the NWs are

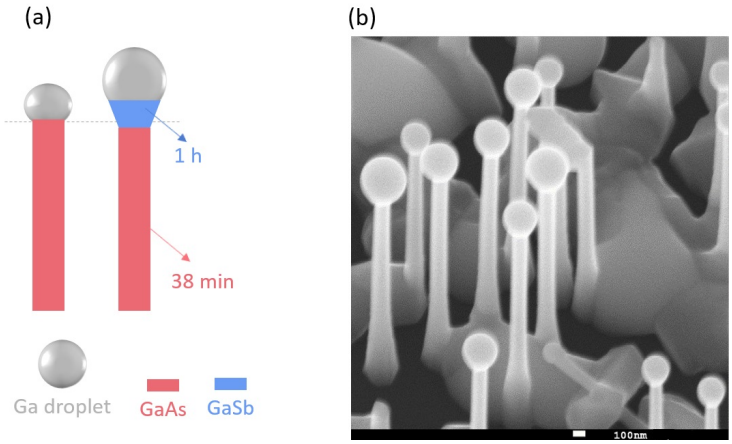

Figure 5.6: The sketched structure of sample A944 before and after the growth of GaSb disks on GaAs stem, and the SEM image of sample A944 GaAs+GaSb NWs.

vertically standing. The droplets on NWs grows much lager than the diameter of NWs.

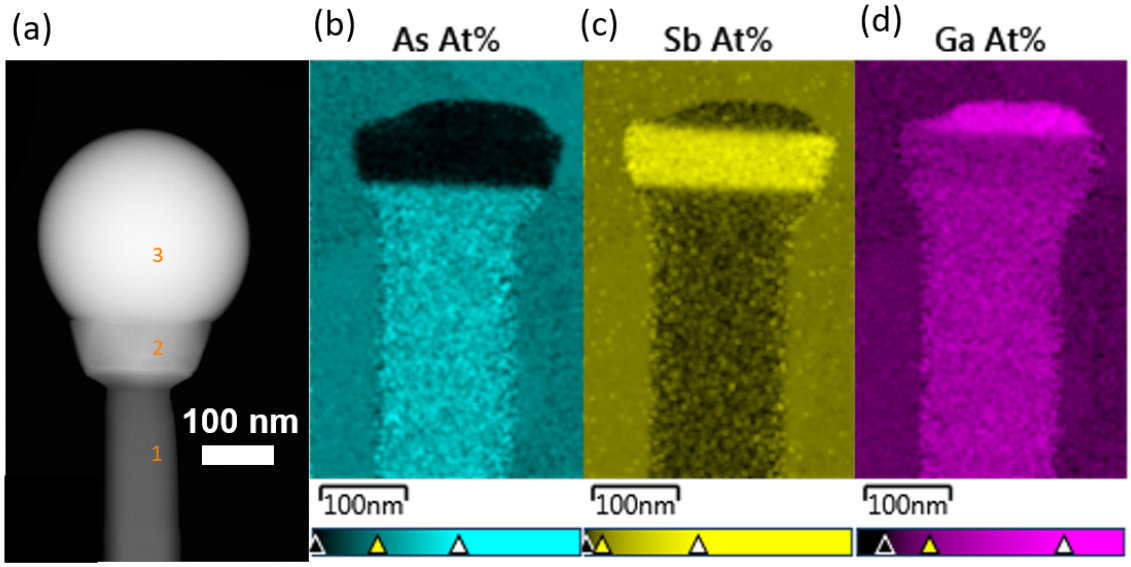

Figure 5.7: The TEM (a) and EDS (b)-(d) images of GaAs+GaSb axial NWs.

To investigate the strcture of the sample of GaAs+GaSb axial NWs, TEM was processed on individual NW. Fig. 5.7 (a) shows the TEM image of the top part of one individual axial NW. From this angle, the contrast clearly shows that the heterostructure has 3 parts: 1. the stem on the bottom, 2. a broad disk on the top of the stem, and 3. a big ball on the top of the entire structure. To identify the elements that each part contains,

EDS has been processed and the images are shown in Fig. 5.7 (b)-(d) for As, Sb and Ga, respectively. In Fig. 5.7 (b), As only exists in the GaAs stem, but the top region close to the GaSb disk has also became a bit broad. In Fig. 5.7 (c), Sb also only exists in one part: the GaSb disk. In Fig. 5.7 (d), Ga distributes along the entire NW. In the big ball (only shown part of it here) the magenta is brightest indicating the ball is nealy-pure Ga ball, but the magenta in the GaSb disks is weaker than that in the GaAs stem area due to the low sensitivity to Ga. It is a clear demonstration that this Ga-droplet-assisted VLS epitaxy is a possible route to a obtain axial heterostructures for Ga-based NWs. Since this method is able to assist the growth of both GaAs NWs and GaSb NWs at the same time, and the switching from GaAs to GaSb has been realized in this section, then we can try to switch the NW growth from GaSb to GaAs. Obviously, this may realize the sandwich structure of GaAs-GaSb-GaAs NWs which would be discussed in the next section.

5.3 Single GaAsSb disk embedded in GaAs NWs

In the previous section, we have successfully grown GaSb disks on the top of GaAs stem directly. The disadvantage is that the growth rate is very low as about 100 nm/h. To realize perfect embedded heterostructures, it is necessary to keep the diameter as same during the epitaxy of Sb-contained segments. In this section, we will try to grow GaAsSb disk instead of GaSb disk onto the top of GaAs stem, and then try to continue growing GaAs NWs. The growth conditions for GaAs stem is as the same as in Sec. 5.2. After the growth of GaAs stem, the Ga and As flux was stopped to pause the growth. Then the substrate temperature was rapidly reduced from 580 °C to 558 °C and the Ga & Sb shutters were opened to grow GaSb disks onto the top of GaAs stems. The flux of of Ga was kept as twice of Ga, and the norminal growth rate of Ga is 0.1 ML/s. After the growth of GaSb disks, additional GaAs parts were grown on the top of GaSb disks. Through the

above steps, a sandwich structure was formed.

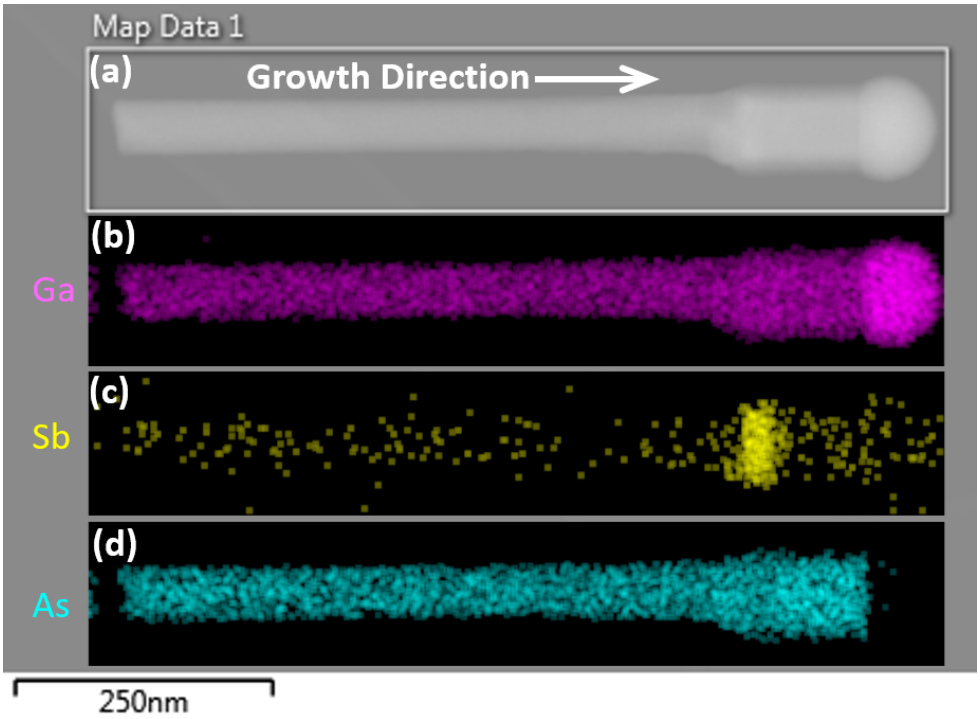

Figure 5.8: The TEM (a) and EDS mapping (b)-(d) images of sample of single GaAsSb disk embedded in GaAs NWs.

Fig. 5.8 (a) shows the TEM image of single GaAsSb disk embedded in GaAs NWs. The growth direction is from the GaAs stem to the Ga-droplet as the arrow shows. The sample can be simplly devided into 3 parts: 1. a thin GaAs stem, 2. a thick segment on the GaAs stem, and 3. the Ga droplets. The GaAs stem has quite uniform diameter of about 50 nm and length of about 580 nm. For part 2, the diameter is about 76 nm and the length is about 90 nm. The diameter of the droplet is about 96 nm and its hight along the growth direction is about 74 nm. In Fig. 5.8 (b) Ga distributes along the entire NW, and the droplet has brightest colour indicating it is a nearly-pure Ga droplets. In Fig. 5.8 (c), there is one region with bright yellow colour pointing the existence of Sb, whose thickness is about 32 nm. In Fig. 5.8 (d), As distributes all the area except for the droplet. It is worth noting that, in the area corresponding to the area with Sb, the brightness of As is a bit weak comparing to the upper area with thick and pure GaAs NW after the GaAsSb

disk, indicating that part of As just has been substituted by Sb. The brightness of the thicker GaAs part is higher than the first GaAs stem because the thicker material reflects more secondary electrons generated by GaAs.

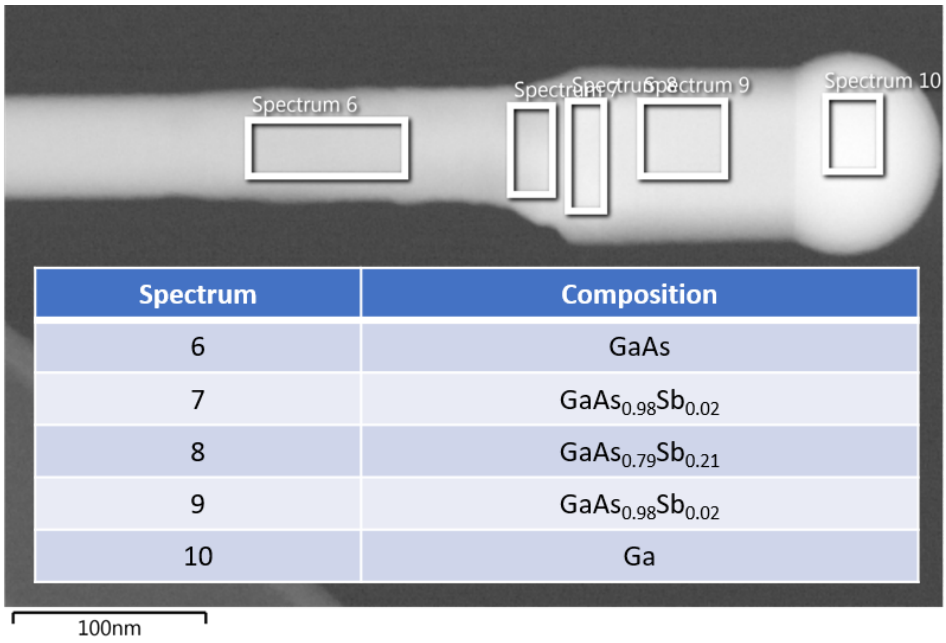

Spectrum	Composition
6	GaAs
7	$GaAs_{0.98}Sb_{0.02}$
8	$GaAs_{0.79}Sb_{0.21}$
9	$GaAs_{0.98}Sb_{0.02}$
10	Ga

Figure 5.9: EDS image of GaAs NW embedded with GaAsSb disk, with the insert table expressing the composition of each region.

Fig. 5.9 shows the EDS results in different areas of the axial NW. The quantitative results are listed in the insert table. For the GaAs stem, it is pure GaAs. For the disk it is ternary compound of GaAsSb rather than pure GaSb due to the residul As in the chamber and in the Ga-droplets. The Sb composition is larger than 20% based on Spectrum 8 in Fig. 5.9. Before the GaAsSb disk, the area with increasing diameter contains Sb composition of about 2%, indicating that the incorporation of Sb starts at this region accompanied with increase of diameter. After the GaAsSb disk, the area with large diameter has Sb composition of about 2%, indicating that it is not very easy to get pure GaAs segment after the growth of a thick GaAsSb disk. The droplets shows pure Ga as prediction.

5.4 Triple GaAsSb disks embedded in GaAs NWs

In the previous section, the sample of single GaAsSb disk embedded in GaAs NWs is realized by reducing the growth temperature and incorporating Sb into GaAs segment. To achieve multiple disks embedded in GaAs NWs, we repeat the growth steps of group "GaAs+GaAsSb" for 3 cycles with appropriate temperature as we used in the previous section.

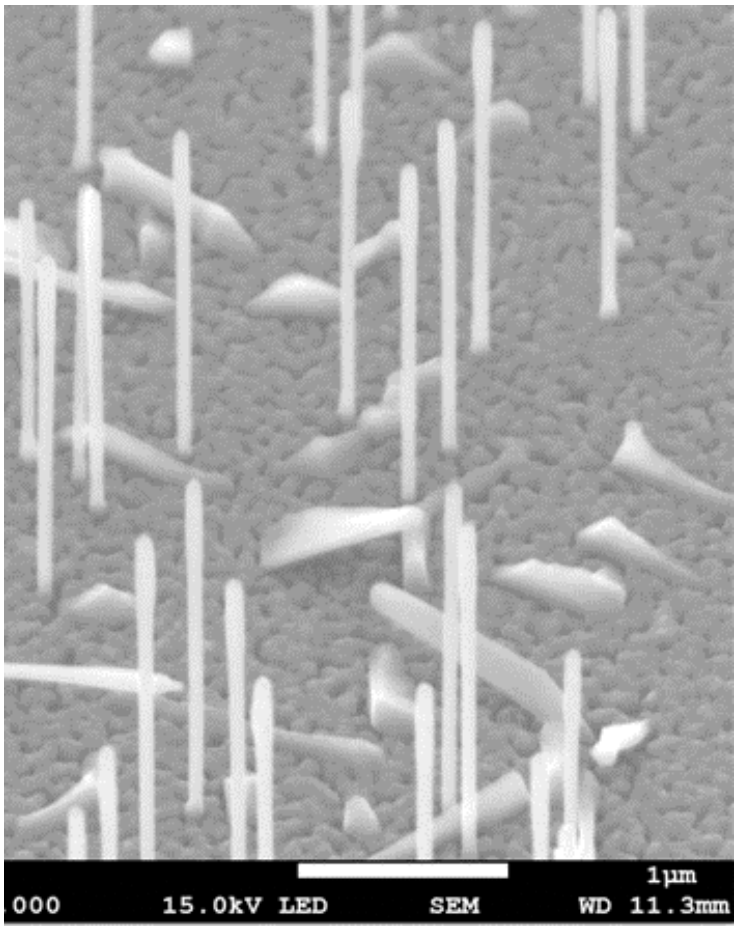

Figure 5.10: SEM image of GaAs NW embedded with trible GaAsSb disks.

The SEM image was taken to preliminary evaluate how successful the growth is. As shown in Fig. 5.10, the NWs of this sample are not as dense as other perfect samples, but all the NWs vertically stand on the surface of the Si substrate. Their length and diameter

are very uniform. It can be clearly seen that in the upper part of the NWs, their diameter slight increases, but not exaggerated. On the Si surface around the NWs, there are bumps spreading evenly. It is worth noting that there are many flaky products due to the change in surface energy caused by the incorporation of Sb, thereby inducing 1-D crystal growth to 2-D growth.

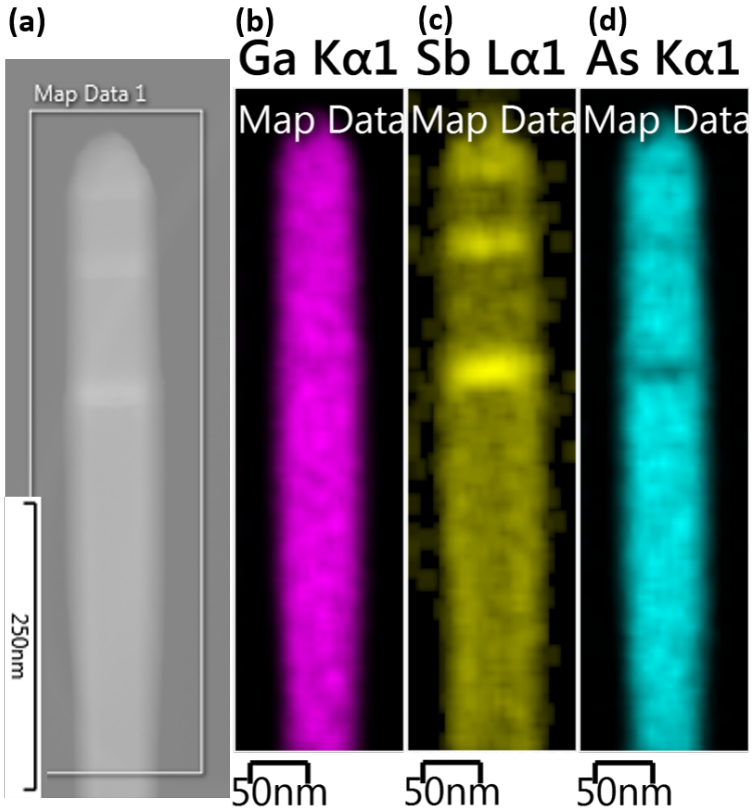

Figure 5.11: TEM (a) and EDS mapping (b)-(d) images of GaAs NW embedded with triple GaAsSb disks.

The TEM and EDS mapping images were taken to reveal the structure and didtribution of elements in the NWs. As the TEM image of the individual NW shown in Fig. 5.11 (a), there are 3 segments with bright colour in the upper part of the NW, indicating 3 heterostructures have been successfully embedded in the NW. The EDS mapping in Fig. 5.11 (b) & (d) shows the Ga & As distribute in the entire NW, but there are 3 dark lines in the position corresponding to the bright lines in Fig. 5.11 (a). In the corre-

sponding position of the 3 dark lines in Fig. 5.11 (d), there are also 3 bright yellow lines in Fig. 5.11 (c), demonstrating the Sb concentrates in the 3 disks. The yellow colour in GaAs region of Fig. 5.11 (c) is a bit bright than those in other EDS mapping images such as Fig. 5.7 (c) and Fig. 5.8 (c). We believe it is due to the 2-D growth co-exists during the growth of the GaAsSb disks similar to the situation of Sec. 4.5. So the linear EDS scan was processed along the growth direction of the NW.

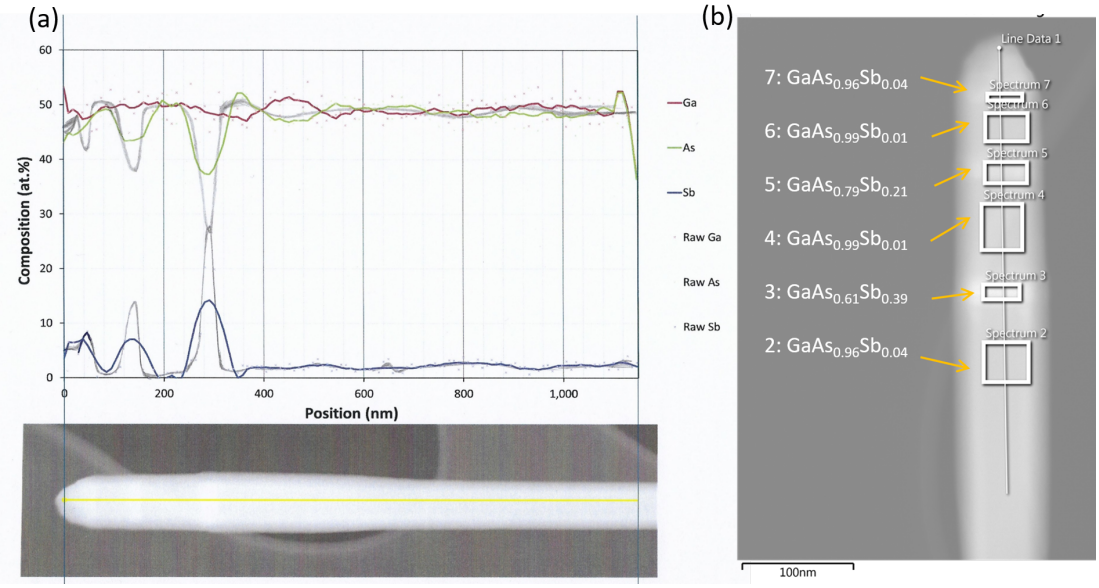

Figure 5.12: Linear mapping EDS image along the growth direction for GaAs NW embedded with triple GaAsSb disks (a) and quantitative areal EDS results for different regions in the NW.

Fig. 5.12 (a) shows the result of linear EDS scan. The red, green and blue lines represent elements of Ga, As and Sb, respectively. The distribution of Ga is very uniform along the entire NW, remain around 50%. In the region of $400 - 1200$ nm, As & Sb also remain uniform value of about 49% and 1%, which indicating the stem is GaAs. The little residual Sb is attributed to the error during the measurement and the slightly 2-D growth of Sb-contained layer around the sidewall of the NW. The Sb has 3 peaks in the position of 50 nm, 150 nm and 280 nm, while As has 3 valey in the same position, further confirming that the formation of GaAsSb disks. It is worth to note that, the green and blue lines were corrected into grey lines according to the measured data points plotted as green "Raw As"

points and blue "Raw Sb" points. In addition, the raw Sb composition at 280 nm is higher than 20%, which means $x > 0.4$ in that $InAs_{1-x}Sb_x$ disk. The areal EDS analysis is shown in Fig. 5.12 (b). The average Sb composition for each of the three GaAsSb disks is 39%, 21% and 4%, respectively as shown in region 3, 5 and 7. The value for region 7 is bit lower than our expection due to the technique issue during the measurement: the selected area is very thin and the position is a bit lower than the exact position where the GaAsSb disk locates. For region 2, 4 and 6, the average Sb composition is about 4%, 1% and 1%, respectively. We mainly ascribe the small amount of Sb to the slightly 2-D growth of Sb-contained layer around the sidewall of the NW. It is worthing to note that the the Sb composition of 4% in region 2 is bit higher than region 4 and 6, which implies that the 2-D growth of Sb-contained layer is more significant in this area than in other areas due to the longer 2-D growth time than region 4 and 6. The TEM image in Fig. 5.12 (a) shows that the diameter starts increasing in the region of $400 - 600$ nm before the growth of first GaAsSb disk, with the confirmation of position of the fist GaAsSb disk in the upper graph of Sb composition. This observation infers that high Sb composition is this area is not only due to the longer 2-D growth time, but also the assistant of Sb to the 2-D growth of Sb-contained layer.

To reveal the crystalline structure of the NW HRTEM images were taken for the entire NW. Fig. 5.13 (a) shows the nearly TEM image of the entire NW. In the bottom region grown in the initial time, there are a lot of defects. After this region, the main body of the GaAs stem is quasi-pure ZB as the zoomed-in HRTEM image shown in Fig. 5.13 (b). The zoomed-in HRTEM image of upper region containing GaAsSb disks are shown in Fig. 5.13 (c). The 3 GaAsSb disks are clearly shown embedded in the NW. The bottom interface is sharper than the upper interface of GaAsSb/GaAs for each disk. This is easy to be understood that the Sb started to crystallize quite quickly once the shutter of Sb opened, while onece the shutter of Sb closed the residual Sb in the co-melting droplets continue crystallizing for a period of time instead of stop crystallizing immediately, until

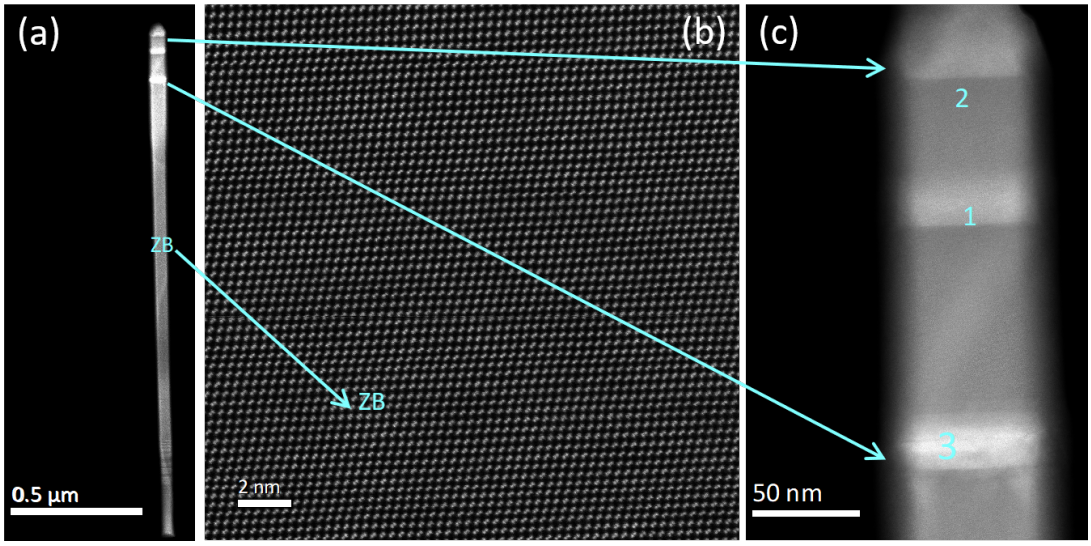

Figure 5.13: HRTEM images of GaAs NW embedded with triple GaAsSb disks.

the composition of Sb decrease below a specific level.

Two interfaces of the disks from Fig. 5.13 (c) are selected and their zoomed in HRTEM images are shown in Fig. 5.14. Fig. 5.14 (a) shows the area around GaAsSb/GaAs interface for the disk-3 in Fig. 5.13 (c). For the bottom region 3A, it is one part of the GaAs stem and exhibites ZB phase. When the growth is switched from GaAs to GaAsSb, Sb start incorporating into Ga droplets and tuning the crystallization. Similar to InAsSb growth in Sec. 4.3, with the Sb incorporation, the WZ phase percentage and the density of defects start increasing, resulting in the transition region 3B with mixed phases and defects. As the Sb incorporation increases more, the Sb starts crystallizing significantly, forming a pure ZB GaAsSb disk region 3C. For the interface area of disk-2 in Fig. 5.13 (c), the bottom region 2A is quasi-pure WZ phase due to the modification of small amount of residual Sb. With Sb incorporation, the density of defects increases forming the transition region 2B. As the Sb incorporation increases more, it results in pure ZB GaAsSb disk region 2C again just like 3C. The phenomenon of phase regulation in this GaAsSb/GaAs axial NWs sample is very similar to the regulation rule of InAsSb NWs exhibited in Fig. 4.20. There are a lot of similarities between the growth of InAs NWs and GaAs NWs.

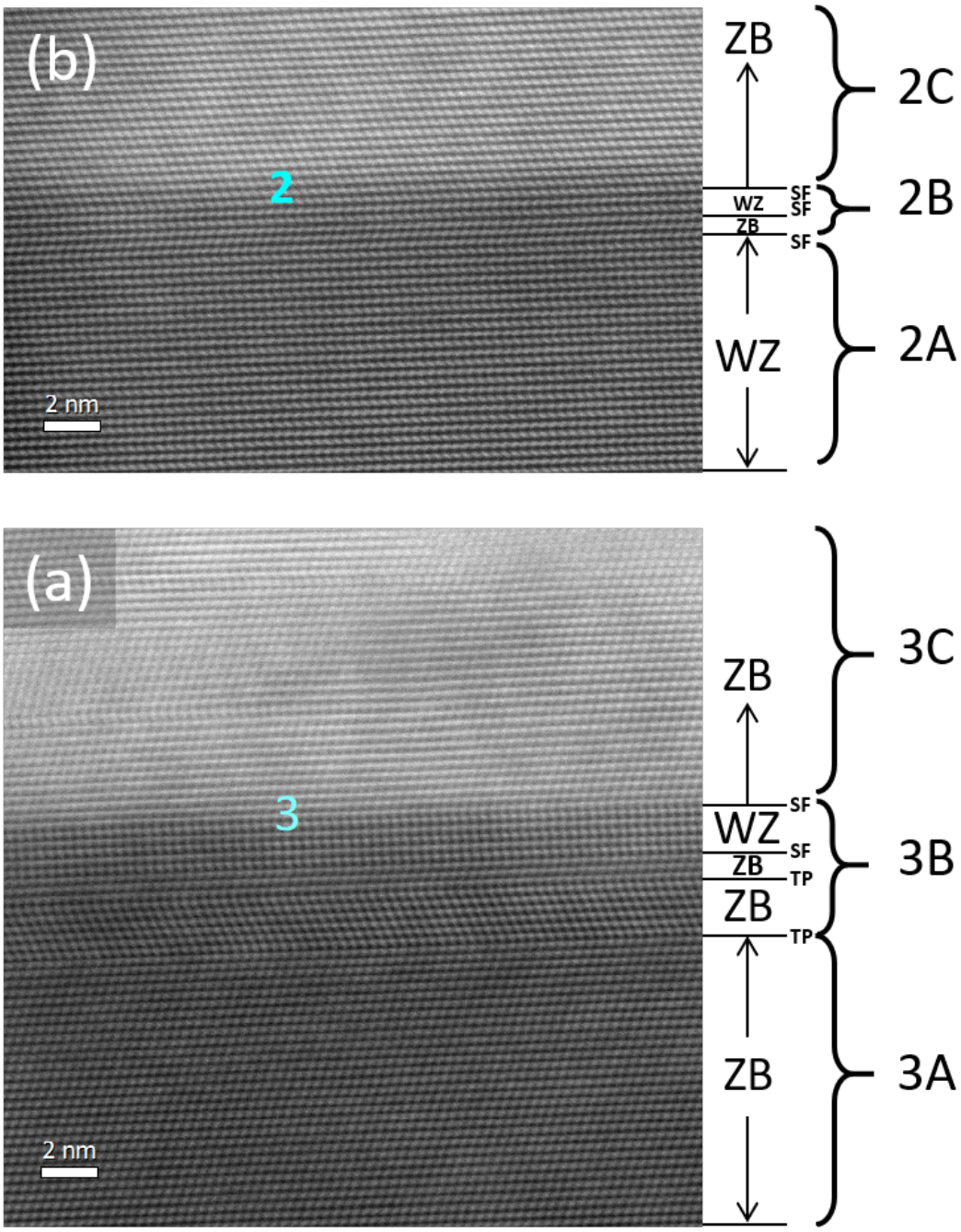

Figure 5.14: Zoomed in TEM images of GaAs NW embedded with triple GaAsSb disks focusing on the GaAs/GaAsSb interfaces.

To reveal the optical properties of this sample, power-dependent PL measurement has been processed at 20 K as shown in Fig. 5.15. In spite of the narrow peaks related to

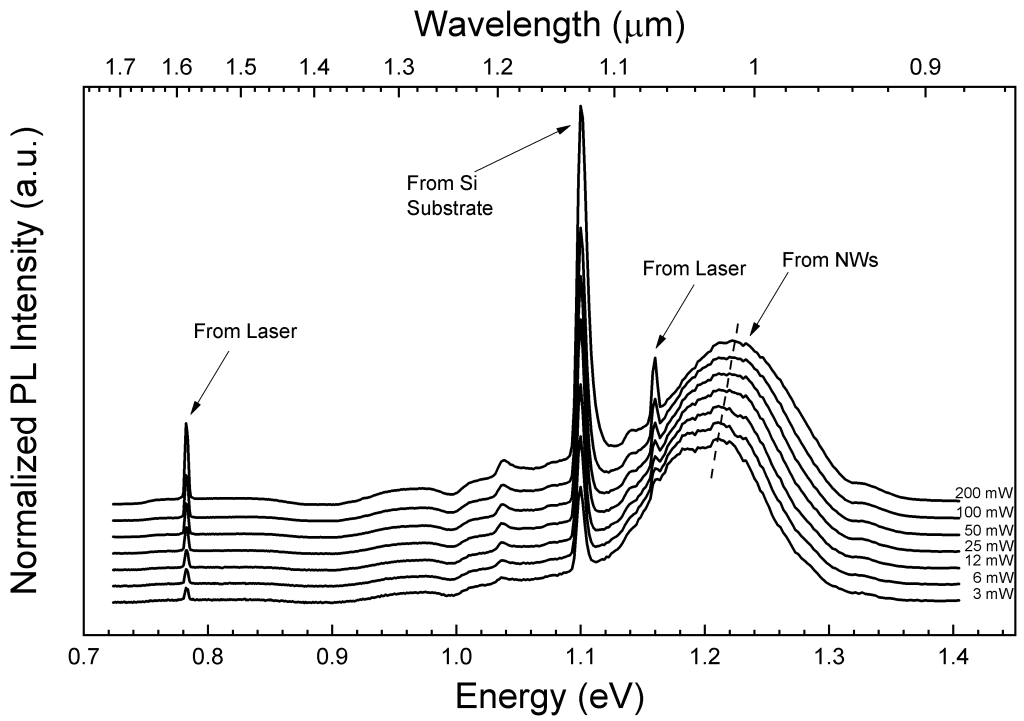

Figure 5.15: Power-dependent PL spectra of of GaAs NW embedded with triple GaAsSb disks measured at 20 K.

laser and from Si substrate, the main peak locates at about 1.2 eV. With the increasing evaluated power, the main peak blue-shifts. Each peak has been decomposed into 3 Gaussian peaks (in blue, red and green) as shown in Fig. 5.16. The grey spectral line represents the measured data points. The characteristic of the 3 fitted Gaussian peaks is very different from each other. For example, under the excitation with power of 3 mW, the peak in blue line is the main peak (LEF) with the highest energy among the 3 fitted peaks centring at above 1.2 eV, and its integrated intensity is very high as well. The secondary peak represented by red line (LEF) locates near 1.06 eV, of a relatively small centre energy and low integrated intensity. It is easy to identify the very narrow peak near 1.1 eV is from the Si substrate. As the excitation power increases, its peak position does not change but its intensity is greatly enhanced. For the main peak, as the excitation power increases, the peak position has a slight blue shift and the change of peak width can not be observed. The secondary peak has the largest changes among these three peaks. It

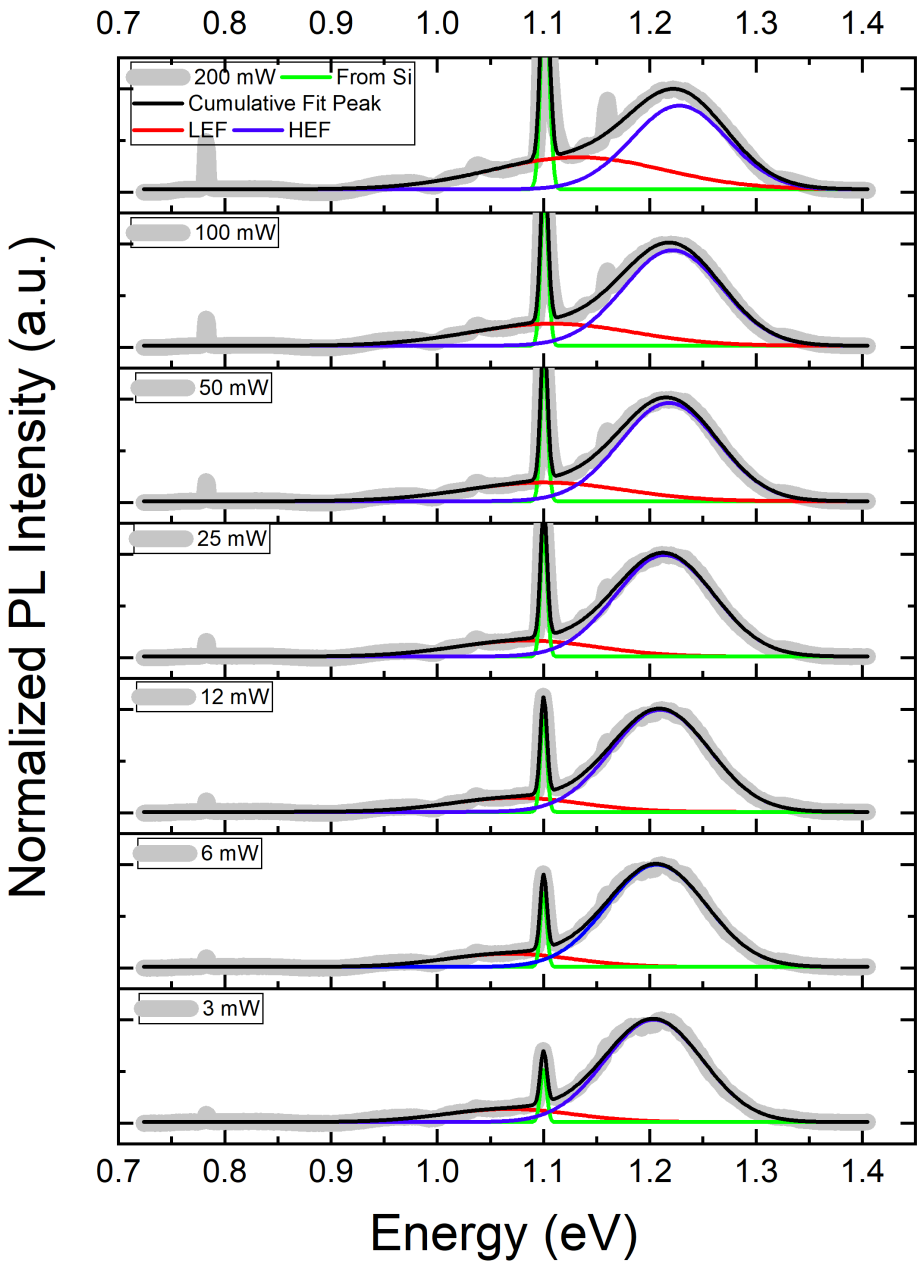

Figure 5.16: Power-dependent PL spectra of of GaAs NW embedded with triple GaAsSb disks measured at 20 K.

shifts from 1.06 eV to 1.13 eV, with increased intensity and width. The black line is the cumulative fit line. To quantitatively study the mechanism of the emission, the characters (Peak position, Integrated Intensity and FWHM) of LEFs and HEFs have been plotted

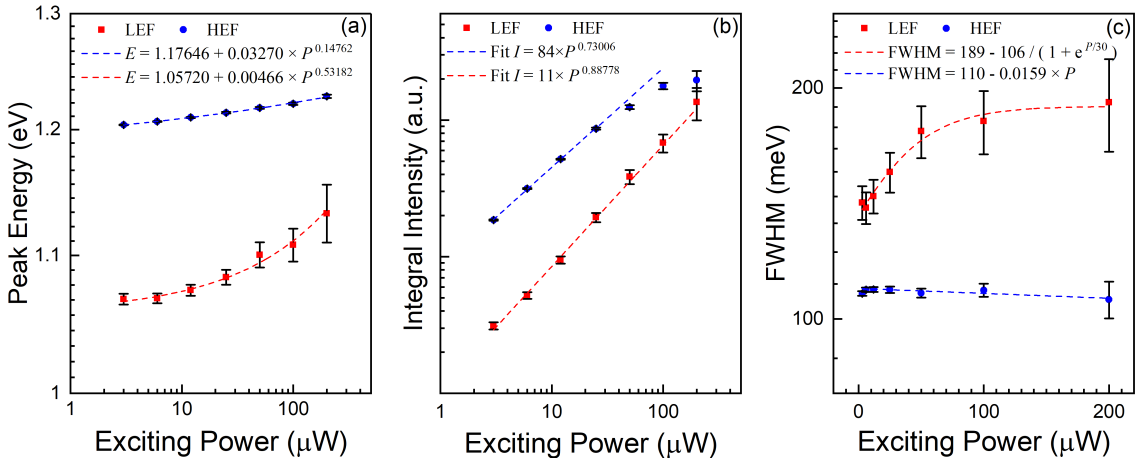

Figure 5.17: Power-dependent PL spectra of of GaAs NW embedded with triple GaAsSb disks measured at 20 K.

in Fig. 5.17. In Fig. 5.17 (a), the blue dots and red square represent the peak energy for HEF and LEF, respectively. Both of them have been fitted using equation:

$$E(P) = E_0 + CP^{\alpha} \tag{5.2}$$

which is derived from Eq. 4.4, where E_0 is the PL energy without band bending effect, P is the excitation power C is a coefficient, and α is the exponent. It is clear that Eq. 5.2 describes the experimental evolution very well in the measured range. Both the peak energy of HEF and LEF increase monotonically with the exciting power, and LEF rises more dramatically, which infers LEF is the emission from type-II QWs structure. The derived E_0 are 1.1765 eV and 1.057 eV for HEF and LEF, respectively, indicating their band energy without band bending effect. The integral intensities are depicted in Fig. 5.17 (b) against excitation power, and the dependence can be approximated by Eq. 4.15. The equation describes the experimental evolution quite well in a power range below 50 μW. α depends on the recombination of photo-induced carriers. $\alpha \approx 1$ hint defect/impurity-related process without free-exciton participation and/or radiative BtB transition. It is clear that under the exciting power over 50 μW the measured data points for HEF is

slightly lower than the predicted value, but the increase for LEF does not slow down. It is believed that, HEF is from radiative BtB transition while the LEF is from type-II QWs structure. In the high-exciting region, more photo-induced carriers are generated and then fall into GaAsSb/GaAs QWs. According to Equatinon 1.28, the carrier density is proportional to the exciting power, and the additional photo-induced carrier generated under high-exciting power prefer to fall into the QWs rather than paticipate the radiative BtB transition in GaAs, thus α for LEF is lager that of HEF, and the increase of integral intensity for HEF in high-exciting region slow down while LEF does not. Fig. 5.17 (c) illustrates the evolution of the FWHM of the PL features with excitation power for LEF and HEF. For the HEF, the FWHM does not have obvious change with exciting power. But in the opposite, the FWHM of LEF increase sharply in the low-exciting region but saturates in the high-exciting region. It is found that the equation

$$FWHM = W_0 + E_{\mathrm{QW}} \frac{\exp(P/P_0)}{1+\exp(P/P_0)} \tag{5.3}$$

can describe the FWHM well, where W_0 is the FWHM value at near-zero power, E_{QW} is the depth of the QWs forming at the interface of GaAsSb/GaAs, and P_0 is the activation power. Eq. 5.3 reflects the sharp increase in the low-exciting region and saturation in the high-exciting region. Data in Fig. 5.17 (c) were used for fitting to obtain the values of W_0 = 136 meV, E_{QW} = 53 meV and P_0 = 30 μW. It gives the predicted FWHM value of 136 meV at near-zero power and the depth of the QWs (53 meV) forming at the interface of GaAsSb/GaAs. Thus the formular in Fig. 5.17 (c) could also be written as: $FWHM = 189\ \mathrm{meV} + 53\ \mathrm{meV}\frac{\exp(P/30\ \mu\mathrm{W})}{1+\exp(P/30\ \mu\mathrm{W})}$. Thus a simple method to estimate the depth of QWs via power-sweeping PL measurement is proposed.

5.5 Triple thin GaAsSb disks embedded in GaAs NWs

In the last section, it can be seen in those TEM images such as Fig. 5.8 ∼ 5.13 that the incorporation of Sb, especially high-content and long-time period, incorporation, will significantly increase the diameter of the GaAsSb disk and the undesired 2-D growth on the side wall of NWs near the disk.

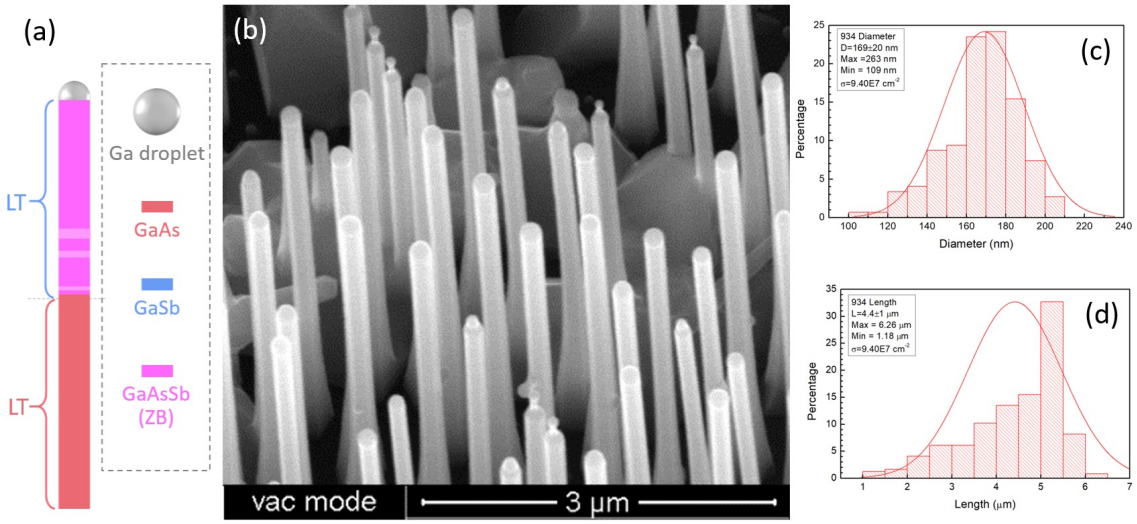

Figure 5.18: Morphology GaAs NWs embedded with trible thin GaAsSb disks. The sketched structure (a), the SEM image of as-grown sample (b), the statistics of diameter (c) and length (d) for the sample.

In order to overcome this under the premise of forming GaAsSb disks, we also significantly reduced the turn-on time of Sb flux, to minimize the effect of Sb incorporation on the disk diameter and 2-D growth.

Fig. 5.18 (a) shows the designed structure of the axial NW. Fig. 5.18 (b) is the SEM image of the as-grown sample. It shows that the diameter is relatively uniform and no significant increase in diameter is observed. The statistics of the morphology is shown in Fig. 5.18 (c) & (d). The average diameter is about 169 nm with a quite symmetrical distribution, while the length is mainly concentrated in 5 μm.

Fig. 5.19 shows the HRTEM images of the sample. The 3 bright lines in the mid-

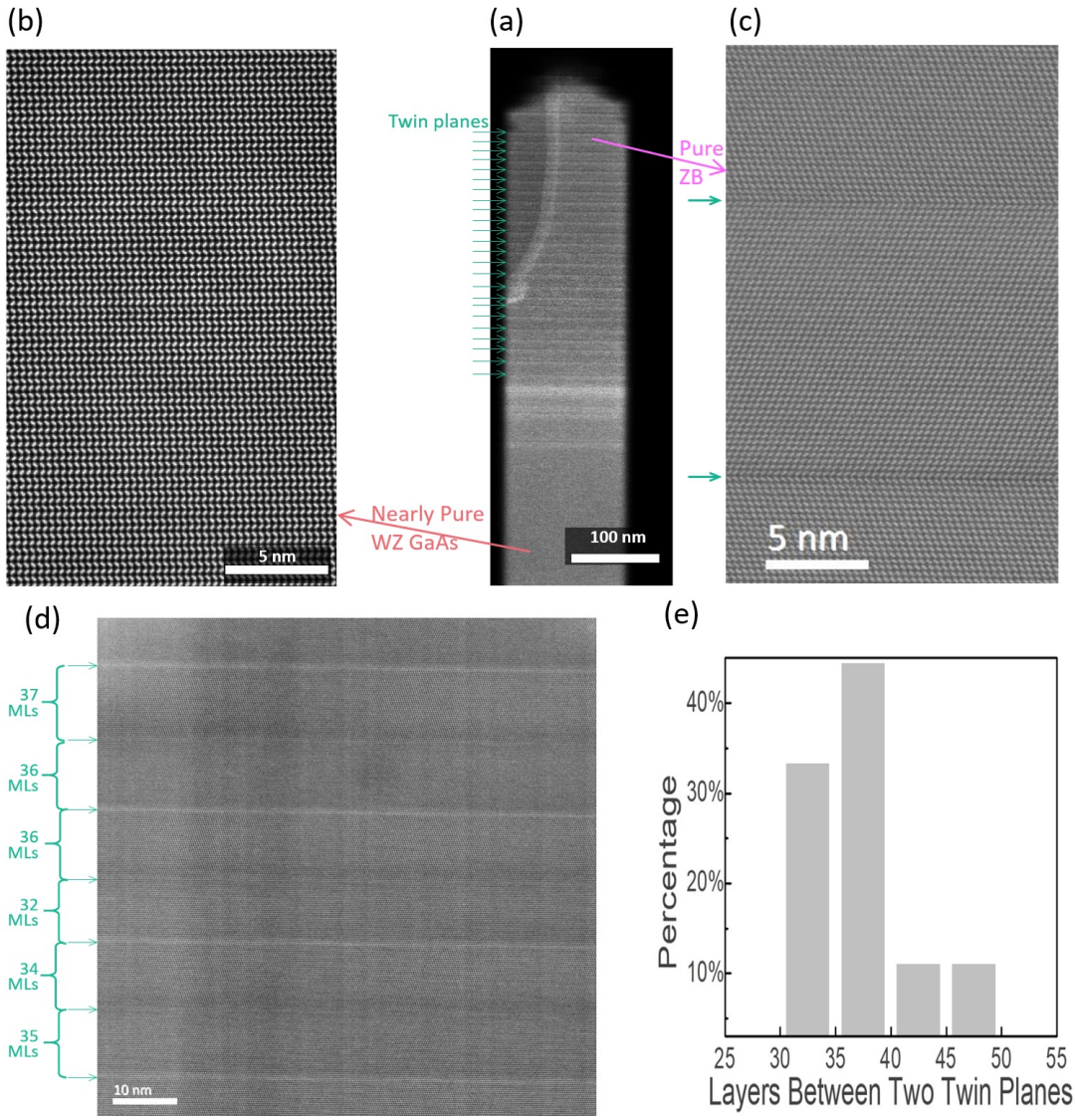

Figure 5.19: HRTEM images and phase statistics of the individual GaAs NW embedded with trible thin GaAsSb disks.

dle part of Fig. 5.19 (a) represents 3 GaAsSb disks crystallized under Ga/Sb flux and the residual As background in the chamber. The bottom part of the NW is pure WZ GaAs as shown in Fig. 5.19 (b), while the top part is pure ZB with TPs as shown in Fig. 5.19 (c). Interestingly, the TPs occur quite periodically here. We believe this is due to the modulation of small amount of Sb as well.

Fig. 5.19 (d) shows the quasi-periodic ZB segments, and the arrows point the position

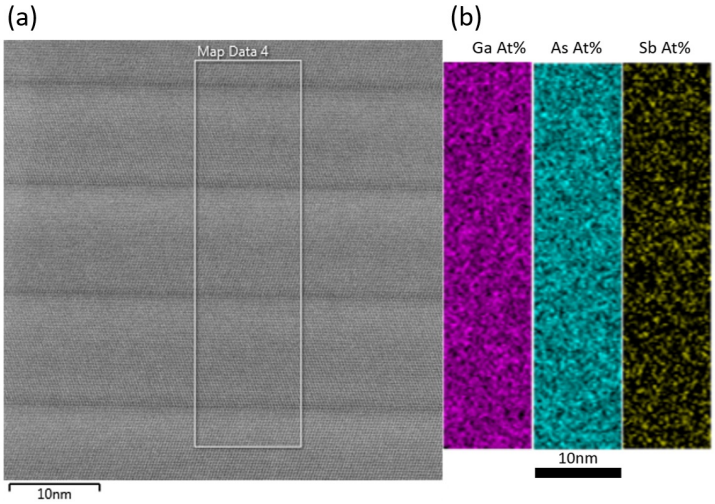

Figure 5.20: EDS analysis on the top part of the individual NW embedded with trible thin GaAsSb disks.

of TPs. To reveal the existence of TPs, the number of monolayers between two adjent TPs for many NWs and was plotted in Fig. 5.19 (e). It is very interesting that the number of monolayers between two adjent TPs is concentrated in the range of $30 - 50$, while the average value is about 37.

Area-selected mapping EDS focusing on the top region has been processed to investigate the distribution of each elements. In Fig. 5.20, both Ga & As distributes uniformly, and no fluctuation can be observed in the area. There is small amount of Sb co-existing.

To summary, GaAsSb/GaAs axial NWs has been successfully realized in this section by switching the As & Sb flux. The structure evolves from one GaSb segment on GaAs stem, to GaSb segment embedded in GaAs NWs, to triple GaSb disks embedded in GaAs NWs. The EDS images confirm the strcture. while the HRTEM images demonstrates clearly the phase modulation due to the Sb incorporation. With the Sb incorporation, the axial NWs embeded with 3 GaAsSb disks exhibts emission at about 1.18 eV and 1.06 eV from BtB transition and type-II transition, respectively. In the end, 3 ultra-thin GaAsSb disks have successfully embedded into the NW without any obvious change in NW diameter. The optical properties would be investigated in the future.

Chapter 6

Conclusion and outlook

6.1 Brief conclusion

This work concentrates on hybrid structures based on arsenic-containing nanowires, with a focus on material growth, structural regulation, and characterization of photoelectric performance, in order to obtain quantum heterostructures with excellent performance near the telecommunication characteristic wavelength. Specifically, it includes the following work:

We first study the growth of InAs NWs and GaAs NWs. Based on the full understanding of the selective area growth method, the importance of the appropriate oxide layer on the surface of the silicon wafer for nanowire growth is explained. The two-step growth method is demonstrated to realize the growth of GaAs NWs, and the droplet assisted growth method is also proposed to achieve the growth of InAs NWs.

For the InAs nanowires, after the growth, we characterized the morphology and found that the InAs NWs stood vertically on the surface of the silicon wafer with high density. For pure InAs NWs, the TEM shows that the microstructure is a mixed phase of WZ and ZB. The PL results show multimodal emissions, with the exception of the BtB transition, as well as typical type-II transitions.

A dominant PL feature is identified to be from the type-II optical transition across the interfaces between the ZB and the WZ phases, a lower-energy feature at low temperatures is ascribed to impurity-related transition, and a higher-energy feature at high temperatures

originates in the interband transition of the WZ InAs being activated by thermal-induced electron transfer. The optical properties of the ZB-on-WZ and WZ-on-ZB interfaces are asymmetric, and stronger non-radiative recombination and weaker carrier-phonon interaction show up in the NWs on p-type substrate, in which built-in electric field forms and leads to carrier assembling around the WZ-on-ZB interface. The results indicate that wide temperature-range infrared PL analysis can serve as efficient vehicle for clarifying optical properties and bandedge processes of the crystal-phase interfaces in vertically aligned InAs NWs.

By carefully tuning $FR_{\mathrm{V/III}}$ and F_{Sb}, InAsSb NWs with different Sb content have been obtained. The crystalline phases and luminescence properties are clearly revealed as a function of Sb incorporation via detailed measurements and analysis (including TEM, temperature-sweeping PL, power-sweeping PL) on a series of InAsSb samples. The crystalline phases and luminescence properties are mutually reinforcing and support each other. InAsSb NWs with Sb incorporation of up to 19% have been obtained by suppressing the Sb surfactant effect, and the emission wavelength is successfully extended to 5.1 µm covering the entire MWIR band. This study opens the way to fabricate next-generation devices using InAsSb NWs , such as highly sensitive silicon-based room-temperature infrared photodetectors operating in MWIR and LWIR, by combining the advantages of III-V semiconductors.

InAs/AlSb core-shell nanowire heterostructure is realized by molecular beam epitaxy and they also exhibit remarkable radiative emission efficiency, which is attributed to efficient surface passivation and quantum confinement induced by the shell. We artribute the remarkable radiative emission to the surface passivation, the oxide in the AlSb shell and the type-II bandgap alignment.

InAs/InGaAs core-shell NWs are also obtained by growing the shell layer after the InAs stem. Due to the introduction of Ga, nanowires exhibit a mixed growth path of core-shell and axial. The flux ratio for Ga to In is 2:1, while the EDS analysis shows

that the ratio of Ga to In in the shell is about 2.6:1, indicating that Ga exhibits stronger incorporation in the shell growth. The PL results show a bimodal emission with a main peak energy of approximately 0.425 eV, with a very stable temperature profile.

GaAs NWs were grown via VLS mode, and their optical properties were studied. The temperature and excitation scanning PL results show that the emission mainly comes from the transition of type-II alignment. The detector based on this shows high-speed photoresponse. The formation of the heterojunction after the introduction of Sb element was confirmed under the premise of maintaining the axial growth. The embedding of multiple GaAsSb nano disks is realized, with the emission wavelength increased to 1 µm, and the offset of conduction band of GaAs/GaAsSb is estimated to be about 53 meV. In addition, the embedding of ultra-thin GaAsSb nano disk is also successfully obtained.

6.2 Brief outlook

There are a few suggestions for the future work. Pure single crystal phase is very important for the performance of NW device. With the help of Sb, the phases of InAs NWs and GaAs NWs are well regulated, but the pure phase is still in demand for both InAs NWs and GaAs NWs. However, due to the limited understanding and regulation of the growth mechanism, the development of III-V nanowires for pure phase will remain a realistic issue for the foreseeable future, perhaps the most fundamental but the most difficult challenge in this field.

For InAs(Sb) NWs, this study opens the way to fabricate next-generation devices using InAsSb NWs , such as highly sensitive silicon-based room-temperature infrared photodetectors operating in MWIR and LWIR, by combining the advantages of III-V semiconductors. But the component regulation of ternary compounds is not always easy. The special growth mechanism of nanowires makes the precise regulation of components more complex. Moreover, the anisotropy of hexagonal nanowires tends to make the distribution

of elements non-uniform in the nanowires. In the shell growth process, this anisotropy becomes more pronounced, a bad effect is to destroy the uniformity of element distribution, and another good effect is that it is easy to induce the formation of novel quantum structures embedded in the nanowire, which is promissing for advanced photonic applications. It is worth mentioning that in our experiments, the light emission from InAs-InGaAs core-shell NWs is suspected to exhibit temperature stability characteristics. Due to the limitations of the conditions, the mechanism is not further confirmed and explained herein, but the revelation is that it is possible to prepare a device with relative temperature-stable performance.

For GaAs(Sb) axial NWs, axial heterostructures can be well implemented, and a steep interface is required to meet the requirements of advanced photonic devices. In our experimental results, the interface on one side of the heterojunction is very steep, but may be not on the other side. Fortunately, based on the results of the ultra-thin nano disk embedded in nanowire, we speculate that the ultra-thin nano disk helps to form a heterojunction with a sharp interface on both sides, which may help to greatly improve device performance. This structure of ultra-thin nano disk embedded in nanowire may also have great application prospects in single photon sources. Heterostructure and composition need to be adequately designed to cover the target wavelength.

Bibliography

[1] L.D. Rosenblum. *See what I'm Saying: The Extraordinary Powers of Our Five Senses*. W. W. Norton, 2010.

[2] P Schagen. Some recent developments in remote sensing. *Nature*, 266(5599):223, 1977.

[3] Jacob Fraden. *Light Detectors*, pages 461–501. Springer New York, New York, NY, 2010.

[4] Russell W Burns. *Communications: an international history of the formative years*, volume 32. IET, 2004.

[5] Stewart E Miller. Lightwaves and telecommunication: Pulses of light transmitted through glass fibers are lowering costs, increasing speed and capacity, and stimulating new uses of telecommunications systems. *American Scientist*, 72(1):66–71, 1984.

[6] FE Idachaba, Dike U Ike, and H Orovwode. Future trends in fiber optics communication. 2014.

[7] Abdul Al-Azzawi. *Light and optics: principles and practices*. CRC Press, 2018.

[8] Qi-Chao Sun, Ya-Li Mao, Si-Jing Chen, Wei Zhang, Yang-Fan Jiang, Yan-Bao Zhang, Wei-Jun Zhang, Shigehito Miki, Taro Yamashita, Hirotaka Terai, et al. Quantum teleportation with independent sources and prior entanglement distribution over a network. *Nature Photonics*, 10(10):671, 2016.

[9] Thaddeus D Ladd, Fedor Jelezko, Raymond Laflamme, Yasunobu Nakamura,

Christopher Monroe, and Jeremy Lloyd O' Brien. Quantum computers. *nature*, 464(7285):45, 2010.

[10] Steven Chu and Arun Majumdar. Opportunities and challenges for a sustainable energy future. *nature*, 488(7411):294, 2012.

[11] PM Pattison, JY Tsao, GC Brainard, and B Bugbee. Leds for photons, physiology and food. *Nature*, 563(7732):493, 2018.

[12] Philip Ronan. Em spectrum.svg - wikimedia commons, the free media repository. `https://upload.wikimedia.org/wikipedia/commons/f/f1/EM_spectrum.svg`, 2015. [Online; accessed 5-August-2019].

[13] Richard C Olsen and RC Olsen. *Remote sensing from air and space*, volume 1. SPIE Press Bellingham, 2007.

[14] Soumendu Datta, Tanusri Saha-Dasgupta, and DD Sarma. Wannier function study of the relative stability of zinc-blende and wurtzite structures in the cdx (x= s, se, te) series. *Journal of physics: condensed matter*, 20(44):445217, 2008.

[15] Helmut Föll and B Kolbesen. Agglomerate von zwischengitteratomen (swirl-defekte) in silizium-ihre bedeutung für grundlagenforschung und technologie. *Jahrbuch der Akademie der Wissenschaften in Göttingen, Vandenhoeck & Ruprecht*, 1976.

[16] Kimberly A Dick, Claes Thelander, Lars Samuelson, and Philippe Caroff. Crystal phase engineering in single inas nanowires. *Nano letters*, 10(9):3494–3499, 2010.

[17] David Ferry. *Semiconductor transport*. CRC Press, 2016.

[18] Svelto Orazio. Principles of lasers, 2010.

[19] Yariv Amnon and P Yeh. Optical electronics in modern communications. *New York*, 1997.

[20] Yoyo Hinuma, Andreas Grüneis, Georg Kresse, and Fumiyasu Oba. Band alignment of semiconductors from density-functional theory and many-body perturbation theory. *Physical Review B*, 90(15):155405, 2014.

[21] Milton Ohring. *Reliability and failure of electronic materials and devices*. Elsevier, 1998.

[22] Milton Ohring. *Materials science of thin films*. Elsevier, 2001.

[23] Anatoli Rogalski. Recent progress in infrared detector technologies. *Infrared Physics & Technology*, 54(3):136–154, 2011.

[24] A Rogalski and Z Orman. Band-to-band recombination in inas1- xsbx. *Infrared physics*, 25(3):551–560, 1985.

[25] P. Zory. *Quantum well lasers*. London: Academic Press, 1993.

[26] Paul Harrison and Alex Valavanis. *Quantum wells, wires and dots: theoretical and computational physics of semiconductor nanostructures*. John Wiley & Sons, 2016.

[27] Jun Shao, Rolf Winterhoff, Achim Dörnen, Enno Baars, and Junhao Chu. Ordering effects on optical transitions in gaxin1-xp/(al0.66ga0.34)yin1-yp quantum wells studied by photoluminescence and reflectivity spectroscopy. *Physical Review B*, 68(16):165327, 2003.

[28] Xiren Chen, Yuxin Song, Liang Zhu, SM Wang, Wei Lu, Shaoling Guo, and Jun Shao. Shallow-terrace-like interface in dilute-bismuth gasb/algasb single quantum wells evidenced by photoluminescence. *Journal of Applied Physics*, 113(15):153505, 2013.

[29] Jun Shao, Zhen Qi, H Zhao, Liang Zhu, Yuxin Song, Xiren Chen, F-X Zha, Shaoling Guo, and SM Wang. Photoluminescence probing of interface evolution with annealing

in inga (n) as/gaas single quantum wells. *Journal of Applied Physics*, 118(16):165305, 2015.

[30] Handong Li, Hayfaa Alradhi, Zhiming Jin, Ezekiel A Anyebe, Ana M Sanchez, Wojcioech M Linhart, Robert Kudrawiec, Hehai Fang, Zhiming Wang, Weida Hu, et al. Novel type-ii inas/alsb core–shell nanowires and their enhanced negative photocurrent for efficient photodetection. *Advanced Functional Materials*, 28(8):1705382, 2018.

[31] Linyou Cao, Justin S White, Joon-Shik Park, Jon A Schuller, Bruce M Clemens, and Mark L Brongersma. Engineering light absorption in semiconductor nanowire devices. *Nature materials*, 8(8):643, 2009.

[32] Baomin Wang and Paul W Leu. Tunable and selective resonant absorption in vertical nanowires. *Optics letters*, 37(18):3756–3758, 2012.

[33] Bahram Ganjipour, Sobhan Sepehri, Anil W Dey, Ofogh Tizno, B Mattias Borg, Kimberly A Dick, Lars Samuelson, Lars-Erik Wernersson, and Claes Thelander. Electrical properties of gasb/inassb core/shell nanowires. *Nanotechnology*, 25(42):425201, 2014.

[34] DA Young. Etching of radiation damage in lithium fluoride. *Nature*, 182(4632):375–377, 1958.

[35] Saeed A Durrani et al. *Radon measurements by etched track detectors: applications in radiation protection, earth sciences and the environment*. World Scientific, 1997.

[36] RS Wagner and WC Ellis. Vapor-liquid-solid mechanism of single crystal growth. *Applied physics letters*, 4(5):89–90, 1964.

[37] A.Y.Cho and J.R.Arthur. Molecular beam epitaxy. *Progress in Solid State Chemistry*, 10(157-191), 1975.

[38] Nikhil P. Concept drawing of a molecular beam epitaxy growth chamber — wikimedia commons, the free media repository,

https://upload.wikimedia.org/wikipedia/commons/e/e9/molecular_beam_epitaxy.png, 2016. [Online; uploaded on 27 December 2013].

[39] Gertjan Koster, Mark Huijben, and Guus Rijnders. *Epitaxial Growth of Complex Metal Oxides*. Elsevier, 2015.

[40] Lee A Walsh and Christopher L Hinkle. van der waals epitaxy: 2d materials and topological insulators. *Applied Materials Today*, 9:504–515, 2017.

[41] Cui-Zu Chang, Jinsong Zhang, Minhao Liu, Zuocheng Zhang, Xiao Feng, Kang Li, Li-Li Wang, Xi Chen, Xi Dai, Zhong Fang, et al. Thin films of magnetically doped topological insulator with carrier-independent long-range ferromagnetic order. *Advanced materials*, 25(7):1065–1070, 2013.

[42] RM Ireland, Liang Wu, M Salehi, Seongshik Oh, NP Armitage, and HE Katz. Non-volatile solid-state charged-polymer gating of topological insulators into the topological insulating regime. *Physical Review Applied*, 9(4):044003, 2018.

[43] Jinsong Zhang, Cui-Zu Chang, Zuocheng Zhang, Jing Wen, Xiao Feng, Kang Li, Minhao Liu, Ke He, Lili Wang, Xi Chen, et al. Band structure engineering in (bi1-xsbx)2te3 ternary topological insulators. *Nature communications*, 2:574, 2011.

[44] Yi Zhang, Ke He, Cui-Zu Chang, Can-Li Song, Li-Li Wang, Xi Chen, Jin-Feng Jia, Zhong Fang, Xi Dai, Wen-Yu Shan, et al. Crossover of the three-dimensional topological insulator bi2se3 to the two-dimensional limit. *Nature Physics*, 6(8):584, 2010.

[45] Woo Kyung Cho, Sung Min Kang, Dong Jin Kim, Sung Ho Yang, and Insung S Choi. Formation of superhydrophobic surfaces by biomimetic silicification and fluorination. *Langmuir*, 22(26):11208–11213, 2006.

[46] Tom Toyosaki. Typical configuration of afm — wikimedia commons, the free media repository, 2020. [Online; uploaded on 22 April 2015].

[47] Weilie Zhou and Zhong Lin Wang. *Scanning microscopy for nanotechnology: techniques and applications*. Springer science & business media, 2007.

[48] MyScope. A generalised cut-away diagram of the internal structure of a transmission electron microscope alongside an example of a modern instrument., 2020. https://myscope.training/legacy/tem/introduction/.

[49] Robert G Hunsperger. Losses in optical waveguides. In *Integrated Optics*, pages 107–128. Springer, 2009.

[50] C Van Opdorp, C Werkhoven, and AT Vink. A method to determine bulk lifetime and diffusion coefficient of minority carriers; application to n-type lpe gap. *Applied Physics Letters*, 30(1):40–42, 1977.

[51] Charles E Lyman, Dale E Newbury, Joseph Goldstein, David B Williams, Alton D Romig Jr, John Armstrong, Patrick Echlin, Charles Fiori, David C Joy, Eric Lifshin, et al. *Scanning electron microscopy, X-ray microanalysis, and analytical electron microscopy: a laboratory workbook*. Springer Science & Business Media, 2012.

[52] Muhammad Y Bashouti, Thomas Stelzner, Andreas Berger, Silke Christiansen, and Hossam Haick. Chemical passivation of silicon nanowires with c1- c6 alkyl chains through covalent si- c bonds. *The Journal of Physical Chemistry C*, 112(49):19168–19172, 2008.

[53] Mohammed Reda Ramdani, Jean Christophe Harmand, Frank Glas, Gilles Patriarche, and Laurent Travers. Arsenic pathways in self-catalyzed growth of gaas nanowires. *Crystal Growth & Design*, 13(1):91–96, 2012.

[54] Emmanouil Dimakis, Jonas Lähnemann, Uwe Jahn, Steffen Breuer, Maria Hilse, Lutz Geelhaar, and Henning Riechert. Self-assisted nucleation and vapor–solid growth of inas nanowires on bare si (111). *Crystal Growth & Design*, 11(9):4001–4008, 2011.

[55] G Koblmüller, K Vizbaras, S Hertenberger, S Bolte, D Rudolph, J Becker, M Döblinger, M-C Amann, JJ Finley, and G Abstreiter. Diameter dependent optical emission properties of inas nanowires grown on si. *Applied Physics Letters*, 101(5):053103, 2012.

[56] Jun Shao, Wei Lu, GKO Tsen, Shaoling Guo, and JM Dell. Mechanisms of infrared photoluminescence in hgte/hgcdte superlattice. *Journal of Applied Physics*, 112(6):063512, 2012.

[57] Kuniharu Takei, Hui Fang, Bala Kumar, Rehan Kapadia, Qun Gao, Morten Madsen, Ha Sul Kim, Chin-Hung Liu, Elena Plis, Sanjay Krishna, et al. Highly quantum-confined inas nanoscale membranes. *arXiv preprint arXiv:1109.2685*, 2011.

[58] Claes Thelander, Philippe Caroff, Sébastien Plissard, and Kimberly A Dick. Electrical properties of inas1- xsbx and insb nanowires grown by molecular beam epitaxy. *Applied Physics Letters*, 100(23):232105, 2012.

[59] M Kopytko, K Jóźwikowski, P Martyniuk, W Gawron, P Madejczyk, A Kowalewski, O Markowska, A Rogalski, and J Rutkowski. Status of hgcdte barrier infrared detectors grown by mocvd in military university of technology. *Journal of Electronic Materials*, 45(9):4563–4573, 2016.

[60] B Mattias Borg, Kimberly A Dick, Joël Eymery, and Lars-Erik Wernersson. Enhanced sb incorporation in inassb nanowires grown by metalorganic vapor phase epitaxy. *Applied Physics Letters*, 98(11):113104, 2011.

[61] S Plissard, KA Dick, X Wallart, and P Caroff. Gold-free gaas/gaassb heterostructure nanowires grown on silicon. *Applied Physics Letters*, 96(12):121901, 2010.

[62] G. E. Cirlin, V. G. Dubrovskii, Yu. B. Samsonenko, A. D. Bouravleuv, K. Durose, Y. Y. Proskuryakov, Budhikar Mendes, L. Bowen, M. A. Kaliteevski, R. A. Abram,

and Dagou Zeze. Self-catalyzed, pure zincblende gaas nanowires grown on si(111) by molecular beam epitaxy. *Phys. Rev. B*, 82:035302, Jul 2010.

[63] Philippe Caroff, Kimberly A Dick, Jonas Johansson, Maria E Messing, Knut Deppert, and Lars Samuelson. Controlled polytypic and twin-plane superlattices in iii–v nanowires. *Nature nanotechnology*, 4(1):50, 2009.

[64] Wei Wei, Xin-Yu Bao, Cesare Soci, Yong Ding, Zhong-Lin Wang, and Deli Wang. Direct heteroepitaxy of vertical inas nanowires on si substrates for broad band photovoltaics and photodetection. *Nano letters*, 9(8):2926–2934, 2009.

[65] Tao Xu, Kimberly A Dick, Sébastien Plissard, Thanh Hai Nguyen, Younes Makoudi, Maxime Berthe, Jean-Philippe Nys, Xavier Wallart, Bruno Grandidier, and Philippe Caroff. Faceting, composition and crystal phase evolution in iii–v antimonide nanowire heterostructures revealed by combining microscopy techniques. *Nanotechnology*, 23(9):095702, 2012.

[66] EA Anyebe, Mohana K Rajpalke, Tim D Veal, CJ Jin, ZM Wang, and QD Zhuang. Surfactant effect of antimony addition to the morphology of self-catalyzed inas 1- x sb x nanowires. *Nano Research*, 8(4):1309–1319, 2015.

[67] EA Anyebe, AM Sanchez, S Hindmarsh, X Chen, J Shao, Mohana K Rajpalke, Tim D Veal, BJ Robinson, Oleg Kolosov, Frazer Anderson, et al. Realization of vertically aligned, ultrahigh aspect ratio inassb nanowires on graphite. *Nano letters*, 15(7):4348–4355, 2015.

[68] Marion JL Sourribes, Ivan Isakov, Marina Panfilova, Huiyun Liu, and Paul A Warburton. Mobility enhancement by sb-mediated minimisation of stacking fault density in inas nanowires grown on silicon. *Nano letters*, 14(3):1643–1650, 2014.

[69] Jun Shao, Wei Lu, Xiang Lü, Fangyu Yue, Zhifeng Li, Shaoling Guo, and Junhao

Chu. Modulated photoluminescence spectroscopy with a step-scan fourier transform infrared spectrometer. *Review of scientific instruments*, 77(6):063104, 2006.

[70] Jun Shao, Lu Chen, Wei Lu, Xiang Lü, Liangqing Zhu, Shaoling Guo, Li He, and Junhao Chu. Backside-illuminated infrared photoluminescence and photoreflectance: Probe of vertical nonuniformity of hgcdte on gaas. *Applied Physics Letters*, 96(12):121915, 2010.

[71] MH Sun, ESP Leong, AH Chin, Cun-Zheng Ning, GE Cirlin, Yu B Samsonenko, VG Dubrovskii, L Chuang, and C Chang-Hasnain. Photoluminescence properties of inas nanowires grown on gaas and si substrates. *Nanotechnology*, 21(33):335705, 2010.

[72] Lijun Zhang, Jun-Wei Luo, Alex Zunger, Nika Akopian, Val Zwiller, and Jean-Christophe Harmand. Wide inp nanowires with wurtzite/zincblende superlattice segments are type-ii whereas narrower nanowires become type-i: an atomistic pseudopotential calculation. *Nano letters*, 10(10):4055–4060, 2010.

[73] M Möller, MM de Lima Jr, A Cantarero, T Chiaramonte, MA Cotta, and F Iikawa. Optical emission of inas nanowires. *Nanotechnology*, 23(37):375704, 2012.

[74] QD Zhuang, Ezekiel A Anyebe, R Chen, H Liu, Ana M Sanchez, Mohana K Rajpalke, Tim D Veal, ZM Wang, YZ Huang, and HD Sun. Sb-induced phase control of inassb nanowires grown by molecular beam epitaxy. *Nano letters*, 15(2):1109–1116, 2015.

[75] C. Colombo, D. Spirkoska, M. Frimmer, G. Abstreiter, and A. Fontcuberta i Morral. Ga-assisted catalyst-free growth mechanism of gaas nanowires by molecular beam epitaxy. *Phys. Rev. B*, 77:155326, Apr 2008.

[76] Lyubomir Ahtapodov, Jelena Todorovic, Phillip Olk, Terje Mjåland, Patrick Slåttnes, Dasa L Dheeraj, Antonius TJ van Helvoort, Bjørn-Ove Fimland, and Helge Weman.

A story told by a single nanowire: optical properties of wurtzite gaas. *Nano letters*, 12(12):6090–6095, 2012.

[77] Neimantas Vainorius, Daniel Jacobsson, Sebastian Lehmann, Anders Gustafsson, Kimberly A Dick, Lars Samuelson, and Mats-Erik Pistol. Observation of type-ii recombination in single wurtzite/zinc-blende gaas heterojunction nanowires. *Physical Review B*, 89(16):165423, 2014.

Acknowledgement

I would like to thank all the friends and orgnization who has made efforts and provided benefits for the completion of this thesis. Considering the large number of people, I will not list them here one by one, but my gratitude is sincere. Among them I just separately thank Dr. Qiandong Zhuang, my supervisor, who always has as much knowledge as Isaac Newton in my eyes.

During my research, they usually do their best to answer the questions I ask them, but from the beginning to the end there is one question I only ask myself, a question that Albert Einstein used to be asked by a little boy, "what is the most important question in scientific research?". I have realized not all the questions have clear answer at a particular time, and one of the values of "research" is the process of "re"-search, which means searching again and again to reveal the fact and truth behind the fog. Thus I also would thank the graceful versicles I read and get power from when I face difficulties during the research, written by famous persons from England and China:

反者道之动，弱者道之用。
天下万物生于有，有生于无。
by 老聃

The world is the totality of facts, not of things.
by Ludwig Wittgenstein

The truth, it is a beautiful and terrible thing,
and should therefore be treated with great caution.
by J.K. Rowling (Albus Dumbledore)

历史没有真相，只残存一个道理。
by 马未都

Calm fell. From Heaven distilled a clemency;
There was peace on earth, and silence in the sky;
Some could, some could not, shake off misery:
The Sinister Spirit sneered: “It had to be!”
And again the Spirit of Pity whispered, “Why?”
by Thomas Hardy

大胆假设，小心求证。
by 胡适

This page leaves blank.

This page leaves blank.

This page leaves blank.